

AD-A048 907

AIR FORCE INST OF TECH WRIGHT-PATTERSON AFB OHIO SCH--ETC F/G 11/4  
A NUMERICAL ANALYSIS OF FRACTURE IN A LAMINATED FIBROUS COMPOSI--ETC(U)  
DEC 77 W P WITT

UNCLASSIFIED

AFIT/GA/AA/77D-9

NL

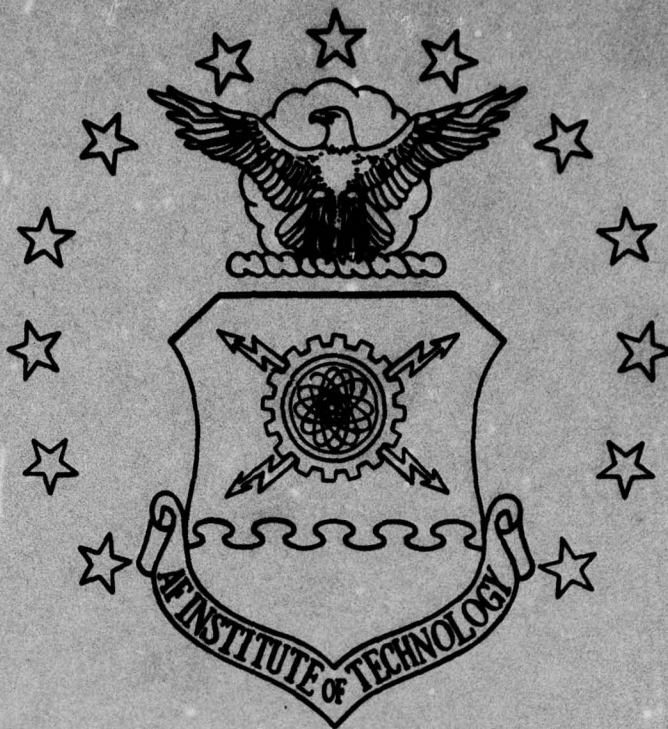
1 OF 2  
AD  
A048 907



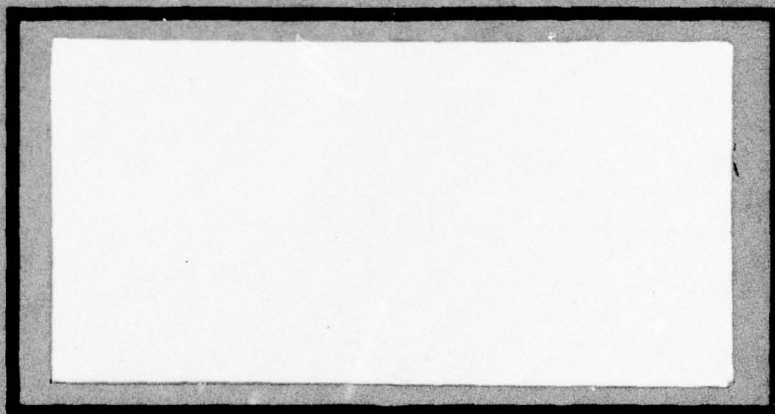
AD A 048907

AD No.

DDC FILE COPY



1



DDC  
JAN 23 1978  
F

UNITED STATES AIR FORCE  
AIR UNIVERSITY  
AIR FORCE INSTITUTE OF TECHNOLOGY  
Wright-Patterson Air Force Base, Ohio

**DISTRIBUTION STATEMENT A**

Approved for public release;  
Distribution Unlimited



①

DDC  
JAN 23 1978  
F

⑨ Master's Thesis,

②

A NUMERICAL ANALYSIS  
OF FRACTURE IN A LAMINATED  
FIBROUS COMPOSITE PLATE  
THESIS

⑭

AFIT/GA/AA/77D-9

⑩

William <sup>Porter</sup> Witt, III  
Captain USAF

⑪ Dec 77

⑫ 97p.

Approved for public release; distribution unlimited

Ø12225

✓B

**A NUMERICAL ANALYSIS  
OF FRACTURE IN A LAMINATED,  
FIBROUS COMPOSITE PLATE**

**THESIS**

**Presented to the Faculty of the School of Engineering  
of the Air Force Institute of Technology**

**Air University**

**in Partial Fulfillment of the  
Requirements for the Degree of  
Master of Science**

**by**

**William P. Witt, III, B.S.  
Captain USAF  
Graduate Astronautical Engineering  
December 1977**

**Approved for public release, distribution unlimited**

ACCESSION for	
NTIS	Write Section <input checked="" type="checkbox"/>
DDC	Buff Section <input type="checkbox"/>
UNANNOUNCED	<input type="checkbox"/>
S I I C A T I O N	
DISTRIBUTION/AVAILABILITY CODES	
SPECIAL	
<b>PA</b>	



## Preface

In this thesis, I have analyzed a notch in a laminated composite plate by numerically modelling the growth of the crack tip damage zone. The pseudo-crack represented by the damage growth is correlated with the actual lamina sub-crack growth which is shown in photographs. The growth of the damage zone is shown through a series of plots. Using three different methods, I was able to predict the fracture strength. It is hoped that the results presented will increase the understanding of fracture in laminated, composite structures.

As with any large project which is individually undertaken, my project involved the assistance of many other individuals, some of whom I must single out. I am indebted to Dr. T. Hahn of the Air Force Materials Laboratory for providing the experimental data and to Dr. V. Venkayya of the Air Force Flight Dynamics Laboratory who provided and explained the finite element program used for this thesis. I am especially indebted to Dr. Anthony Palazotto who was always available to provide valuable assistance and guidance throughout this long endeavor. My most special thanks must go to my wife, Pamela, who not only did an excellent job typing this thesis, but also endured me during this project.

William P. Witt, III



<u>Contents</u>	<u>Page</u>
Preface . . . . .	ii
List of Figures . . . . .	iv
List of Tables . . . . .	vii
List of Symbols . . . . .	viii
Abstract . . . . .	x
I. Introduction . . . . .	1
II. Theory . . . . .	8
Implications of Two Dimensional Analysis	8
Strength Determination . . . . .	10
Application of Numerical Analysis Results	16
III. Numerical Analysis Description . . . . .	29
Finite Element Model . . . . .	29
Bounding the Damage Zone . . . . .	39
General Procedure . . . . .	39
IV. Results . . . . .	41
General Results . . . . .	41
Correlation of Subcrack Length . . . . .	67
Failure Prediction . . . . .	74
V. Conclusions . . . . .	78
Bibliography . . . . .	80
Vita . . . . .	83

# List of Figures

Figure		Page
1	Modes of Crack Extension . . . . .	3
2	Specimen Geometry . . . . .	6
3	Loading Curve Showing Difference Between Discounting Methods. . . . .	15
4	Enhanced Radiographic Image of Ply Subcracks at 50% of the Experimental Fracture Load, Approxi- mately Five Times Actual Size. . . . .	18
5	Enhanced Radiographic Image of Ply Subcracks at 60% of the Experimental Fracture Load, Approxi- mately Five Times Actual Size. . . . .	18
6	Enhanced Radiographic Image of Ply Subcracks at 70% of the Experimental Fracture Load, Approxi- mately Five Times Actual Size. . . . .	19
7	Enhanced Radiographic Image of Ply Subcracks at 80% of the Experimental Fracture Load, Approxi- mately Five Times Actual Size. . . . .	19
8	Enhanced Radiographic Image of Ply Subcracks at 90% of the Experimental Fracture Load, Approxi- mately Five Times Actual Size. . . . .	20
9	Enhanced Radiographic Image of Ply Subcracks at 95% of the Experimental Fracture Load, Approxi- mately Five Times Actual Size. . . . .	20
10	Load Displacement Diagram Used to Calculate $\mathcal{Z}$	22
11	Instability Load Displacement Diagram . . . . .	24
12	Applied Load Versus Load Bearing Area . . . . .	28
13	First Mesh 163 Nodes, 252 Elements . . . . .	31
14	Second Mesh 252 Nodes, 457 Elements . . . . .	32
15	Resultant Force, $N_x$ , Relative to Applied Load, $P$ , Versus $x$ Distance $x$ From Crack For Both Meshes to Show Convergence . . . . .	34
16	Resultant Force, $N_x$ , Relative to Applied Load, $P$ , Versus $x$ Distance $y$ From Crack For Second Mesh, to Show Values Used For Integration . . . . .	35



17	Resultant Force, $N_x$ , Relative to Applied Load, P, Versus y Distance $x$ From Centerline for 2nd Mesh, to Show Values Used for Integration . . . . .	36
18	Sample Load Displacement Curve . . . . .	38
19	Load Versus Displacement Curve for Elastic Model.	43
20	Load Versus Displacement Curve for Progressive Failure Model . . . . .	44
21	Damage Zone Prediction at 10% of Experimental Fracture Load, Using Elastic Model . . . . .	46
22	Damage Zone Prediction at 20% of Experimental Fracture Load, Using Elastic Model . . . . .	47
23	Damage Zone Prediction at 30% of Experimental Fracture Load, Using Elastic Model . . . . .	48
24	Damage Zone Prediction at 40% of Experimental Fracture Load, Using Elastic Model . . . . .	49
25	Damage Zone Prediction at 50% of Experimental Fracture Load, Using Elastic Model . . . . .	50
26	Damage Zone Prediction at 60% of Experimental Fracture Load, Using Elastic Model . . . . .	51
27	Damage Zone Prediction at 70% of Experimental Fracture Load, Using Elastic Model . . . . .	52
28	Damage Zone Prediction at 80% of Experimental Fracture Load, Using Elastic Model . . . . .	53
29	Damage Zone Prediction at 90% of Experimental Fracture Load, Using Elastic Model . . . . .	54
30	Damage Zone Prediction at 100% of Experimental Fracture Load, Using Elastic Model . . . . .	55
31	Damage Zone Prediction at 20% of Experimental Fracture Load, Using Progressive Failure Model. .	57
32	Damage Zone Prediction at 30% of Experimental Fracture Load, Using Progressive Failure Model. .	58
33	Damage Zone Prediction at 40% of Experimental Fracture Load, Using Progressive Failure Model. .	59
34	Damage Zone Prediction at 50% of Experimental Fracture Load, Using Progressive Failure Model. .	60



35	Damage Zone Prediction at 60% of Experimental Fracture Load, Using Progressive Failure Model. .	61
36	Damage Zone Prediction at 70% of Experimental Fracture Load, Using Progressive Failure Model. .	62
37	Damage Zone Prediction at 80% of Experimental Fracture Load, Using Progressive Failure Model. .	63
38	Damage Zone Prediction at 85% of Experimental Fracture Load, Using Progressive Failure Model. .	64
39	Damage Zone Prediction at 87.5% of Experimental Fracture Load, Using Progressive Failure Model. .	65
40	Damage Zone Prediction at 88.75% of Experimental Fracture Load, Using Progressive Failure Model. .	66
41	$K_I^2$ Versus Subcrack Length for Elastic Model. . .	71
42	$K_I^2$ Versus Subcrack Length for Progressive Failure Model . . . . .	72
43	$\mathcal{D}$ Versus Subcrack Length for Progressive Failure Model . . . . .	73
44	Analytical Load Versus Load Bearing Area Diagram for This Specimen . . . . .	76

# List of Tables

Table		Page
I	Lamina Properties . . . . .	14
II	Loading Curve Data . . . . .	15
III	Load Displacement Curve Data . . . . .	42
IV	Subcrack Lengths . . . . .	68
V	$K_I$ Calculations (Elastic Model) . . . . .	69
VI	$K_I$ Calculations (Progressive Failure Model) . . . . .	69
VII	Strain Energy Release Rates . . . . .	70
VIII	Load and Load Bearing Area Data . . . . .	75



# List of Symbols

$A_E$	area of one element in a finite element mesh (in. <sup>2</sup> )
$A_{LB}$	remaining load bearing area after damage has occurred at the crack tip (in. <sup>2</sup> )
$a$	resultant crack half-length (in.)
$a_o$	initial crack half-length (in.)
$C$	dimension of damage zone measured colinear with existing crack or notch (in.)
$d_o$	critical distance over which stress is averaged to predict the occurrence of fracture (in.)
$E_{11}$	longitudinal elastic modulus ( $\frac{lb.}{in.^2}$ )
$E_{22}$	transverse elastic Modulus ( $\frac{lb.}{in.^2}$ )
$F, G, H, L, M, N$	failure strength parameters used in the Tsai-Hill failure criterion for anisotropic plates ( $\frac{in.^4}{lb.^2}$ )
$F_i, F_{ij}, F_{ijh}$	strength tensors used in the Tsai-Wu tensor failure criterion (various dimensions)
$J, J_c$	strain energy release rate ( $\frac{in.-lb.}{in.}$ )
$G_{12}$	shear modulus ( $\frac{lb.}{in.^2}$ )
$K$	stress intensity factor ( $\frac{lb.-in.^{\frac{1}{2}}}{in.^2}$ )
$K_I$	opening mode stress intensity factor ( $\frac{lb.-in.^{\frac{1}{2}}}{in.^2}$ )
$N_x$	resultant force in the global x-direction ( $\frac{lb.}{in.}$ )
$N_y$	resultant force in the global y-direction ( $\frac{lb.}{in.}$ )
$P, P_{ax}$	applied force (lb.)
$S$	ultimate in-place shear stress in anisotropic plates ( $\frac{lb.}{in.^2}$ )
$t$	plate thickness (in.)
$w$	plate width (in.)



X	ultimate longitudinal stress in anisotropic plates $\left(\frac{\text{lb.}}{\text{in.}^2}\right)$
Y	ultimate transverse stress in anisotropic plates $\left(\frac{\text{lb.}}{\text{in.}^2}\right)$
$\delta$	displacement of load application point (in.)
$\epsilon_x$	strain in global x-direction $\left(\frac{\text{in.}}{\text{in.}}\right)$
$\nu_{12}$	Poisson's ratio
$\sigma$	remotely applied stress $\left(\frac{\text{lb.}}{\text{in.}^2}\right)$
$\sigma_1, \sigma_2, \sigma_3$	normal stresses in the primary material directions for an anisotropic plate $\left(\frac{\text{lb.}}{\text{in.}^2}\right)$
$\sigma_a$	average stress $\left(\frac{\text{lb.}}{\text{in.}^2}\right)$
$\sigma_0$	ultimate unnotched tensile strength $\left(\frac{\text{lb.}}{\text{in.}^2}\right)$
$\sigma_i, \sigma_j, \sigma_k$	stress tensors $\left(\frac{\text{lb.}}{\text{in.}^2}\right)$
$\tau_{12}, \tau_{13}, \tau_{23}$	shear stresses for anisotropic plate $\left(\frac{\text{lb.}}{\text{in.}^2}\right)$

### Abstract

A crack in a laminated, composite plate was modelled using numerical methods. The experimental results used to validate this analysis were for a  $(0, \pm 45, 90)_s$  graphite/epoxy plate with a center notch oriented normal to the loading direction. Two, two-dimensional finite element models were used to determine the size of the crack tip damage zones. One involved a purely elastic analysis, and in the other, the element ply stiffness was completely discounted if the stresses exceeded the Tsai-Hill failure criterion. Damage zone diagrams showing the growth and shape of the ply damage zones at increasing load levels were developed for both models. The size of the sub-cracks in each ply were linearly related to the opening mode stress intensity factor,  $K_I$ , and to the strain energy release rate,  $G$ . A critical stress intensity factor approach, an instability approach, and a new fracture load prediction method based on load versus load bearing area diagrams were used to predict the fracture load. Since this new method provided close upper and lower bounds on the fracture load and is applicable to complicated structures, it was considered the best of the three methods.

A NUMERICAL ANALYSIS  
OF FRACTURE IN A LAMINATED,  
FIBROUS COMPOSITE PLATE

I. Introduction

This thesis is specifically concerned with the use of numerical methods to model a crack in a laminated composite plate. The crack is simulated by a through-the-thickness, finite width, center notch oriented normal to the loading axis. Conventional finite element analysis and classical laminated plate theory are used in the numerical model. These techniques are coupled with the use of composite strength theory and incremental loading to follow the growth and development of the damage zone at the crack tip. There are a variety of reasons why modelling should be addressed, but the primary motivating factors are money and safety.

Background

Recent fuel price increases have been the motivation for increased research into fuel-conservation technology. Significant fuel savings can be realized by lighter weight vehicles, and one of the most promising ways of reducing the structural weight of aerospace vehicles is to use high strength composites in primary structures [1]. As recognized by current Air Force



policy, fracture considerations are important in aircraft design and are especially important for the primary structures of aircraft [2]. Although current Air Force fracture design requirements only apply to metal aircraft structures, as composites become more widely applied, fracture mechanics considerations in the design of composite components will surely become mandatory in the interest of safety.

Linear elastic fracture mechanics (LEFM) theory has been developed for describing the behavior of brittle, homogeneous, isotropic materials. LEFM can be used to describe the three (3) basic modes of crack extension, shown in Figure 1 [3]. The crack follows three stages of growth. First a crack initiates from an existing flaw; it then propagates in a stable, usually slow manner, and last comes unstable extension and structural failure [4]. The crack will propagate in the direction along which the elastic energy release rate per unit crack extension will be maximum. In Mode I extension, this direction is perpendicular to the direction of greatest local tension [5].

In LEFM, crack propagation is explained by an energy balance at the crack tip between the strain energy release rate,  $\mathcal{G}_c$ , and the surface energy created by crack extension [6]. Another factor used in LEFM is the stress intensity factor,  $K$ , which is a measure of the stress intensity at the crack tip, where the crack tip stresses are inversely proportional to the square root of radial distance from the crack tip. The stress intensity factor depends on the magnitude of the applied forces, the geometry of the body containing the crack, the type of crack

extension, and the material in which the crack is propagating [5]. The basic theory assumes that the entire body containing the crack is elastic, when in actual materials the stress singularity at the crack tip produces plastic flow.

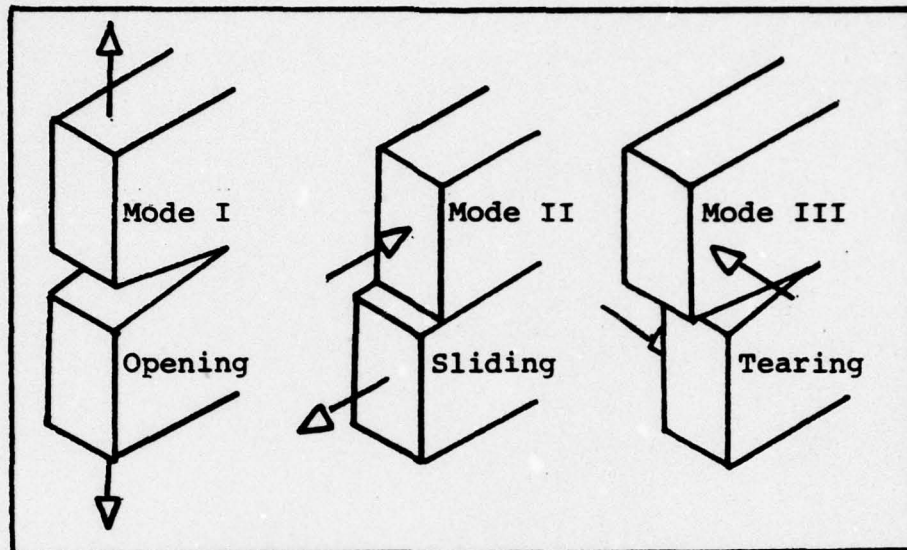


Figure 1. Modes of Crack Extension

LEFM can be modified to account for plasticity if the plastic region is small compared to the crack length [7]. The plastic deformation at the crack tip effectively blunts the tip and hence makes the material tougher [8]. Several models are available to account for the effect of plasticity, but the simplest method is to assume a plane stress solution and then modify the crack length by a parameter determined by the region where yielding has occurred [8].

If the small area at the crack tip in fibrous composites could be accurately modelled as homogeneous and anisotropic, many of the relations from LEFM could be directly applied since



none of the basic principles used in fracture mechanics would be violated [9]. But, it has been shown that fracture is very sensitive to the local properties at the crack tip [6]; therefore, the presence of two phases complicates the fracture process in composites. Insight into composite fracture can be gained by examining the observed phenomena of composite fracture.

Most of the composite fracture experiments have emphasized Mode I loading [10]. The cracks have either been parallel or perpendicular to fibers in unidirectional composites, or aligned with a material axis in composite laminates [6]. The observations made in these experiments can best be understood by relating them to the three stages of crack growth.

Microcracks initiate in the matrix almost from the onset of loading. The microcrack initiation sites are flaws which are introduced during the fabrication process [11] or are induced by stress concentration, battle damage, fatigue, or transient high loading conditions [12].

Due to the microscopic heterogeneity at the crack tip, cracks in composites do not propagate in the same manner as they do in isotropic materials [13]. After initiation, there is normally no visible self-similar crack growth [14]. Rather, the crack propagates by developing a network of microcracks [10]. Due to the difference in material properties between the fiber and the matrix, three types of crack propagation can occur when the microcracks reach the fiber matrix interface. The cracks can be reflected back into the matrix; they can

continue to travel directly through the fiber, or they may cause interfacial debonding [13]. Normally, subcracks are formed which extend parallel to the fibers. It has been observed that these subcracks continue to grow, either along the interface or in the matrix, and they are influenced by what occurs in the neighboring fibers [5].

In laminates, these subcracks extend in each ply along the fibers in a manner similar to the way the crack tip plastic zone grows in metals [4,13]. In fact, one group of experiments has shown that this damage zone can be treated like the plastic zone in metals to obtain fracture strength [13]. The damage zone seems to function like a plastic zone in that the "yielding" in the composite serves to blunt the crack tip and relax the stresses [4].

Subcracks and damage zone growth ultimately lead to failure of the structure. Ultimate failure may either be characterized by ply failure, where the fibers actually pull out from the matrix, or break, by delamination, or by a combination [15].

Thus at the present time, the direct applicability of LEFM to laminated composite fracture cannot be assumed [4, 6, 13]. The presence of notch sensitivity [4] and the fact that crack growth parallel to the fibers in unidirectional composites can be explained by a stress intensity factor [16, 17] indicate that some portions of presently developed isotropic fracture theory can be applied. The major divergences from isotropic fracture theory are the growth of a damage zone as opposed to crack opening from the crack tip and the dissimilar behavior of each ply



in a laminate to a given load.

The data which will be used to validate the analysis done in this thesis was generated by the Air Force Materials Laboratory [6, 10]. During the experiments, notched composite plates of Thornel 300 graphite fibers in Narmco 5208 epoxy were loaded to failure, Figure 2. The specimens shown in Fig. 2, contained either a 13mm or a 20mm notch in  $(0, \pm 45)_s$  and  $(0, \pm 45, 90)_s$  laminates. The results of these experiments were used to show that the notched fracture strength could be predicted using unnotched failure strength and the dimension of the damage zone.

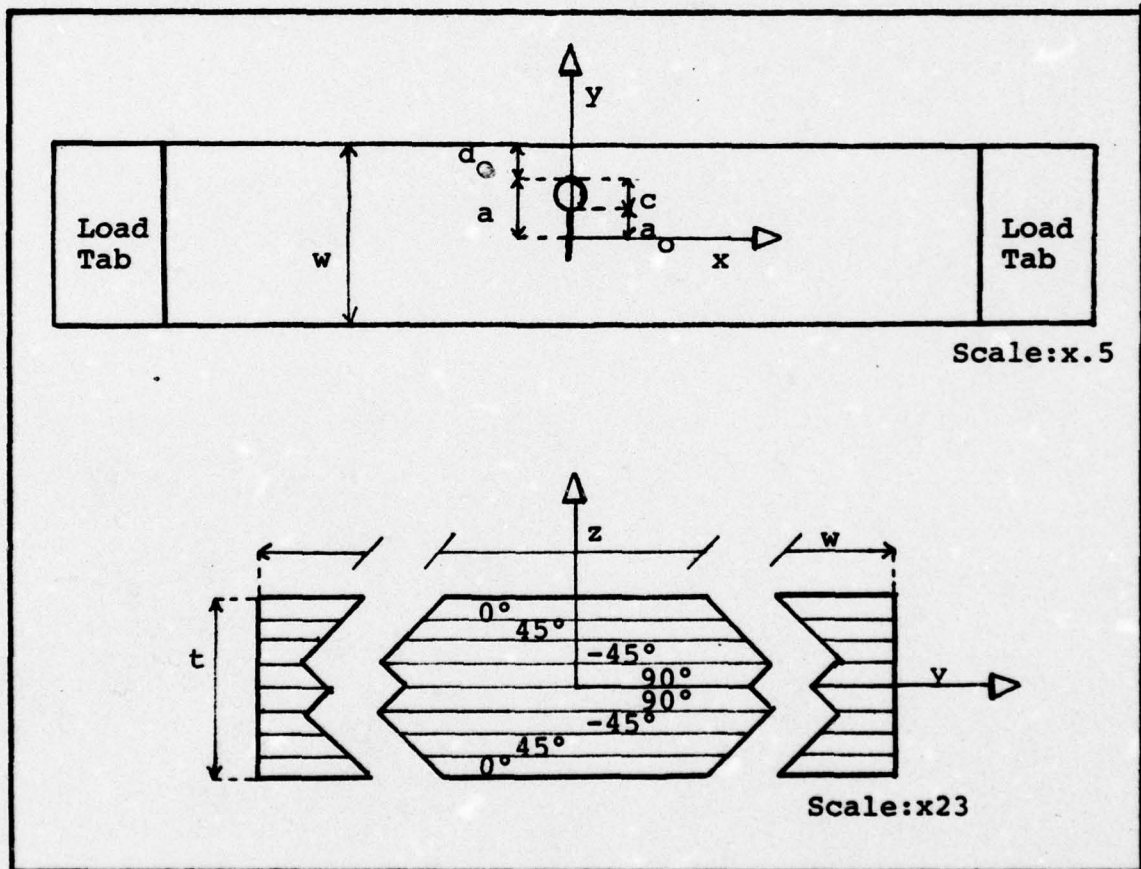


Figure 2. Specimen Geometry

As part of these experiments, radiographs were taken at various load levels. The radiographic image of the crack tip damage area was enhanced as described in Ref. 18. From these radiographs it is possible to measure the length of the subcracks in each ply of the laminate.

This thesis will use a finite element model of the experimental  $(0, \pm 45, 90)_s$  laminate with a 13mm (.51 in.) notch to analyze the growth of the crack tip damage zone. The crack tip stress and displacement fields, and the dimensions and shape of the damage zone in each ply are obtained as output. This output data is compared with subcrack dimensions obtained from the radiographs, isotropic crack stress and displacement fields, and with several models used to predict fracture strength.

The following sections explain the analysis. First, the theory behind the modelling will be explained. Next, the numerical analysis will be covered. Last, the results and conclusions based on comparisons between the analytical data and experimental data will be presented.



## II. Theory

The theoretical foundation of this analysis can be built by answering three questions. What are the implications of a two dimensional analysis of the crack tip damage zone in a composite laminate? What composite strength theory is appropriate for crack tip damage zone analysis, and how can this theory be applied? How can the modelled damage region be used to predict fracture strength?

### Implications of Two Dimensional Analysis

Several investigations have stated that the stress field around a crack in a composite plate is three dimensional [9,6,13]. The three dimensionality is caused by the interlaminar stresses at the free edge of a crack.

The effect of the free edge on the interlaminar stresses in an unnotched laminate plate under uniaxial stress has been partially explained by Pagano and Pipes. Notches, though, present a different type of free edge. This difference, coupled with the crack tip singularity, make the solution of the free edge effects along a notch extremely difficult. Therefore, any discussion on the applicability of a two dimensional analysis must be made based on the purpose of the analysis.

This analysis is concerned with modelling and analyzing the crack tip damage zone and how it relates to the fracture strength. The applicability of the two dimensional analysis can then be assessed by comparing dimensions of the damage zone and the areas

affected by interlaminar stresses, and then determining whether interlaminar stresses affect fracture strength.

Mandell, Wang, and McGarry [4] performed a finite element analysis of a single edge notched composite plate using a three dimensional finite element analysis. It should be noted that the interlaminar stresses for an edge notch are probably worse than those for a center notch since the edge notch is connected to a stress free edge. Therefore, if the effects of the interlaminar stresses are within the bounds of the damage zone for this edge case, then interlaminar stresses for a center notched specimen should be even less significant.

The results of the Mandell analysis indicate that the effect of the interlaminar stresses was confined to a distance equal to the laminate thickness along the crack flanks and was less ahead of the crack tip. Also, examination of the isostress plots reveals that the area where the interlaminar stresses were of the same magnitude as the planar stresses was much smaller. Since previous studies [10, 13, 14, 4] indicated that the damage zone was confined to the area immediately at the crack tip or ahead of it, and the damage zone at failure was much greater than the laminate thickness, the interlaminar stresses should not affect the boundary of the damage zone.

In reference [19], the effects of interlaminar stresses on the fracture strength of center notched laminated plates was studied experimentally. This study showed that the interlaminar stresses had no effect on the fracture strength of a center notched plate.



In light of previous work, it seems feasible to use a two dimensional analysis to model the boundary of the damage zone in a center notched laminated plate. Furthermore, the stress field value outside a region equal to a laminate thickness from the crack should be accurate.

### Strength Determination

In general for any material, strength is a measure of the ability to deform without sustaining irreversible damage. In homogeneous isotropic materials, this ability is measured by the yield criterion, where the yield strength is the point where the material ceases to act elastically. The yield criterion defines a hypersurface against which various loading conditions can be evaluated [20,21].

Several studies have modelled the behavior of a unidirectional composite as linear to failure [9, 22, 23, 24]. Drawing a parallel with plasticity theory, it can then be surmised that the combinations of stresses which represent lamina failure can be represented by a hypersurface in stress space [17]. Lamina failure is defined as the inability of the lamina to carry stress in the same manner as it did in its virgin state.

After putting laminae together to form a laminate, the behavior of the laminate is no longer linear to failure. Instead it can be assumed that failure of the laminate occurs when all of its constituent laminae have failed [9, 17].

There are two basic types of criteria which have been developed to describe the plastic yield surface, non-interacting and

interacting [17]. In the non-interacting criteria, such as maximum stress or maximum strain, multiaxial stress does not affect uniaxial strength [21]. For the interacting criteria, such as the von Mises or Tresca criteria, the yield surface is determined by the total stress tensor. Since this analysis deals with a high strength graphite epoxy and examination of failure curves for high strength graphite-epoxy specimens [25] reveals a high degree of interaction, the non-interacting criteria will not be used in this analysis.

There are basically two interaction theories which have been developed for homogeneous, anisotropic materials. One is the Tsai-Hill theory [20, 22], in which the failure surface is defined by

$$F(\sigma_2 - \sigma_3)^2 + G(\sigma_3 - \sigma_1)^2 + H(\sigma_1 - \sigma_2)^2 + 2L\tau_{23}^2 + 2M\tau_{31}^2 + 2N\tau_{12}^2 = 1 \quad (1)$$

where  $F$ ,  $G$ ,  $H$ ,  $L$ ,  $M$ , and  $N$  are failure strength parameters. The other theory is the Tsai-Wu tensor theory, in which the failure surface is defined by

$$F_i \sigma_i + F_{ij} \sigma_i \sigma_j + F_{ijk} \sigma_i \sigma_j \sigma_k + \dots = 1 \quad (2)$$

where  $F_i$  and  $F_{ij}$  are strength tensors of the second and fourth order respectively [9]. Although more general than the Tsai-Hill criterion, the Tsai-Wu criterion is more complicated and requires extensive testing to determine the values of the strength tensors. Since this work is analytical and further testing is required to determine the strength tensor, the Tsai-Hill criterion will be used since the failure strength parameters can be determined from the uniaxial strengths for



the two dimensional case [22] such that the criterion becomes

$$\frac{\sigma_1^2}{X^2} - \frac{\sigma_1 \sigma_2}{X^2} + \frac{\sigma_2^2}{Y^2} + \frac{\sigma_{12}^2}{S^2} = 1 \quad (3)$$

where X is axial strength, Y is transverse strength and S is shear strength.

When the Tsai-Hill criterion is used, extreme caution is required for two reasons [22]. First, this criterion is based on a distortional energy approach where hydrostatic pressures do not cause yielding [20]. It has been shown that composites do yield under hydrostatic loading due to the misalignment of the principle stress and principle strain directions [23]. Second, the criterion, as stated, does not account for differences between compressive and tensile strengths. The effect of these deviances can be found by examining the applicability of the criterion to the material being analyzed.

This criterion is phenomenological in nature; therefore, the applicability of the criterion must be judged against its ability to predict failure for the particular laminate under study. It will be shown that the Tsai-Hill criterion can be used to predict uniaxial failure of the  $(0, \pm 45, 90)_s$  graphite-epoxy laminate used in this analysis; therefore, it will be assumed that the problems arising out of yielding under hydrostatic loading do not significantly affect strength predictions.

The difference in tensile and compressive failure strengths can be included by using a simple procedure [9]. If the stress field includes compressive stresses, the compressive failure strength is used for that component of the stress field, otherwise

the tensile failure strength is used in the criterion.

Before this criterion can be applied to a laminate, a determination must be made as to how to treat constituent lamina failure when it occurs prior to total laminate failure. There are various methods to predict laminate failure, the most appropriate is the use of the individual failure characteristics of the laminae to predict laminate failure through progressive lamina failure [9, 17, 24]. As a lamina fails, the equivalent stiffness for the laminate is changed by modifying the constituent lamina stiffness.

There are basically three methods to modify the laminate stiffness [17]. There is the total discount method where the failed ply is assigned zero stiffness and strength. Second, there is the mode limited discount method where zero stiffness and strength are assigned to the transverse and shear modes if the failure occurs only due to transverse or shear stresses, and the strength and stiffness in all modes is discounted if the failure is due to longitudinal stresses. In the third method, the failed lamina is assigned residual properties.

Since the exact lamina failure mechanisms and the post failure performance of the lamina in a laminate are not completely understood, this analysis uses a bounding theory to portray failure in the crack tip damage zone. It is obvious that one extreme bound on the damage zone can be found if all lamina are treated as elastic until failure occurs (elastic method), and the other extreme bound is determined by completely discounting all stiffness of a ply when the stress field in



that ply exceeds the failure criterion.

The appropriateness of two dimensional analysis, the Tsai-Hill failure criterion, the progressive lamina failure approach to predict laminate failure, and the boundedness assumption made in the analysis can be illustrated by applying these procedures to an unnotched specimen under tension. The properties of the graphite-epoxy specimen used are shown in Table I.

Table I			
Lamina Properties			
Elastic Constants		Ultimate Strengths	
t	.0436 in.	X <sub>t</sub>	217.6 ksi
E <sub>11</sub>	15545 ksi	X <sub>c</sub>	217.6 ksi
E <sub>22</sub>	1425 ksi	Y <sub>t</sub>	5.8 ksi
G <sub>12</sub>	903 ksi	Y <sub>c</sub>	35.7 ksi
v <sub>12</sub>	.288	S	9.9 ksi

The ultimate strength of the (0, +45, 90)<sub>s</sub> laminate was 54.4 ksi.

Using these properties and the procedures mentioned previously, the ultimate strength of the laminate was predicted. The loading curve is shown in Fig. 3, and the resultant forces and strains at the knees are shown in Table II. The upper line represents the curve obtained if all lamina remain elastic until all lamina have failed. The middle curve uses the mode limited discount method, and the lower curve uses the total

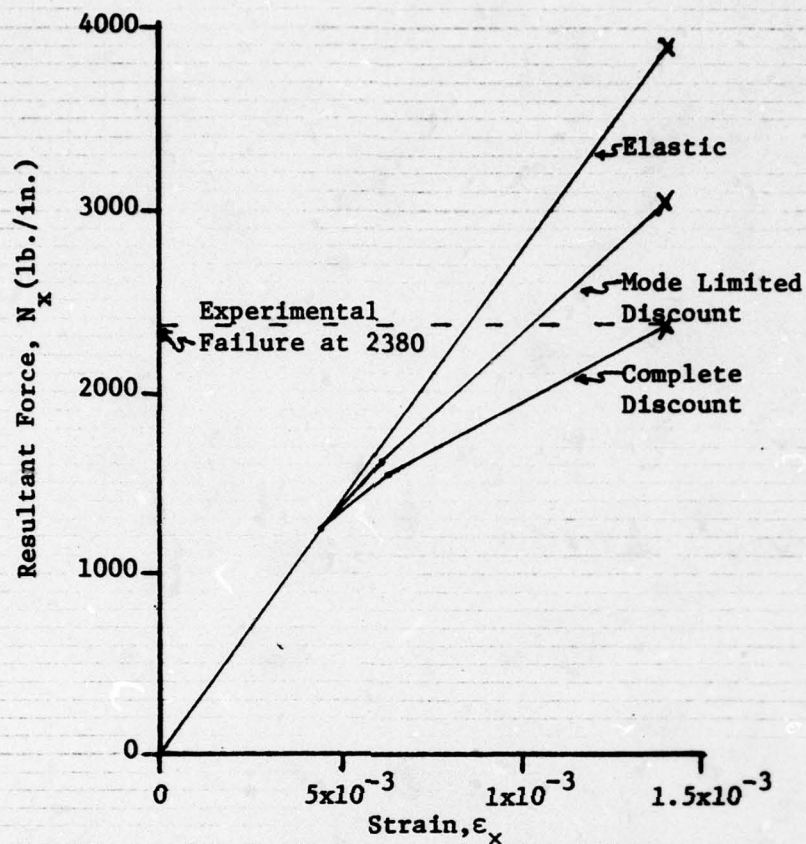


Figure 3. Loading Curve Showing Difference Between Discounting Methods.

Table II						
Loading Curve Data						
Ply Which Fails	Elastic Method		Mode Limited Discount Method		Complete Discount Method	
	$N_x$ (lb./in.)	$\epsilon_x$	$N_x$ (lb./in.)	$\epsilon_x$	$N_x$ (lb./in.)	$\epsilon_x$
90°	1230	$4.4 \times 10^{-3}$	1230	$4.4 \times 10^{-3}$	1230	$4.4 \times 10^{-3}$
+45°			1620	$6.1 \times 10^{-3}$	1470	$6.2 \times 10^{-3}$
0°	3900	$14.0 \times 10^{-3}$	3070	$14.0 \times 10^{-3}$	2370	$14.0 \times 10^{-3}$



discount method.

As can be seen, the elastic method is an upper bound on failure, and the total discount method does provide a lower bound. The closeness of the lower bound to the actual strength suggests that the ability of the composite to handle loads is severely degraded when transverse or shear failure occurs as is assumed in the total discount method.

In summary, failure in the damage zone will be bounded using the elastic method and the complete discount method. Lamina failure will be defined using the Tsai-Hill criterion.

#### Application of Numerical Analysis Results

The goal of a fracture analysis is to predict in what fashion and when catastrophic failure will occur. The manner of failure can be correlated with either crack propagation or the growth of a damage zone at the crack tip. The "when" of ultimate failure is explained by the fracture stress if strain rates and other time related phenomena are ignored. The phenomena correlated with these two questions will be discussed in the following paragraphs.

Since crack extension did not occur for the tests being analyzed, the investigation must concentrate on explaining the growth of the damage zone. Two specific phenomena are related to the growth of the damage zone. The unobservable phenomenon is the growth of the failure area around the crack tip. This phenomenon is described by the dimension,  $c$ , of the failure

area or damage zone where all plies have failed, the laminate damage zone. In this laminate, this zone coincides with the dimension of the  $0^\circ$  damage zone measured colinear with the original notch and can only be found through numerical analysis. The observable occurrence is the growth of subcracks along ply fibers [4, 13].

It is questionable whether the growth of subcracks and the fracture stress are directly related [4]. It has been shown, though, that the length of the subcracks is proportional to the opening mode stress intensity factor, squared,  $K_I^2$  [4]. The average length of the ply subcracks can be obtained from radiographs of the crack tip damage zone, as can be seen in Fig. 4, 5, 6, 7, 8, and 9. Since  $K_I^2$  is proportional to the strain energy release rate,  $\mathcal{G}$  [5, 26], it is also possible to relate  $\mathcal{G}$  to the ply subcrack length. Values of  $K_I$  and  $\mathcal{G}$  can be found using the finite element analysis where the crack extension is equal to the growth of the laminate damage zone. This correlation indirectly relates the growth of the modelled damage and the growth of the ply subcracks, which can only be measured through experiments.

Since the damage zone in laminates is analogous to the crack tip plastic zone in metals, the following expression can be used to calculate  $K_I$  in a center notched, finite width plate [27].

$$K_I = \sigma \left( w \tan \frac{\pi a}{w} \right)^{\frac{1}{2}} \quad (4)$$



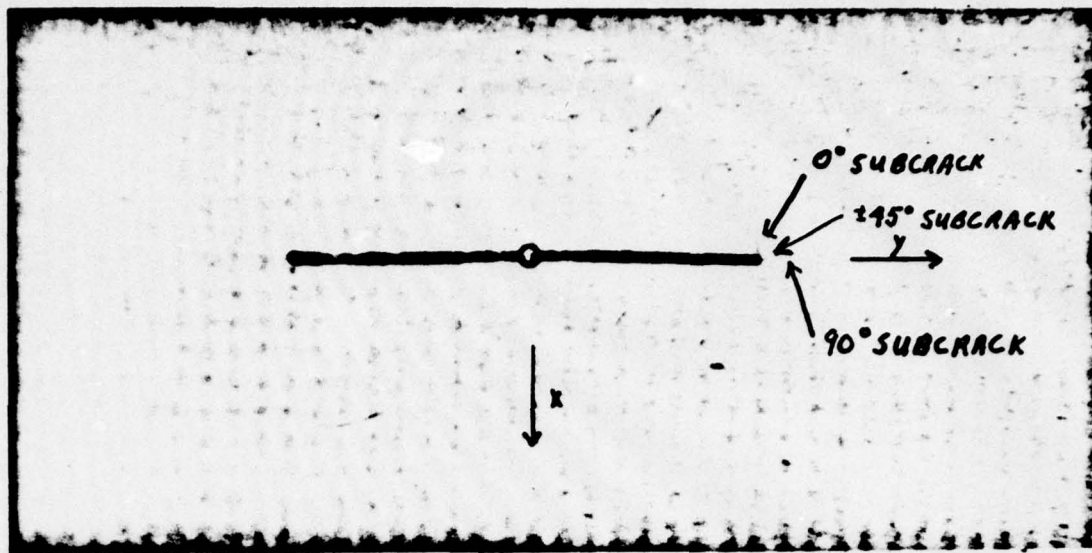


Figure 4. Enhanced Radiographic Image of Ply Subcracks at 50% of the Experimental Fracture Load, Approximately Five Times Actual Size.

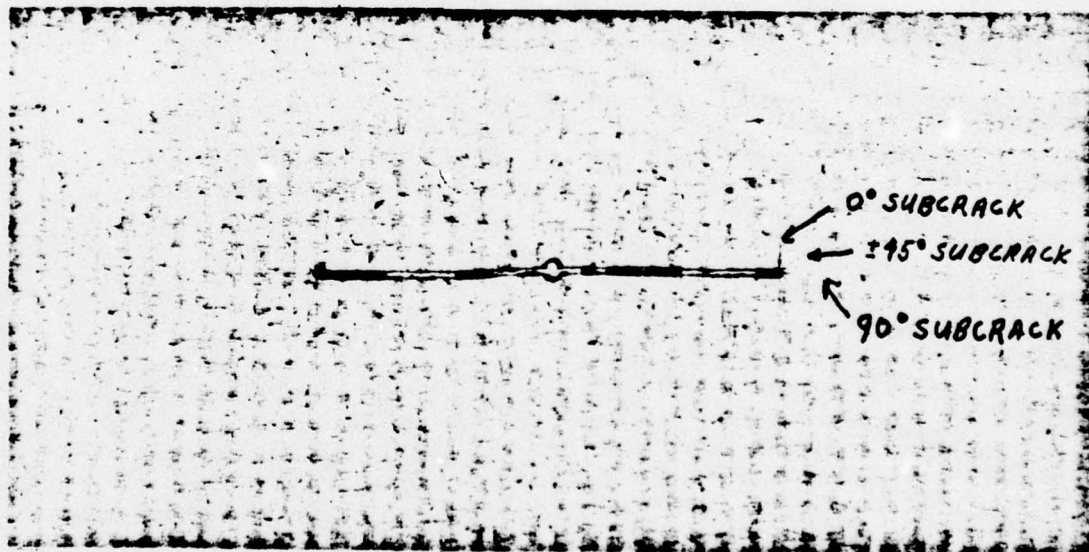


Figure 5. Enhanced Radiographic Image of Ply Subcracks at 60% of the Experimental Fracture Load, Approximately Five Times Actual Size.

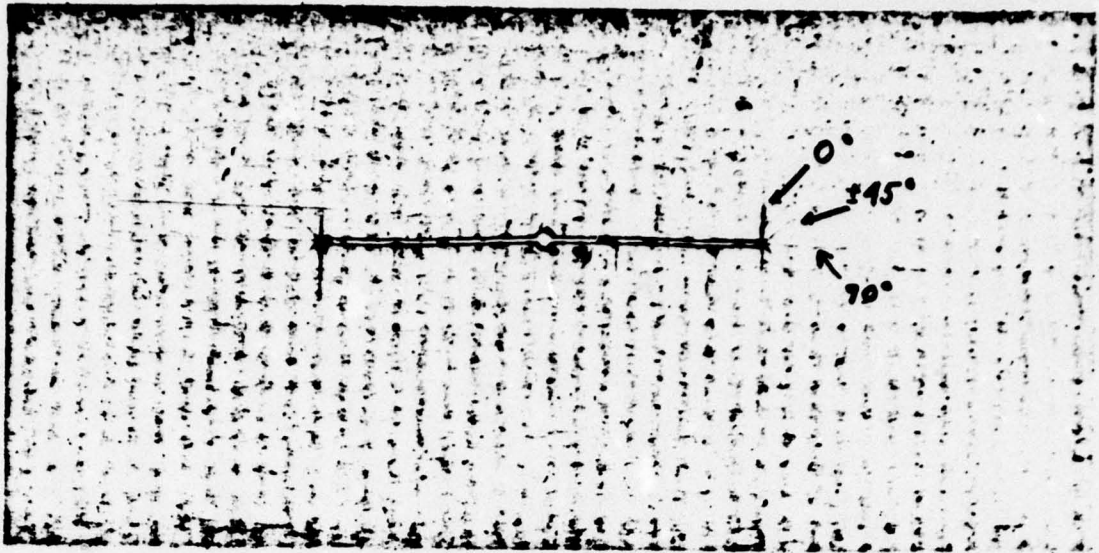


Figure 6. Enhanced Radiographic Image of Ply Subcracks at 70% of the Experimental Fracture Load, Approximately Five Times Actual Size.

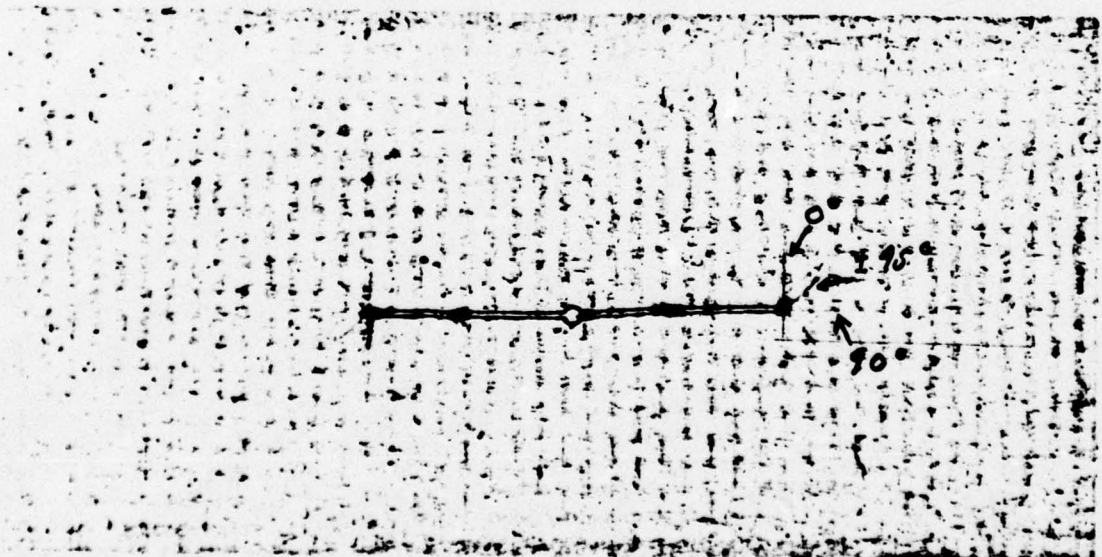


Figure 7. Enhanced Radiographic Image of Ply Subcracks at 80% of the Experimental Fracture Load, Approximately Five Times Actual Size.



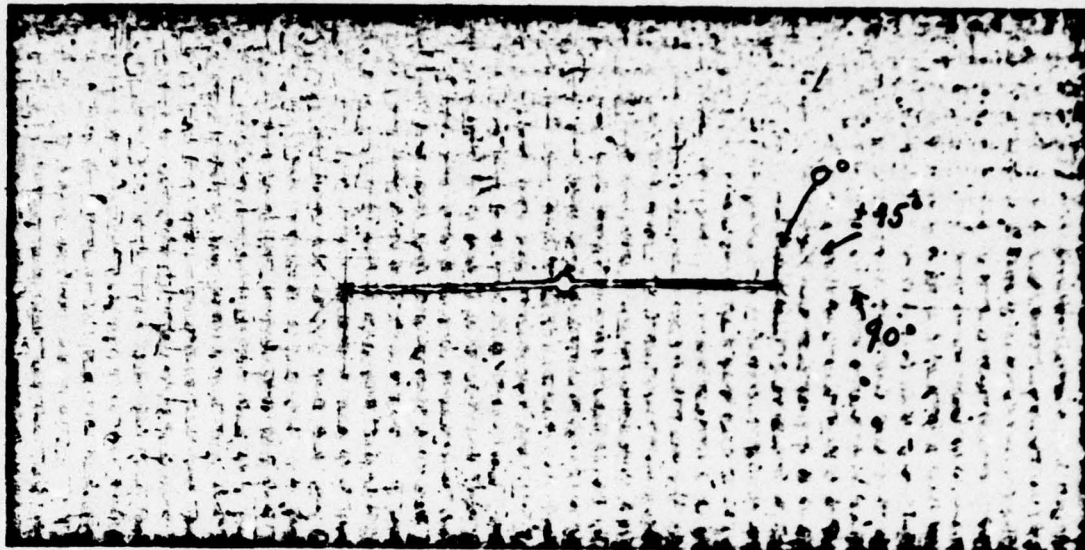


Figure 8. Enhanced Radiographic Image of Ply Subcracks at 90% of the Experimental Fracture Load, Approximately Five Times Actual Size.

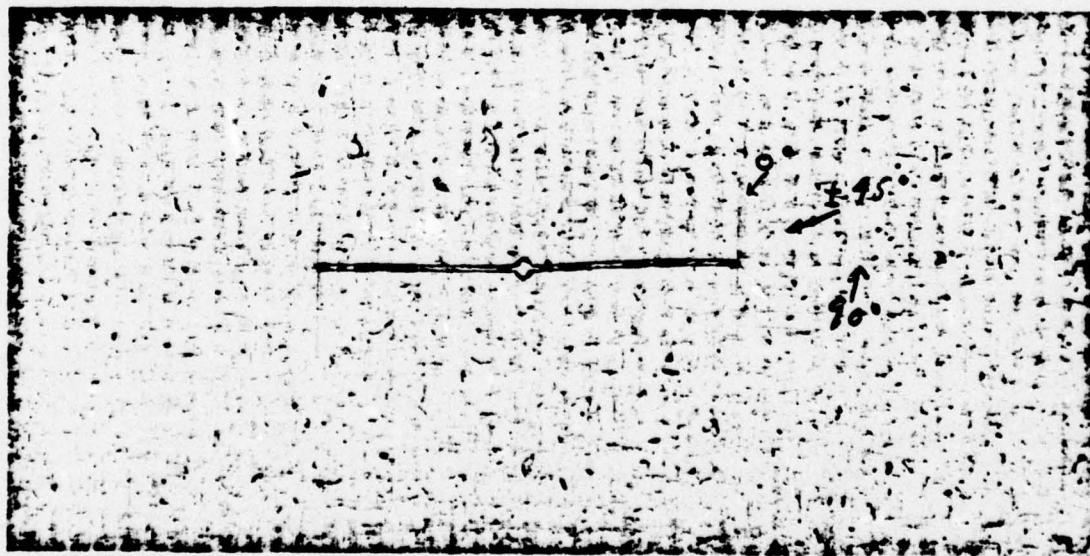


Figure 9. Enhanced Radiographic Image of Ply Subcracks at 95% of the Experimental Fracture Load, Approximately Five Times Actual Size.

In this expression,  $\sigma$  is the applied stress,  $w$  is the plate width, and  $a$  is the effective crack half-length. The effective crack half-length is the sum of the original crack half-length,  $a_0$ , and the size of the damage zone,  $c$ , measured collinear with the original notch, see Figure 2.

$$a = a_0 + c \quad (5)$$

With this relation and the results from the finite element analysis, it is possible to calculate  $K_I$  for each loading increment. Since the subcrack length can be related to the loading increment, it is then possible to correlate  $K_I^2$  and the ply subcrack lengths.

Various studies have used a finite element analysis to determine the strain energy release rate [6, 28]. It has been shown that [5, 6]

$$\mathcal{G} = \frac{P^2}{2} \frac{dC}{da} \quad (6)$$

where  $P$  is the applied load and  $\frac{dC}{da}$  is the rate of change of structural compliance with crack extension. From the finite element analysis in which element plies are removed as they fail, load-displacement diagrams are obtained similar to those shown in references [14] and [27] and in Fig. 10. As the damage zone increases the compliance changes. The compliance can be calculated by assuming the displacement at the load



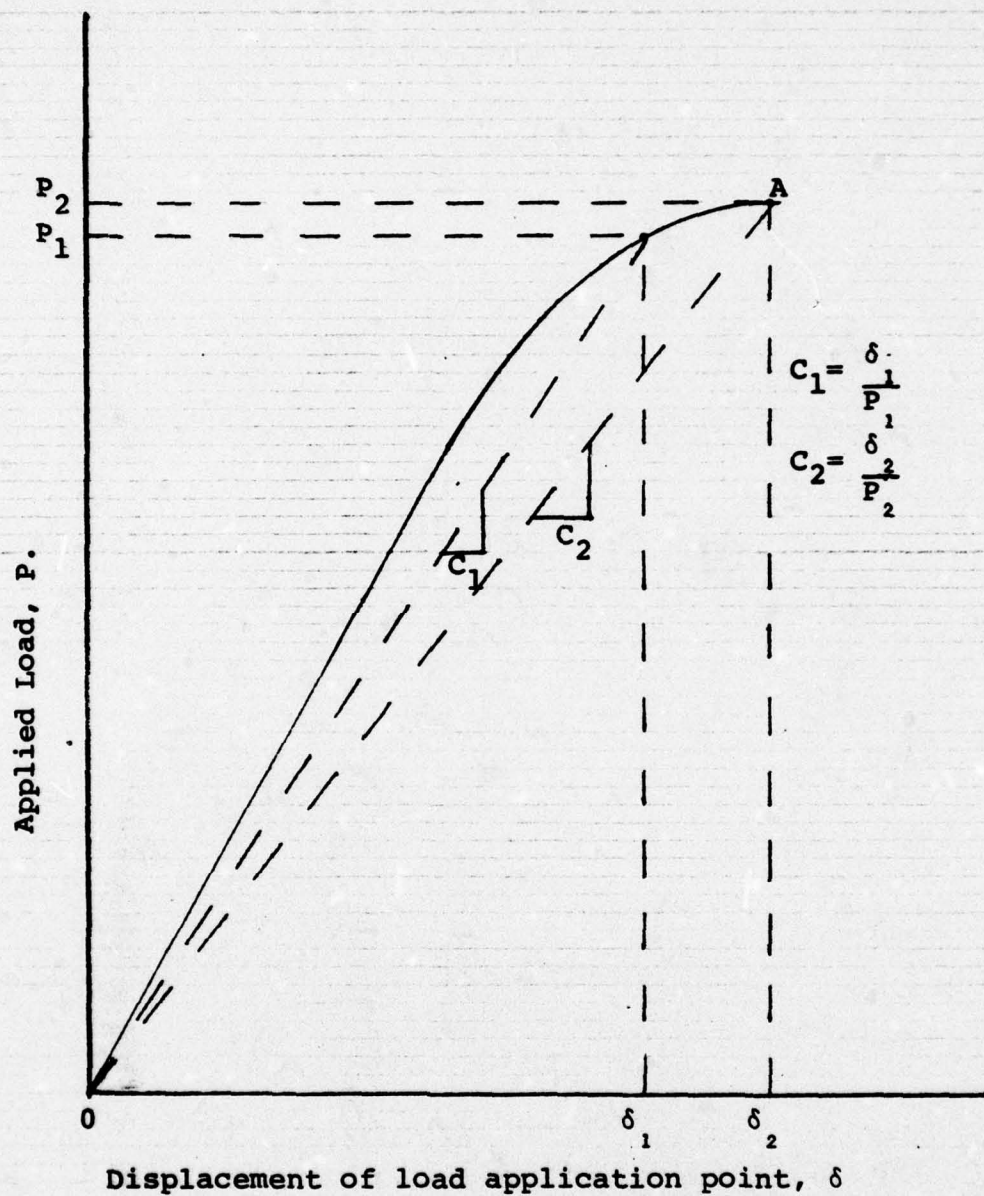


Figure 10. Load displacement diagram used to calculate  $\bar{y}$ .

application point returns to zero as the load is relaxed, line AO. The inverse of the slope of this line is the new compliance,  $C_2$ . The change in crack extension is the difference between the equivalent crack length  $2a_2$  and the previous equivalent crack length  $2a_1$ . The derivative can then be approximated by

$$\frac{dC}{da} = \frac{C_2 - C_1}{2a_2 - 2a_1} \quad (7)$$

The equivalent strain energy release rate is approximated by

$$= \frac{P_2^2}{2} \left( \frac{C_2 - C_1}{2a_2 - 2a_1} \right) \quad (8)$$

The second goal, of predicting when fracture will occur, can be approached in three manners. Two of these, the use of a critical stress intensity factor and instability analysis are classical in nature, and the third is introduced, for the first time, in this thesis. The third method involves the relation between combinations of load and load bearing area which result in stresses above the ultimate stress.

In a previous work [13], Hahn predicted that  $K_C/\sigma_0$  is between .7393 in.<sup>1/2</sup> and .7663 in.<sup>1/2</sup> for the specimen being analyzed, where  $K_C$  is the critical opening mode stress intensity factor and  $\sigma_0$  is the unnotched tensile strength. Using these values and the unnotched tensile strength of



54.4 ksi, the range for  $K_c$  is obtained as

$$40.22 \text{ ksi-in.}^{\frac{1}{2}} < K_c < 41.67 \text{ ksi-in.}^{\frac{1}{2}} \quad (9)$$

Using equations (4), (5), and (9) and the dimensions of the damage zone obtained from the finite element analysis, the failure load can be predicted.

The instability method of predicting fracture strength is the simplest to apply. The load-displacement curve for the sequence of loading where element plies within the failure region are removed is plotted, Fig. 11. The increment of load which causes the curve to transition from the non-linear region, II, to the flat region, III, is defined as the instability load, and the preceding load is taken as the fracture strength.

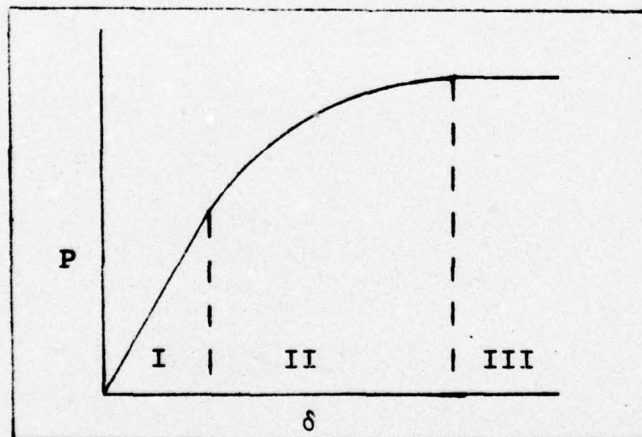


Figure 11. Instability Load Displacement Diagram

The last method is based on logic similar to that presented in an article by Nuismer and Whitney [29]. The average stress criteria predicts failure when the average value of stress,  $\sigma_a$ , over some fixed distance,  $d_o$ , ahead of the crack first reaches the unnotched tensile strength,  $\sigma_o$ . In equation form, failure occurs when

$$\frac{1}{d_o} \int_a^{a+d_o} \sigma_x(0,y) dy = \sigma_o \quad (10)$$

where  $d_o$  is the fixed distance ahead of the crack,  $a$  is the crack length, and  $\sigma_x$  is the perpendicular, normal stress component ahead of the crack tip. Clearly the average stress is represented by the left side of equation (10). For a center notched plate, Fig. 2, equation (10) must hold at both ends of the crack, and the normal stress perpendicular to the crack flanks must be zero; therefore,

$$\sigma_a = \frac{1}{2d_o} \int_{-a-d_o}^{a+d_o} \sigma_x dy \quad (11)$$

The equation as presented in the referenced paper predicted the notched strength for an infinite plate with a center notch. For the finite plate being analyzed, it is assumed that  $d_o$  is the distance from the boundary of the damage zone to the plate edge.

$$2d_o = W - 2a \quad (12)$$

Further, if it is assumed that the effective crack length is the sum of the initial notch length,  $a_o$ , and the dimension of



the damage zone colinear with the original notch,  $c$ , such that

$$a = a_o + c \quad (13)$$

From Fig. 2, it can be seen that

$$-\frac{w}{2} = -a - d_o \quad (14)$$

$$\frac{w}{2} = a + d_o \quad (15)$$

$$2d_o = w - 2a_o - 2c \quad (16)$$

Incorporating equations (14), (15), and (16) into equation (11)

$$\sigma_a = \frac{1}{w - 2a_o - 2c} \int_{-\frac{w}{2}}^{\frac{w}{2}} \sigma_x dy \quad (17)$$

From classical laminated plate theory

$$N_x = \int_{-t/2}^{t/2} \sigma_x dz \quad (18)$$

where  $N_x$  is the resultant force per unit length, and  $t$  is the laminate thickness. Now integrating equation (17) across the thickness of the plate the following is obtained

$$\int_{-t/2}^{t/2} \sigma_a dz = \int_{-t/2}^{t/2} \frac{1}{w - 2a_o - 2c} \int_{-\frac{w}{2}}^{\frac{w}{2}} \sigma_x dy dz \quad (19)$$

assuming sufficient continuity in  $\sigma_x$  and that  $w$ ,  $a_o$ , and  $c$  are constant through the thickness, equation (19) is rewritten as

$$\int_{-t/2}^{t/2} \sigma_a dz = \frac{1}{w - 2a_o - 2c} \int_{-\frac{w}{2}}^{\frac{w}{2}} \int_{-t/2}^{t/2} \sigma_x dz dy \quad (20)$$

By the definition of the averaging process,  $\sigma_a$  is constant through the thickness, therefore

$$\int_{-t/2}^{t/2} \sigma_a dz = \sigma_a t \quad (21)$$

From equations (18) and (19)

$$t\sigma_a = \frac{1}{w-2a_o-2c} \int_{-\frac{w}{2}}^{\frac{w}{2}} N_x dy \quad (22)$$

From energy considerations, the integral of the resultant force in the x direction integrated over a line perpendicular to the x-axis must equal the applied load in the x direction,  $P_{ax}$ ,

$$\int_{-\frac{w}{2}}^{\frac{w}{2}} N_x dy = P_{ax} \quad (23)$$

Substituting equation (23) into (22)

$$t\sigma_a = \frac{1}{w-2a_o-2c} P_{ax} \quad (24)$$

or

$$\sigma_a = \frac{1}{t(w-2a_o-2c)} P_{ax} \quad (25)$$

Defining the quantity,  $t(w-2a_o-2c)$ , as the remaining load bearing area,  $A_{LB}$ , and substituting equation (25) and into equation (10), the following condition will define fracture strength

$$\frac{P_{ax}}{A_{LB}} = \sigma_o \quad (26)$$

To find the fracture strength for a particular material, equation (26) is applied to a load versus load-bearing area



diagram, Fig. 12. The boundary of the failure region is the line defined by

$$\frac{P}{A} = \sigma_0 \quad (27)$$

As damage progresses from the crack tip, the load bearing area decreases. If load and remaining load bearing area are plotted as shown in Fig.12, the predicted fracture strength is the intercept between this curve and the boundary of the failure region. Referring to the boundedness argument presented in the Strength Determination, the elastic method yields an upper bound on strength, and the complete discount method yields a lower bound

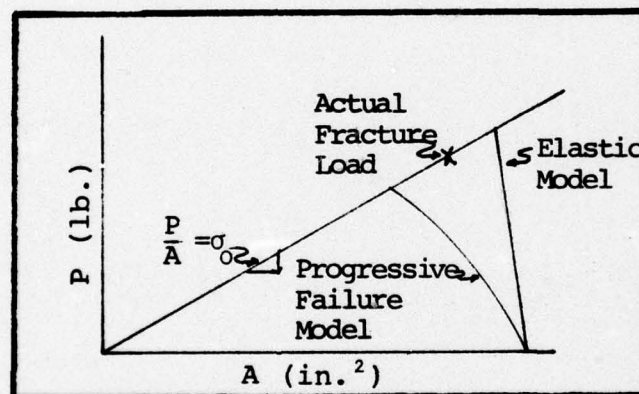


Figure 12. Applied Load Versus Load Bearing Area.

This is the last section of the theory chapter. Now that the theory behind the application of the numerical results has been built, it is necessary to establish the foundation of the finite element modeling which was done to obtain the results.

### III. Numerical Analysis Description

The analysis generated in this thesis is based on data obtained through a finite element method. In this section, the finite element method used and the method employed to determine the size of the damage zone in each ply will be discussed.

#### Finite Element Model

To apply some of the methods of LEFM or to obtain the exact stresses and displacements around a crack tip, an exact elasticity solution is required [30]. Since exact solutions for composite problems are difficult, if not impossible, to obtain, it is appropriate to use approximate numerical methods to analyze composite fracture.

The finite element program used in this thesis was developed at the Air Force Flight Dynamics Laboratory [31]. The program is based on classical laminated plate theory and the displacement method of finite element analysis. This program could be used to analyze plies of several different combinations, one of which was  $(0, \pm 45, 90)_s$ , and included various standard elements, including the constant strain triangle. The element stiffness matrix is modified by either changing the relative percentage of the plies contained in the element laminate or by changing the element material.



There are many areas that should be considered when constructing a finite element model [32]. These many areas can be condensed to four questions when considering a specific problem:

- 1) What mesh model is best for the given problem?
- 2) How can symmetry and boundary conditions be incorporated in the model?
- 3) How accurate are the results and has the solution converged to the exact solution?
- 4) What do the stresses and strains which result from the model actually mean?

These questions will now be answered as they apply to a center crack in a laminated, composite plate.

In the finite element analysis of cracks either standard elements are used and the mesh around the crack is refined to account for the high stress gradients, or a special crack tip element is used which models the theoretically infinite stress at the crack tip. Since it is not absolutely proven that all ply stresses are infinite at the crack tip in composites, and the notch which simulates a crack does not extend, the standard constant strain triangle is used in this analysis.

When elements such as the constant strain triangle are used, it is necessary to refine the elements in the vicinity of the crack. In one work which studied the effect of element size [30], it was found that accurate results could be obtained by reducing the element size in the vicinity of the crack so that the ratio of element area to crack length squared  $\left(\frac{A_E}{a^2}\right)$  was between  $1.2 \times 10^{-6}$  and  $20 \times 10^{-6}$ . These ratios resulted in approximately five percent error in the determination of the isotropic stress intensity factor. For this analysis two

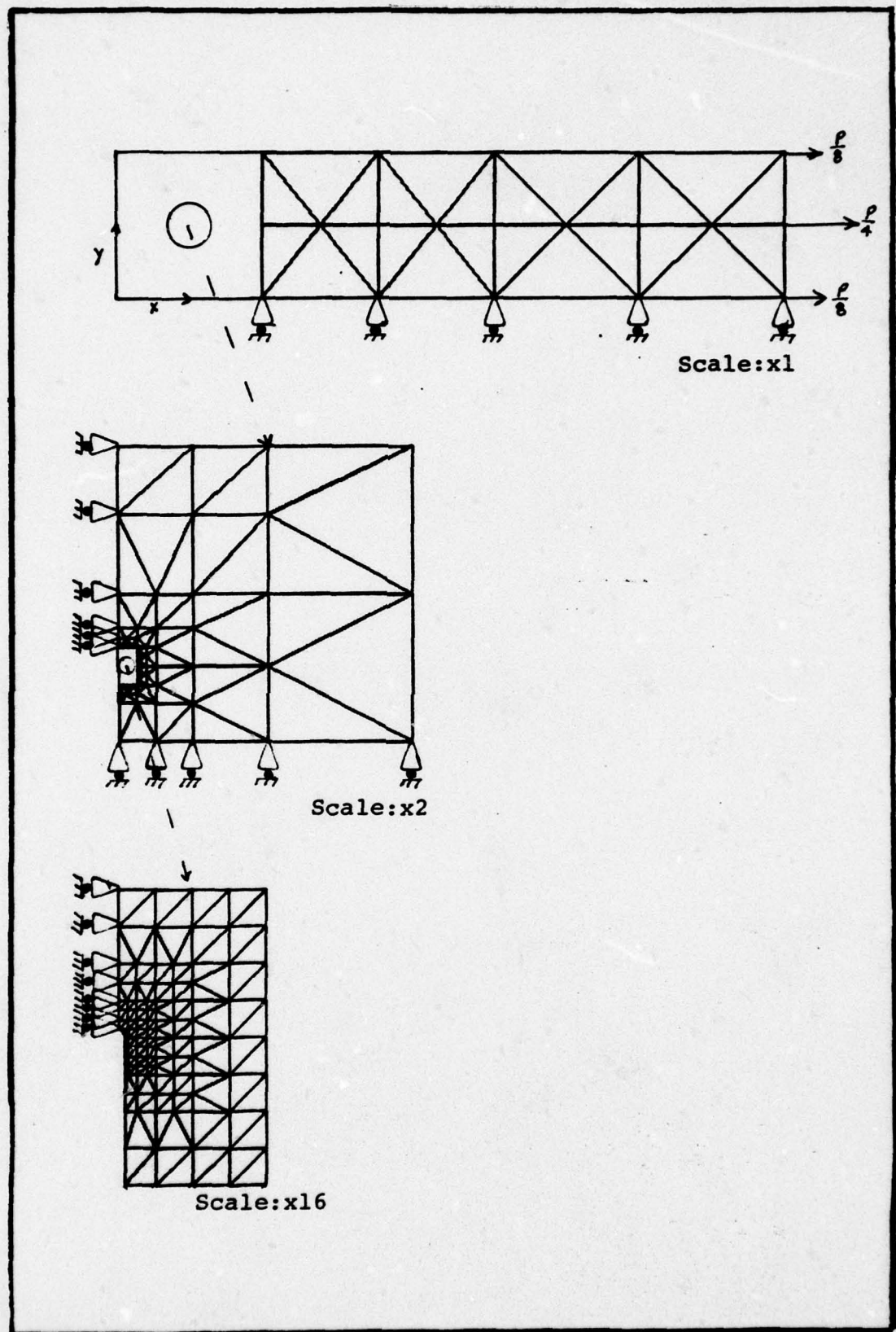


Figure 13. First Mesh 163 Nodes, 282 Elements



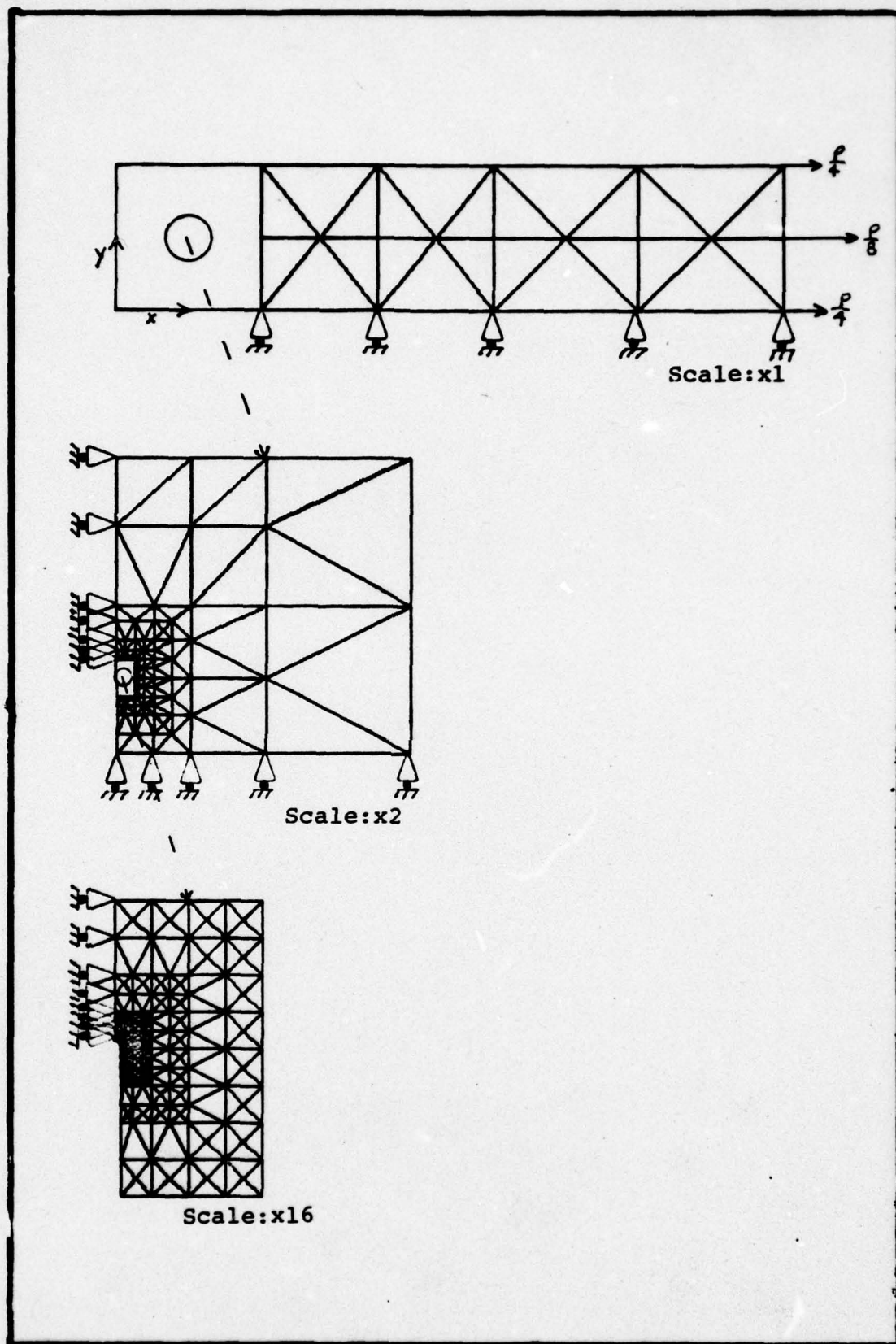


Figure 14. Second Mesh 252 Nodes, 457 Elements

finite element meshes were generated making use of the information presented in reference 30. In the first, Figure 13, with 163 nodes and 282 elements, the  $\frac{A_E}{a^2}$  ratio was approximately  $20 \times 10^{-6}$ . In the second, Figure 14, with 252 nodes and 457 elements, the  $\frac{A_E}{a^2}$  ratio was  $10 \times 10^{-6}$ . The accuracy of these two meshes when applied to the composite crack problem was assessed by checking stress convergence.

Before these element grids could be checked for convergence, the symmetry and boundary conditions had to be investigated. Since this is a two dimensional analysis and no bending loads were applied, the lamina stacking sequence did not affect the solution; therefore, it is possible to assume symmetry about both the x-axis and the y-axis. Due to symmetry, it is only necessary to model one quarter of the plate. The boundary conditions required are to restrain the y-displacements along the x-axis and the x-displacements along the y-axis as shown in Figures 13 and 14.

The values of  $N_x$  were calculated for both meshes along the radial line running from the crack tip parallel to the x-axis in order to check for convergence. As can be seen in Figure 15, the meshes yield values that are essentially the same except in the immediate vicinity of the crack tip.

To check the second mesh for accuracy, the values of  $N_y$  along the radial line running from the crack tip parallel to the x-axis were numerically integrated, Fig. 16, and the values of  $N_x$  along the crack flank parallel to the y-axis were integrated, Fig. 17. From energy considerations, it is obvious that



NO. 340R-L410 DIETZGEN GRAPH PAPER  
SEMI-LOGARITHMIC  
4 CYCLES X 10 DIVISIONS PER INCH

EUGENE DIETZGEN CO.  
MADE IN U. S. A.

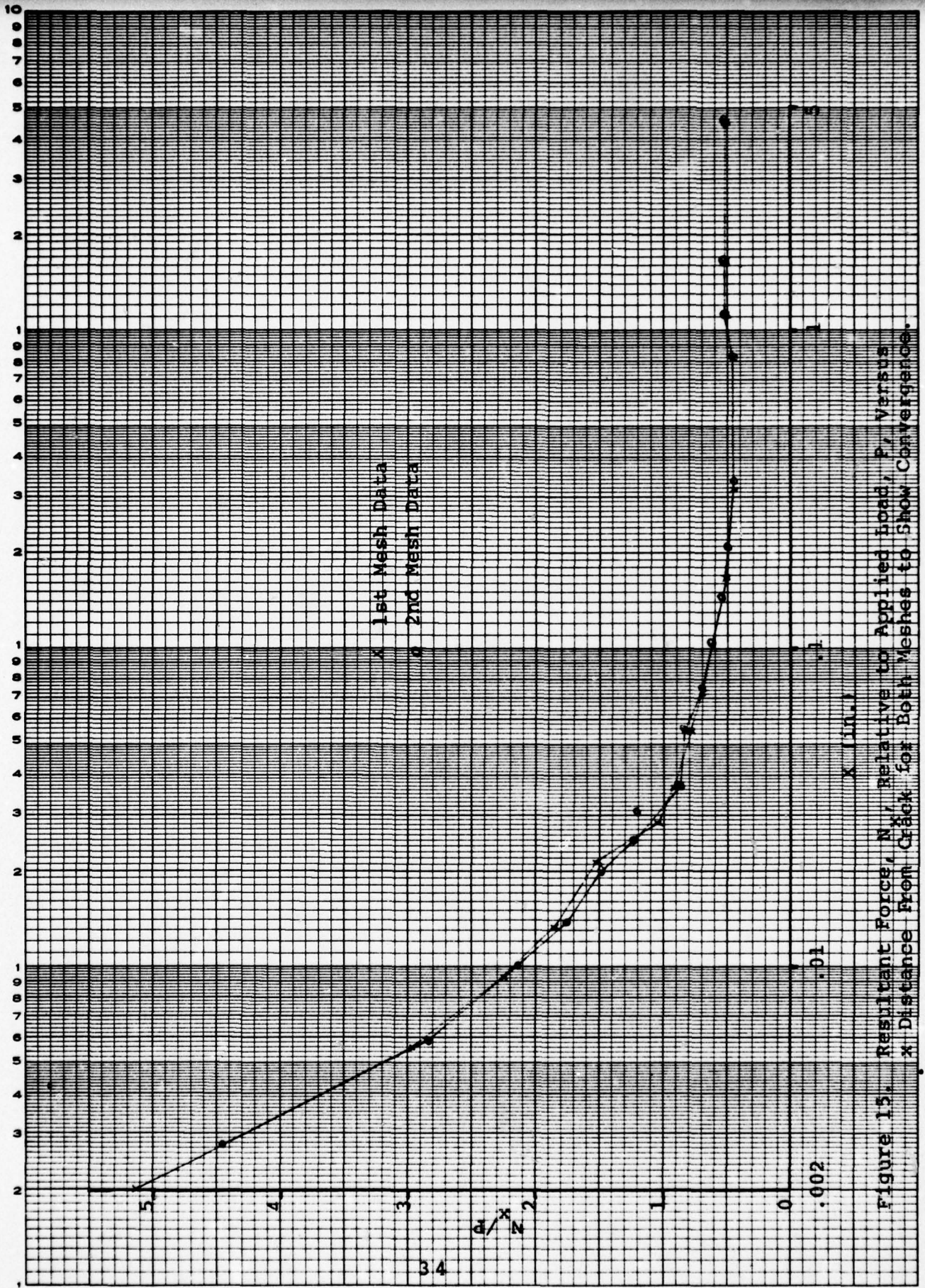


Figure 15. Resultant Force,  $N$ , Relative to Applied Load,  $P$ , Versus Distance From Crack for Both Meshes to Show Convergence.



EUGENE DIETZGEN CO.  
MADE IN U. S. A.

NO. 340R-L410 DIETZGEN GRAPH PAPER  
SEMI-LOGARITHMIC  
4 CYCLES X 10 DIVISIONS PER INCH

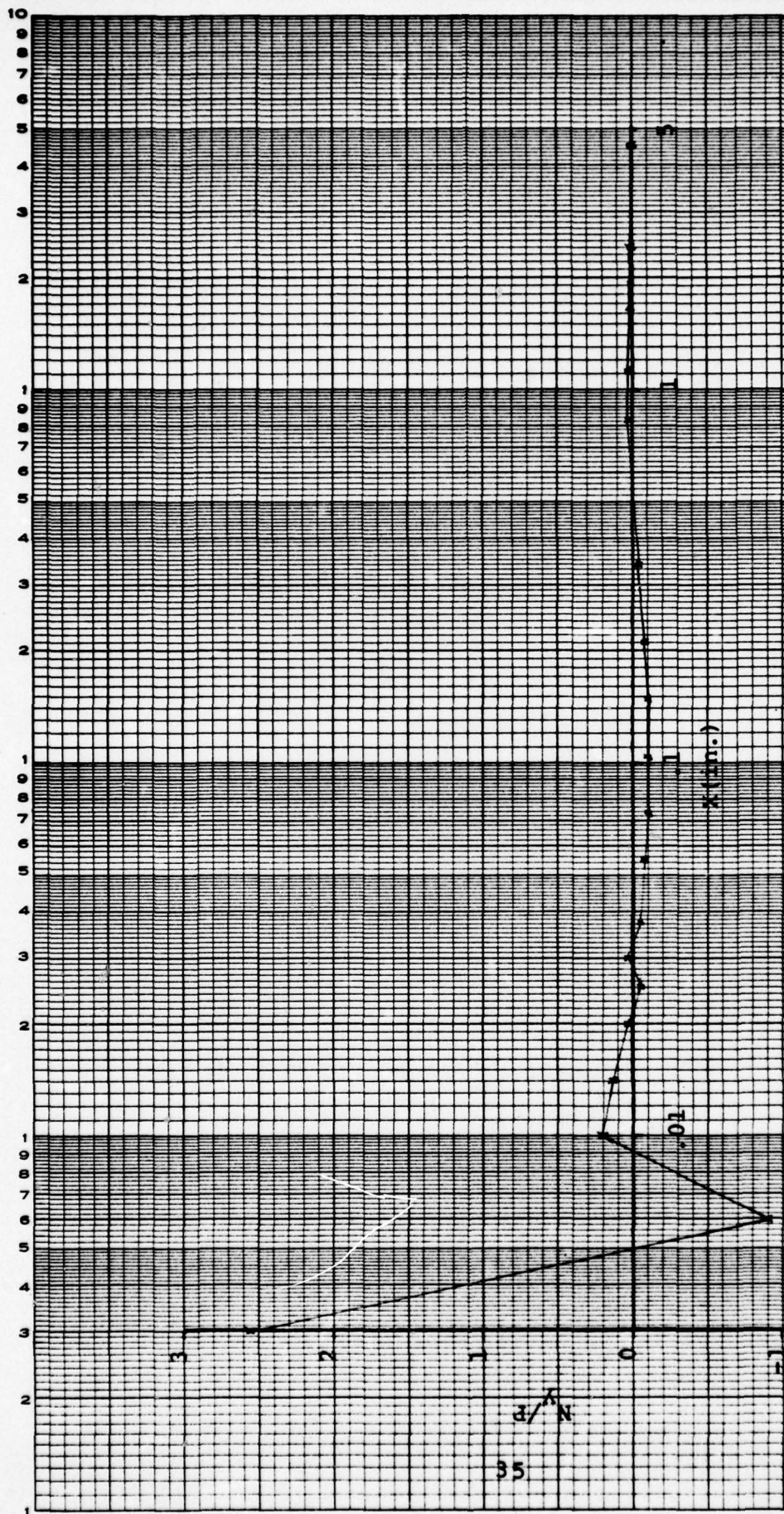


Figure 16. Resultant force,  $N/P$ , Relative to Applied load,  $P$ , Versus  
Distance from Crack for Second Mesh, to Show Values  
Used for Integration.



EUGENE DIETZGEN CO.  
MADE IN U. S. A.

NO. 340R-L410 DIETZGEN GRAPH PAPER  
SEMI-LOGARITHMIC  
4 CYCLES X 10 DIVISIONS PER INCH

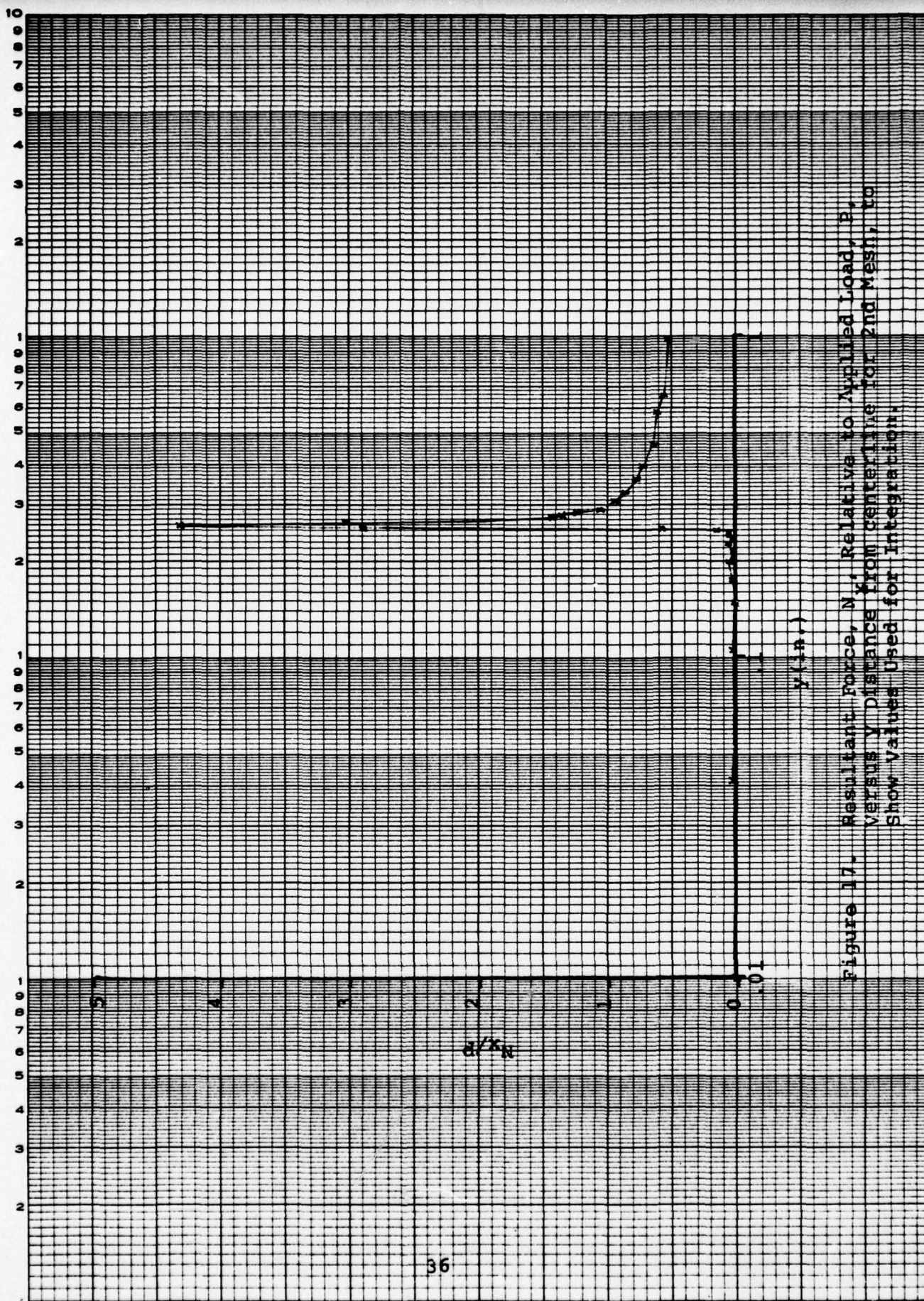


Figure 17. Resultant Force,  $N$ , Relative to Applied Load,  $P$ , Versus  $y$  Distance from centerline for 2nd Mesh, to Show Values Used for Integration.

the  $N_y$  values should integrate to zero and the values of  $N_x$  should integrate to the applied load,  $P$ . The closeness of these integration values to the expected values is a measure of the accuracy of the numerical solution. The relative values of  $N_y/P$  integrate to  $-.009$ , and the relative values of  $N_x/P$  integrate to  $.955$ . These results indicate that for the given assumptions the numerical results are slightly lower than the actual stresses and that no gross numerical inaccuracies are introduced.

A second convergence problem is the determination of the proper loading increments. In the progressive failure model, the load displacement diagram becomes nonlinear, Fig. 18. In the nonlinear portion of the curve, it is necessary to reduce the size of the loading increments in order to insure convergence to the correct solution. In this analysis, the load increment is halved when the modelled displacement in a load iteration is 10% greater than the displacement determined in the previous iteration. The process of reducing the increment is continued until convergence is obtained over all loads or the slope of the load displacement diagram changes by more than a factor of fifty.

The last question which needs to be addressed in the finite element modelling is how to use the stresses which result from the analysis. Since constant strain triangles are used, the stress is assumed to be constant over the entire triangle. For the purpose of analyzing the stress fields, it is assumed that the stress results are for the centroid of the triangle. As



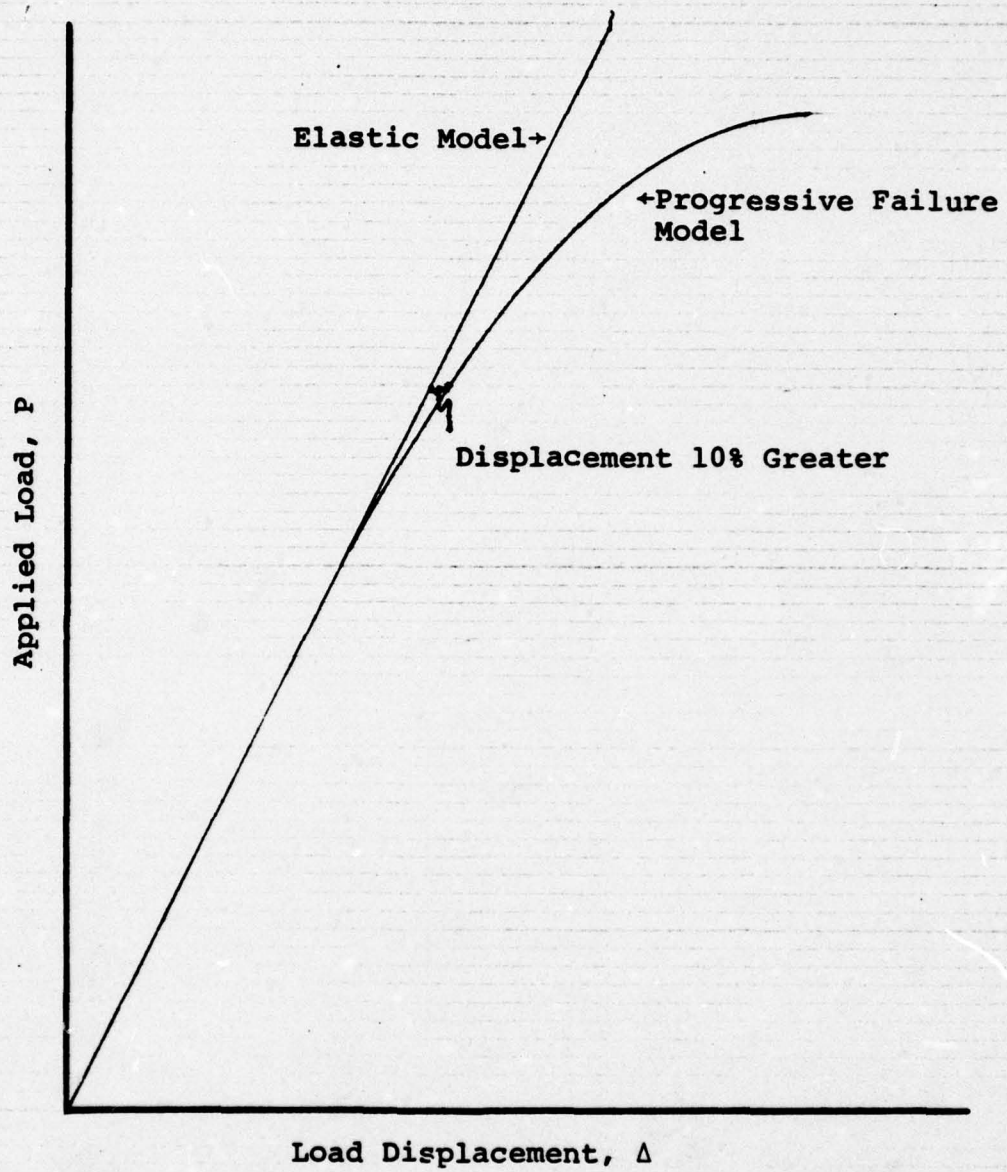


Figure 18. Sample Load Displacement Curve

suggested in reference [32], values of stresses are averaged over adjoining elements using the relative volume of the elements as a weighting factor. This process reduces the variance which exists where there are high stress gradients.

#### Bounding the Damage Zone.

As part of the results from the finite element analysis, the value of the Tsai-Hill failure criterion for each ply in an element is calculated. Since the damage zone boundary is the locus of points where the value of the failure criterion is equal to one, it is necessary to interpolate between calculated values to obtain the location of the damage zone boundary.

The interpolation is performed in the following manner. The plate is divided into fifteen degree segments, where the crack tip is the origin of the fifteen degree radial lines. The radii of the points along these lines where the values of the failure criterion are immediately above and below one are determined. Since the distances between these points is small and the failure criterion varies in a monotonic fashion along the radials, the location of the boundary is determined by linearly interpolating between the points immediately above and below.

#### General Procedure

There are two general procedures which are followed in the numerical analysis stage. One is for the purely elastic method, and the other is for the method which employs ply removal. In the



elastic method, loads are applied in increments of 10% up to the experimentally determined strength. At each level of loading the bounds of the damage zone are determined, but the element stiffnesses are not changed. In the method using ply removal, the same general procedure is initially followed, but after each increment of loading the element plies which failed are removed before the next increment of load is applied. If the displacement differs by more than 10% for the same load increment, the load increment is halved until the model converges. This procedure is continued until either the experimentally determined strength is reached or the model becomes unstable, where instability is defined by the point where the slope changes by more than a factor of fifty.

#### IV. Results

In this section, the results of the analysis will be presented. First, the general load displacement and damage zone determination are discussed followed by the correlation between ply subcrack length and  $K_I^2$  and  $\eta$ . The last section pertains to fracture strength prediction.

##### General Results

The load-displacement data for the elastic and progressive failure models are given in Table III. The load displacement curve for the elastic model is shown in Fig. 19. The relationship between the load and the displacement remains linear.

The load displacement curves for the progressive failure model are shown in Fig. 20. Four iterations were required before the model converged. The first iteration diverged from the elastic curve by more than 10% at 90% of the experimental fracture strength; this loading sequence was continued, though, until an instability was reached at 110% of the fracture strength. The next iteration started at 85% of the fracture strength and proceeded in 5% increments. This iteration diverged at the 90% level again and developed an instability at 100% of fracture strength. During the third iteration, divergence occurred at 90% and instability at 92.5%. The last iteration started at 87.5%, and developed an instability at 90%.



Table III

## Load Displacement Curve Data

Per Cent of Experimental Fracture Load	Applied Load (lb.)	Applied Stress (ksi)	Load Displacement (in.)
Elastic Model			
10	256	2.98	$2.1600 \times 10^{-3}$
20	504	5.88	$4.2500 \times 10^{-3}$
30	760	8.86	$6.4117 \times 10^{-3}$
40	1016	11.84	$8.4300 \times 10^{-3}$
50	1264	14.73	$1.0664 \times 10^{-2}$
60	1520	17.72	$1.2823 \times 10^{-2}$
70	1768	20.61	$1.4916 \times 10^{-2}$
80	2024	23.59	$1.7075 \times 10^{-2}$
90	2280	26.58	$1.9235 \times 10^{-2}$
100	2528	29.47	$2.1327 \times 10^{-2}$
Progressive Failure Model, 1st Iteration			
10	256	2.98	$2.1588 \times 10^{-3}$
20	504	5.88	$4.2503 \times 10^{-3}$
30	760	8.86	$6.4120 \times 10^{-3}$
40	1016	11.84	$8.5866 \times 10^{-3}$
50	1264	14.73	$1.0705 \times 10^{-2}$
60	1520	17.72	$1.2947 \times 10^{-2}$
70	1768	20.61	$1.5197 \times 10^{-2}$
80	2024	23.59	$1.7807 \times 10^{-2}$
90	2280	26.58	$2.1533 \times 10^{-2}$
100	2528	29.47	$3.2329 \times 10^{-2}$
110	2784	32.45	1.2248
Progressive Failure Model, 2nd Iteration			
85	2152	25.09	$2.0324 \times 10^{-2}$
90	2280	26.58	$2.4415 \times 10^{-2}$
95	2408	28.07	$3.2135 \times 10^{-2}$
100	2528	29.47	1.2352
Progressive Failure Model, 3rd Iteration			
87.5	2216	25.83	$2.3730 \times 10^{-2}$
90	2280	26.58	$3.0427 \times 10^{-2}$
92.5	2344	27.37	1.1400
Progressive Failure Model, 4th Iteration			
88.75	2248	26.20	$3.0000 \times 10^{-2}$
90	2280	26.58	1.1000

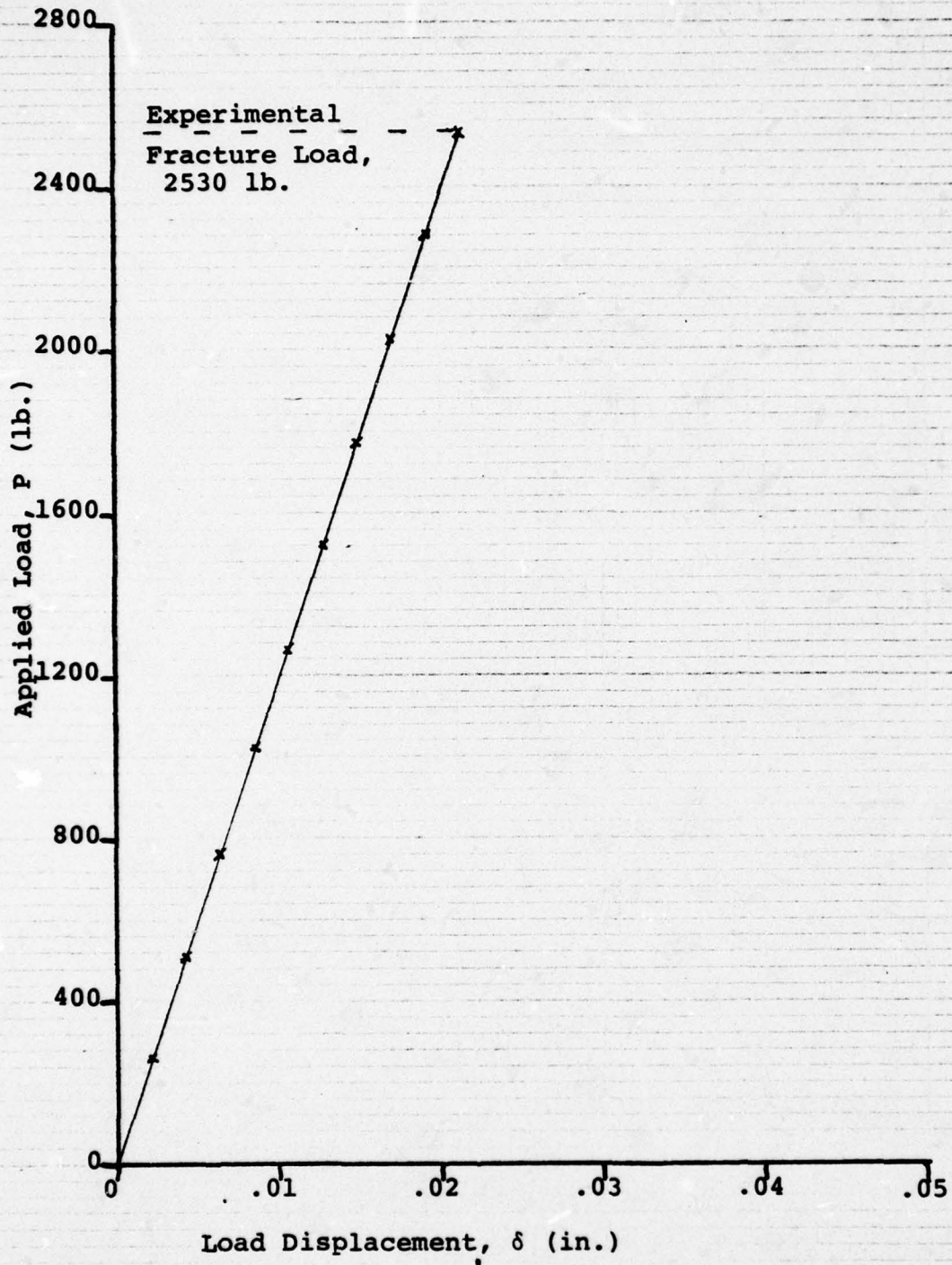


Figure 19. Load Versus Displacement Curve for Elastic Model.



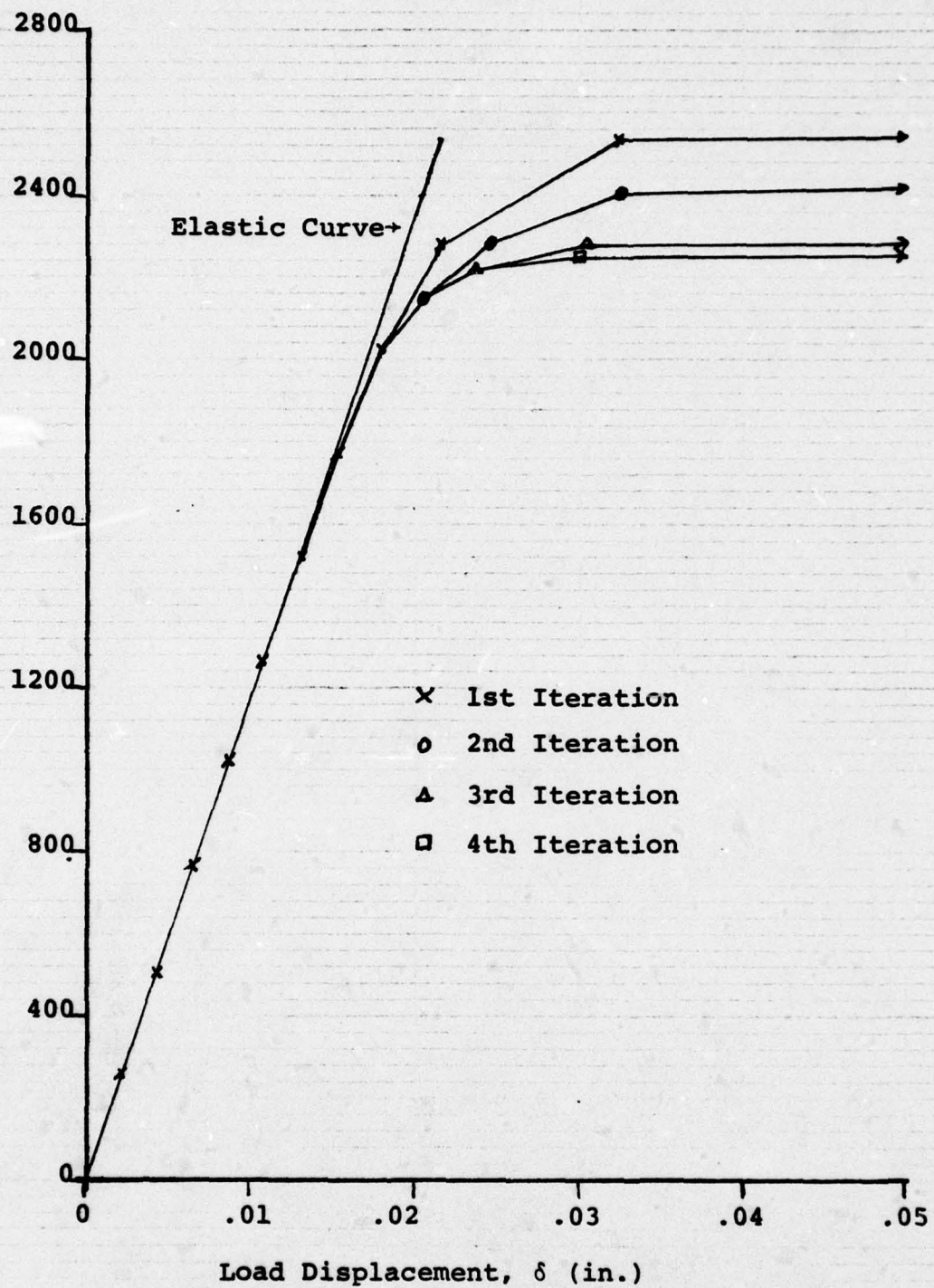


Figure 20. Load Versus Displacement Curve for Progressive Failure Model.

The damage zone diagrams for the elastic model are shown in Figures 21-30. The plots correspond to the portion of the plate shown in the figures. The coordinates  $x$  and  $y$  are normalized by dividing them by the plate width,  $w$ . The dotted line parallel to the  $y$ -axis represents the crack and the crack tip is located at  $y/w = .13$ . The boundary of the plate is at  $y/w = .5$ .

Several generalizations can be drawn from examination of these plots. First the damage zone remains very small until 40% of the fracture strength is reached. From Fig. 28, which is for 80% of the fracture strength, the general shape of the damage zones in each ply can be seen.

The damage zone in each ply generally extends the farthest in a direction perpendicular to the fiber direction. This is caused by the large amount of shearing and transverse failure. The damage zone extends slightly behind the crack tip in all plies.

The  $90^\circ$  ply has the largest damage zone, and the zone in this ply grows the fastest. At 100% of the fracture load, all of the  $90^\circ$  ply has failed except for a small area along the crack flanks.

The boundaries for the  $+45^\circ$  ply and the  $-45^\circ$  ply essentially coincide. The small deviances which occur are believed to be caused by numerical errors. As previously mentioned, the stress fields in the  $\pm 45^\circ$  plies showed the greatest disparity among adjoining elements. The damage zone in the  $\pm 45^\circ$  plies remains essentially circular in nature.



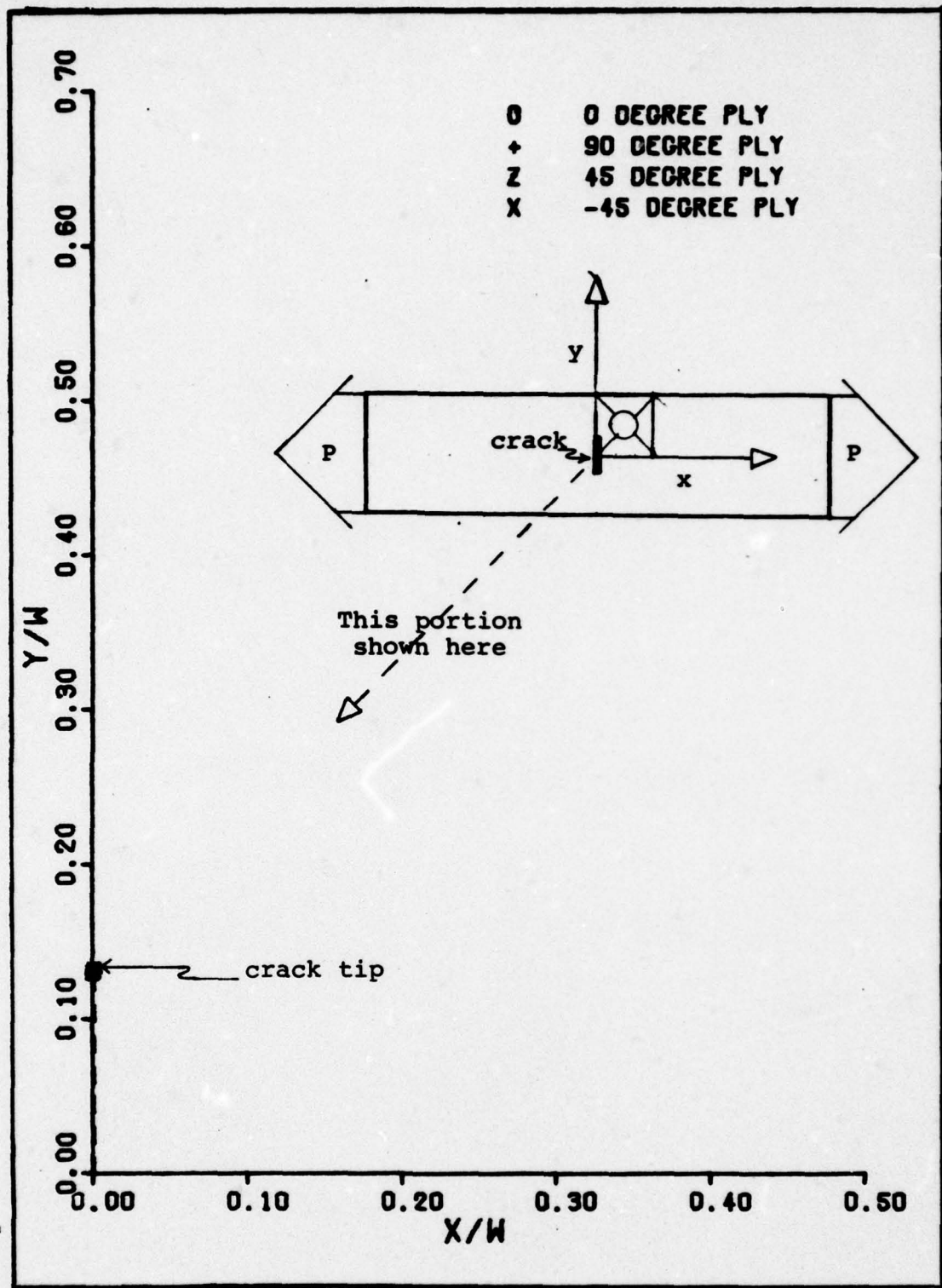


Figure 21. Damage Zone Prediction at 10% of Experimental Fracture Load, Using Elastic Model.

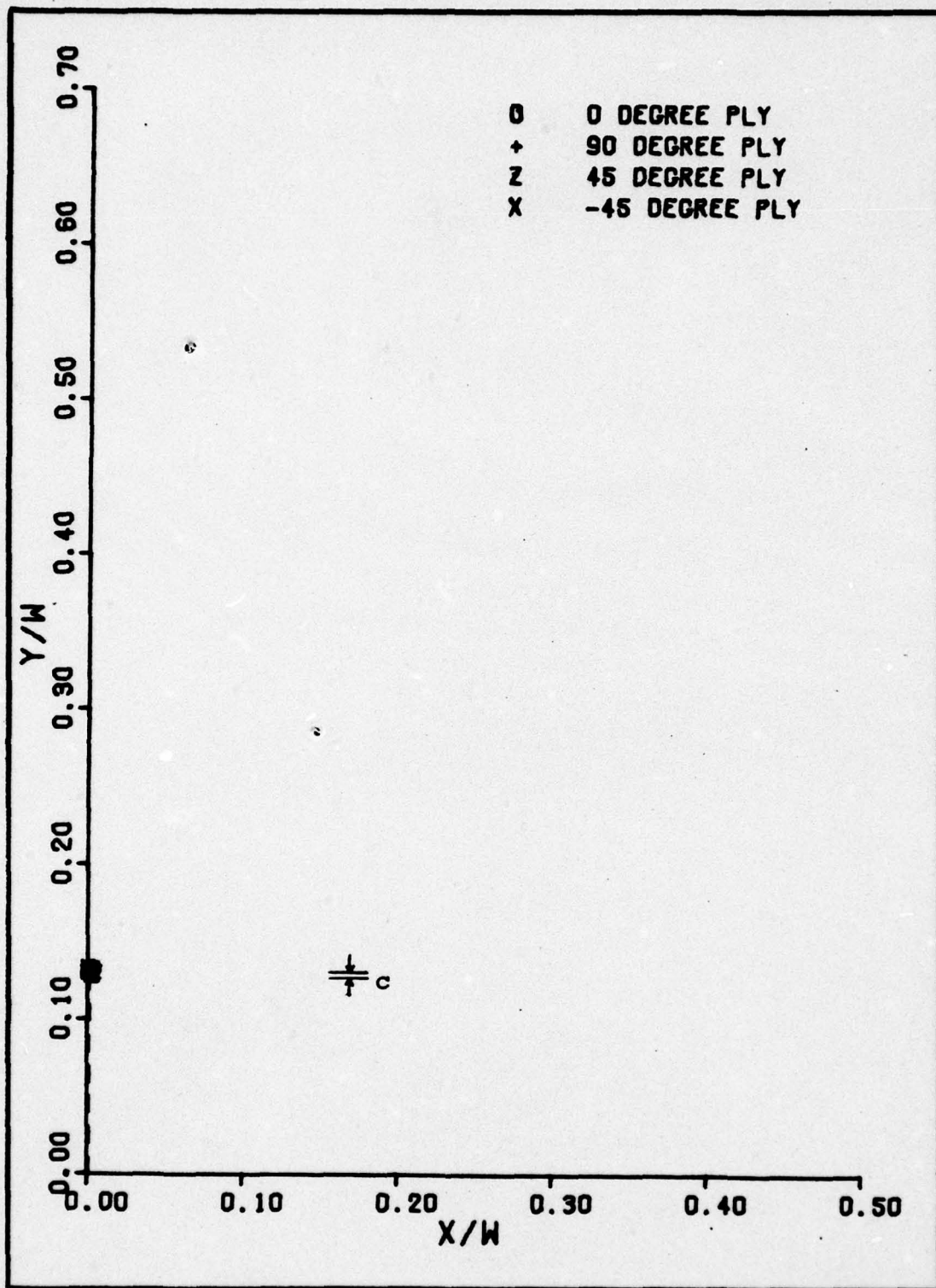


Figure 22. Damage Zone Prediction at 20% of Experimental Fracture Load, Using Elastic Model.



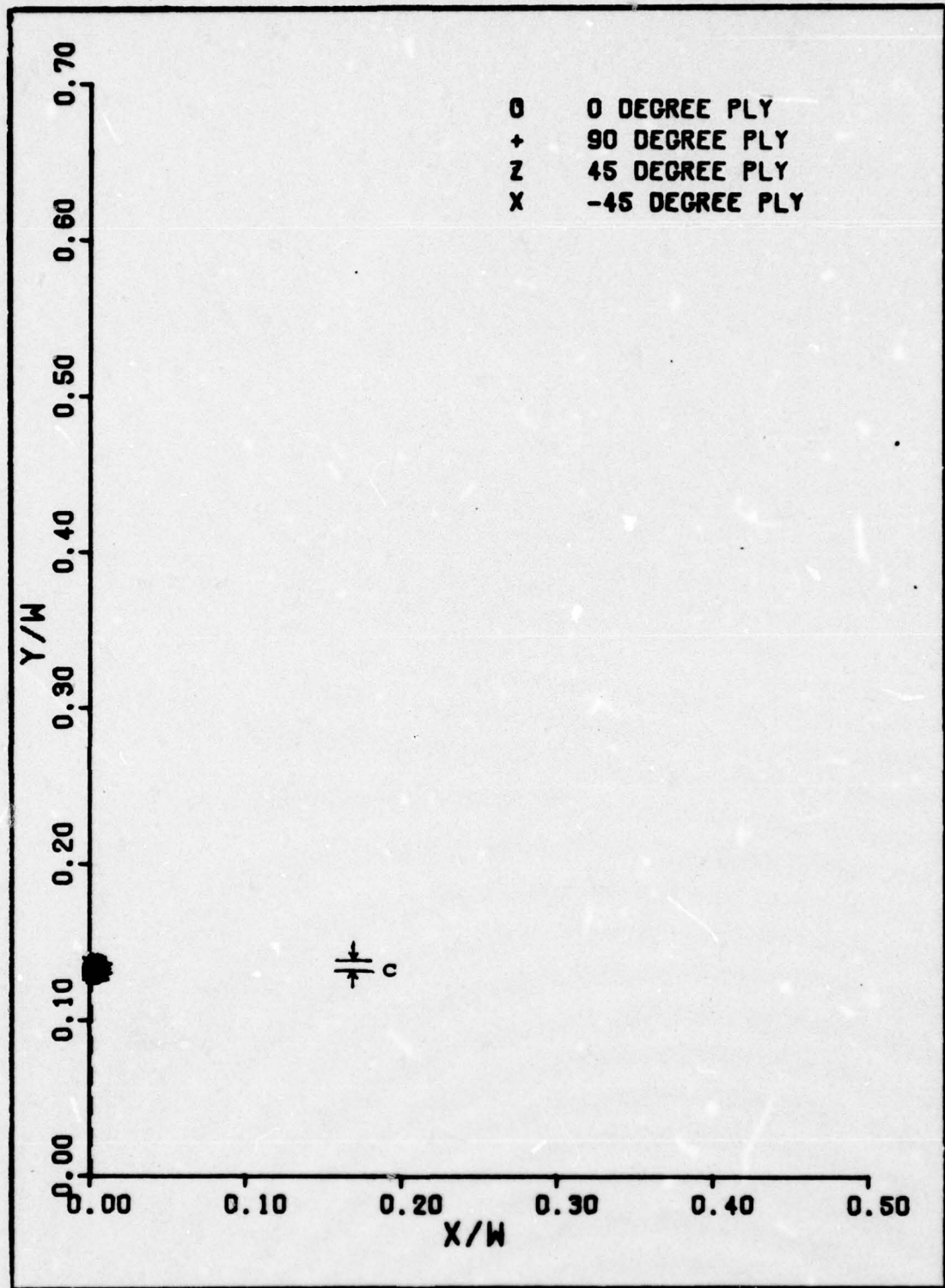


Figure 23. Damage Zone Prediction at 30% of Experimental Fracture Load, Using Elastic Model.

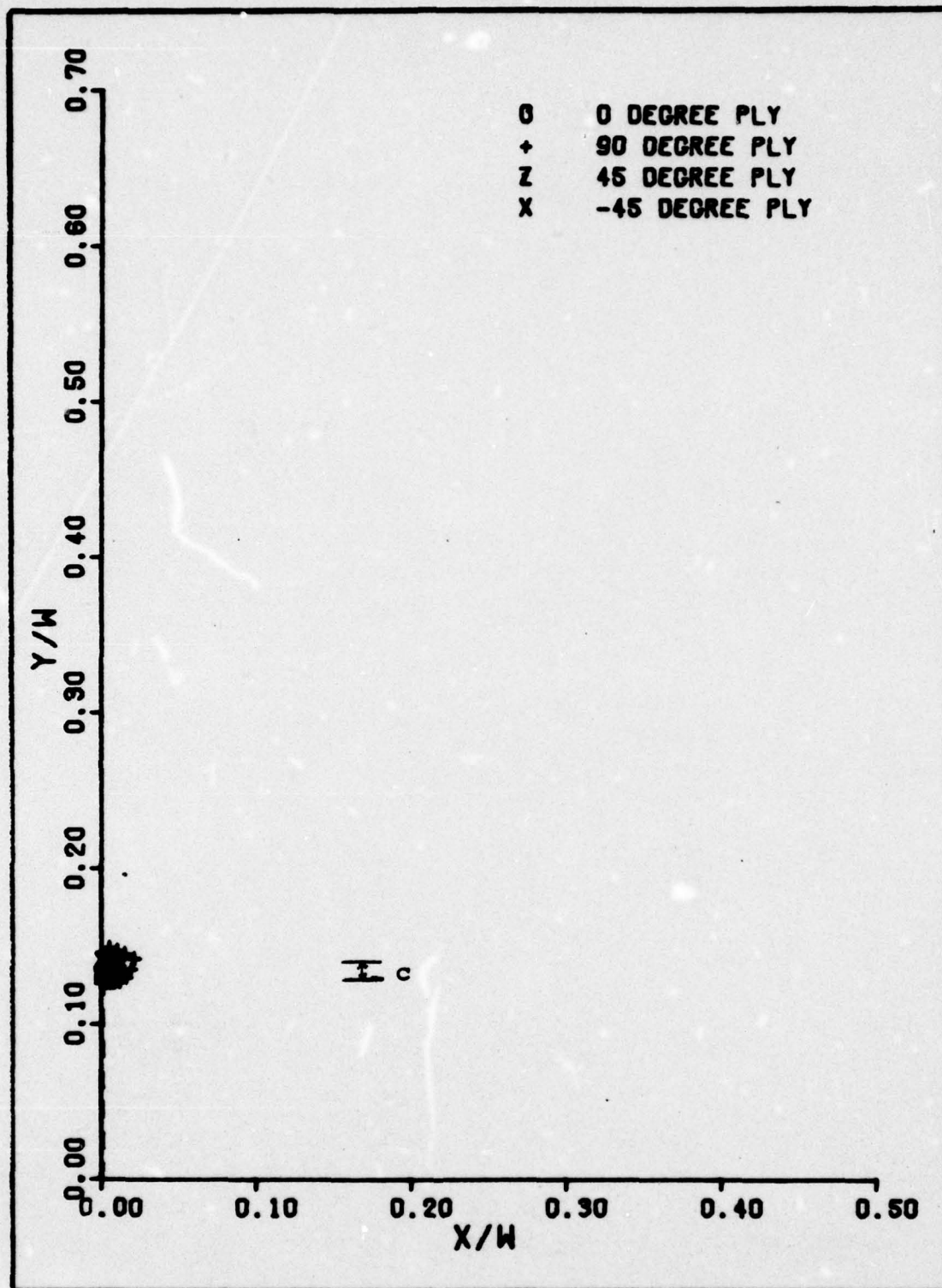


Figure 24. Damage Zone Prediction at 40% of Experimental Fracture Load, Using Elastic Model.



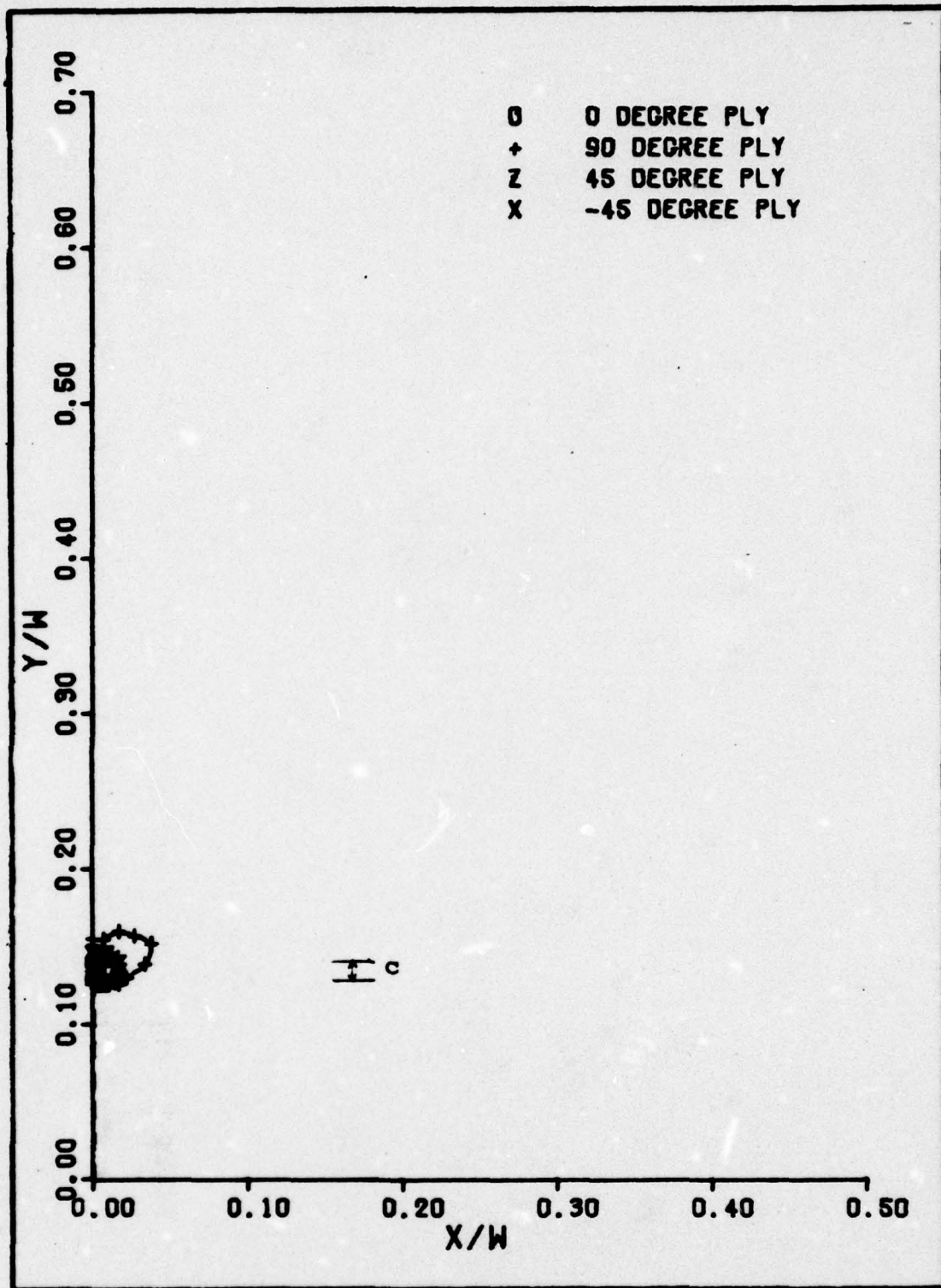


Figure 25. Damage Zone Prediction at 50% of Experimental Fracture Load, Using Elastic Model.

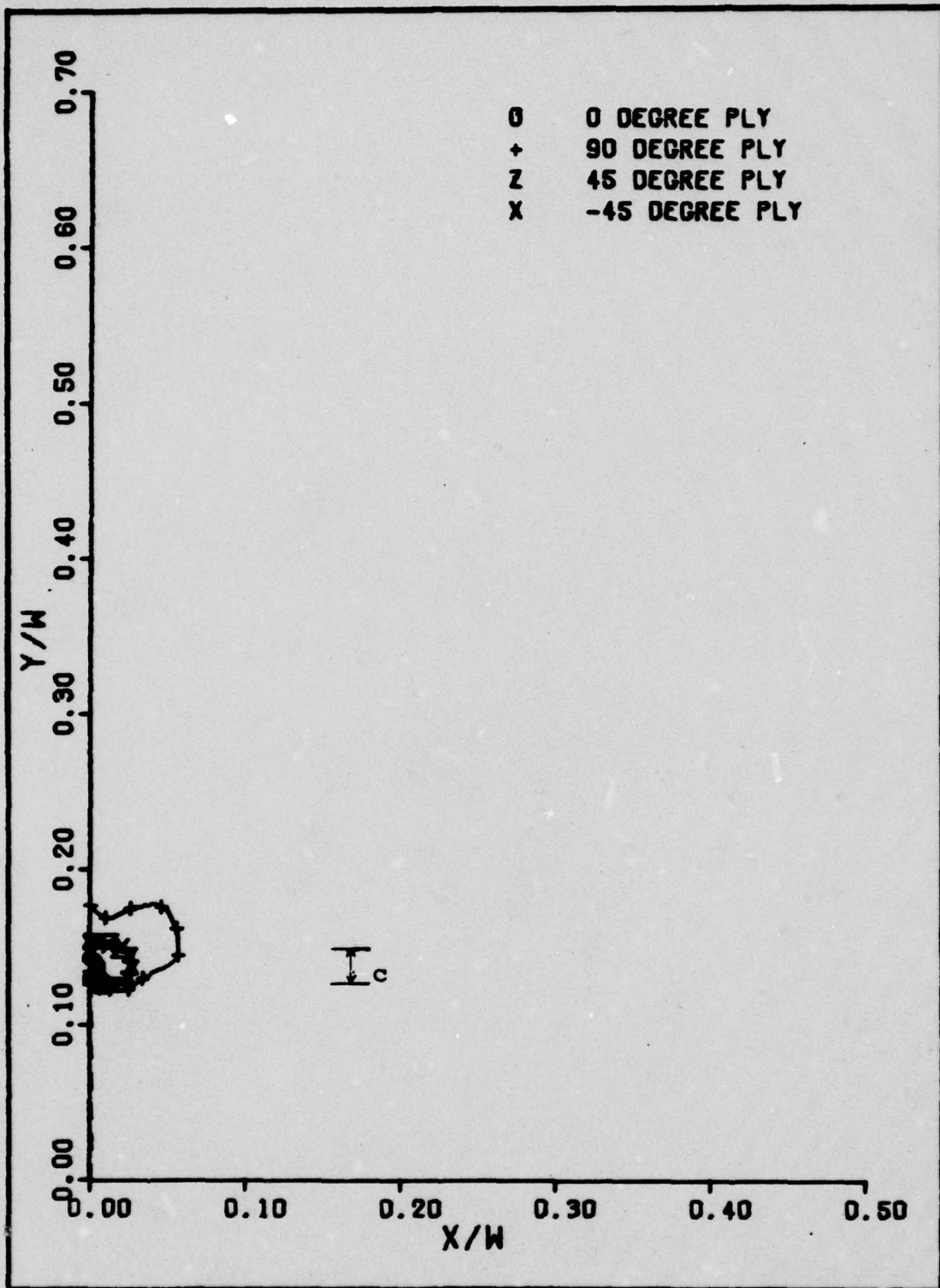


Figure 26. Damage Zone Prediction at 60% of Experimental Fracture Load, Using Elastic Model.



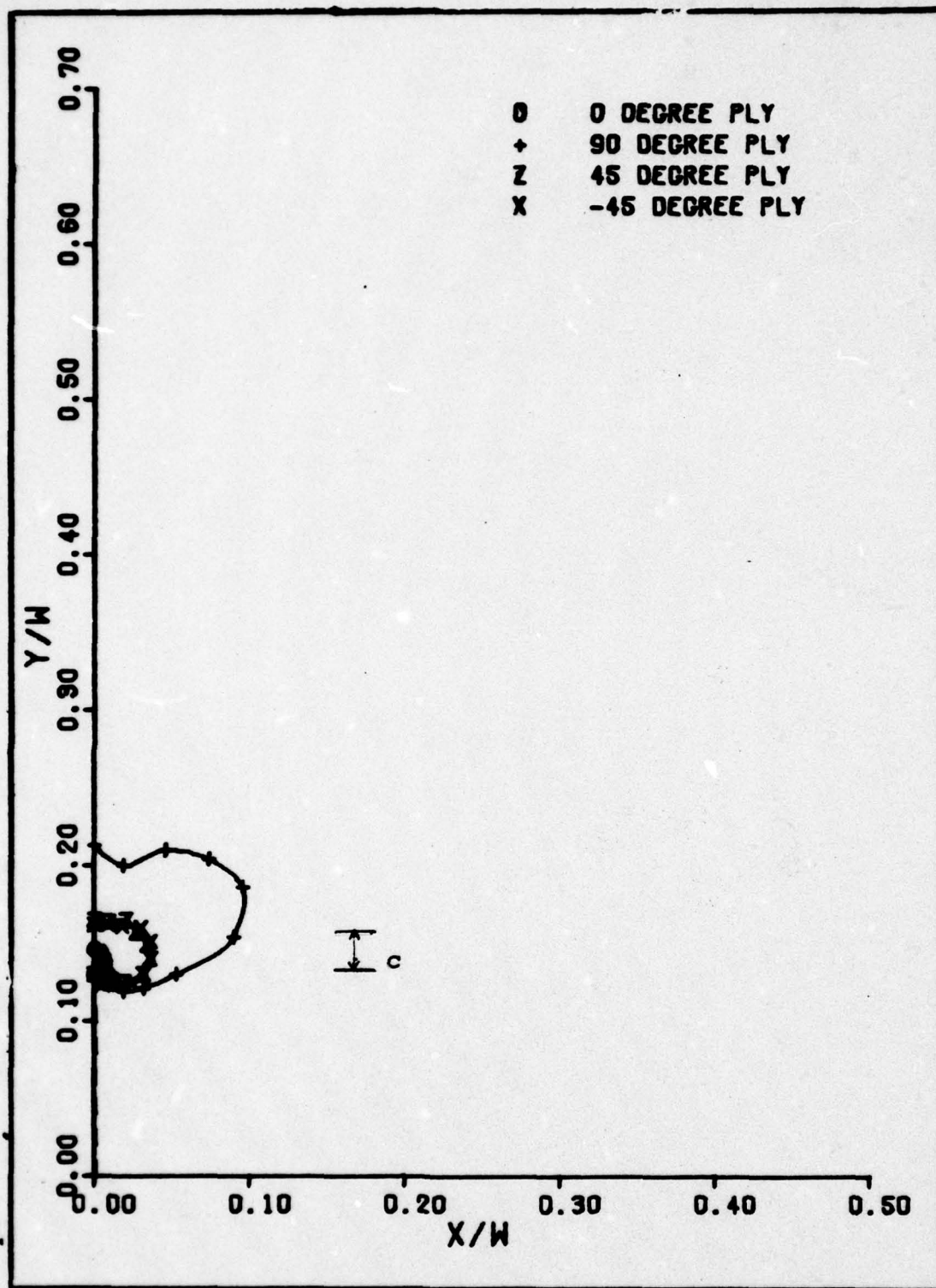


Figure 27. Damage Zone Prediction at 70% of Experimental Fracture Load, Using Elastic Model.

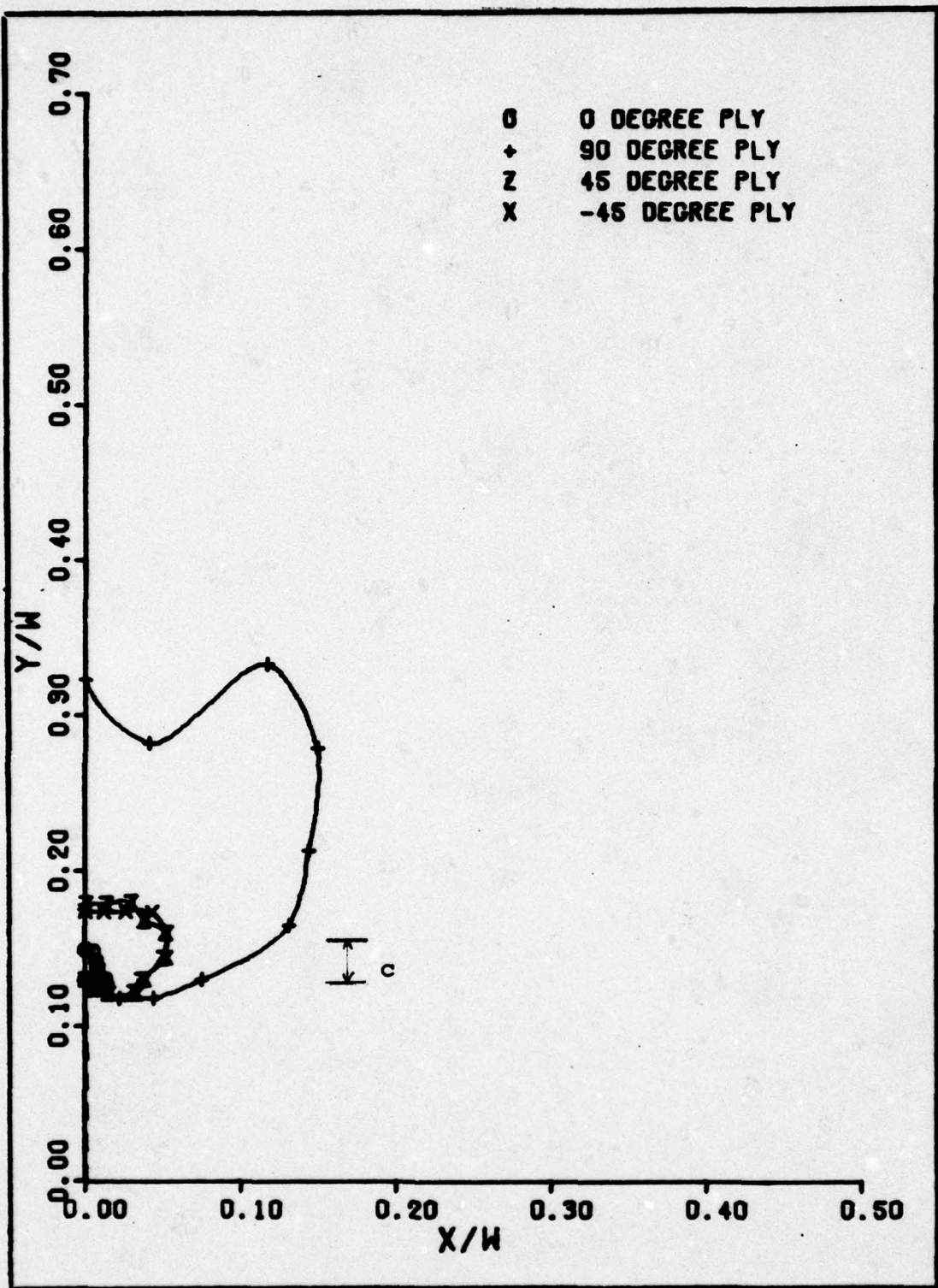


Figure 28. Damage Zone Prediction at 80% of Experimental Fracture Load, Using Elastic Model.



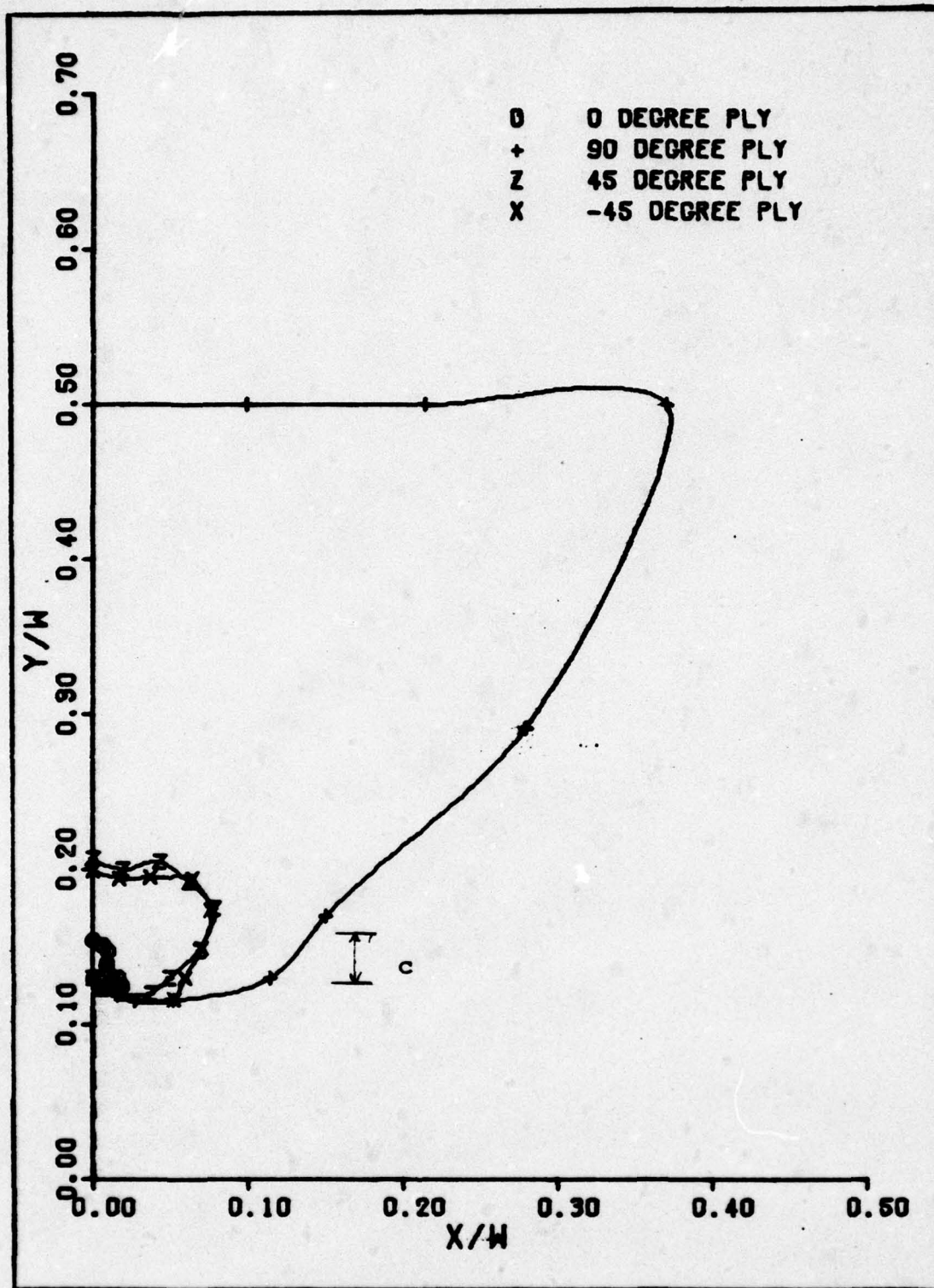


Figure 29. Damage Zone Prediction at 90% of Experimental Fracture Load, Using Elastic Model.

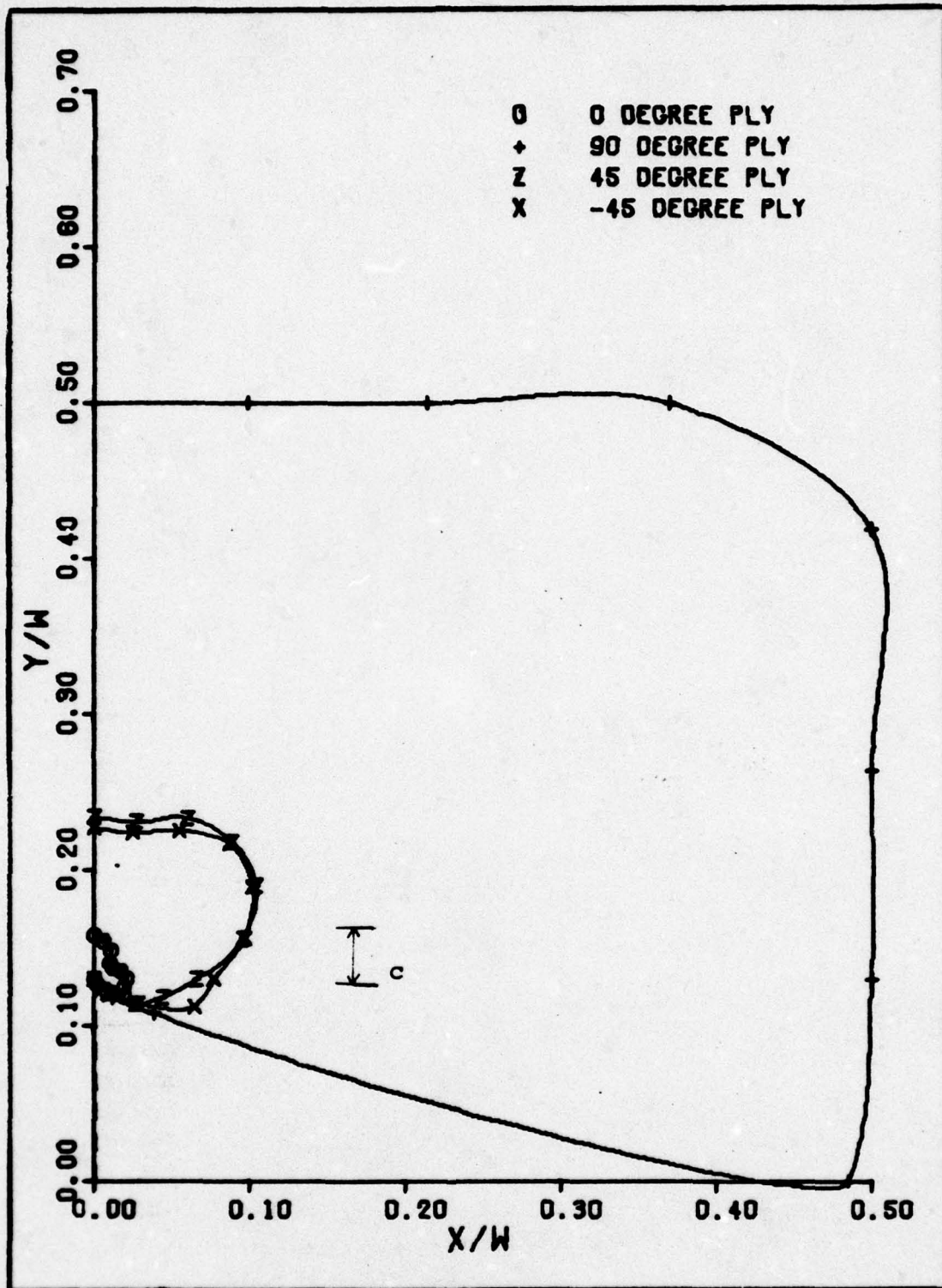


Figure 30. Damage Zone Prediction at 100% of Experimental Fracture Load, Using Elastic Model.



The smallest damage zone is that for the  $0^\circ$  plies. As can be seen, it is narrow and pointed. The area bounded by the  $0^\circ$  damage zone is also the area in which all plies have failed. The growth of this damage zone is mainly in the direction of the original notch. Due to the shape and extension direction of this damage zone, the assumption that it represents pseudo-crack extension is validated.

The damage zone boundaries for the progressive failure model are shown in Figures 31 through 40. The boundaries for the elastic model and the progressive failure model are similar up to the 50% load level. At this point, the damage zones in the progressive failure model begin to grow faster. Another dissimilarity is that the growth of the damage zone behind the crack tip stops at 50%. The removal of element plies causes enough stress relaxation so that the stresses in this area are similar to the stresses along the crack flanks.

At the 85% load level, the  $\pm 45^\circ$  plies and the  $90^\circ$  ply have failed in the entire region between the crack tip and the edge of the plate. Contrary to what happens with the elastic model, the  $90^\circ$  ply never fails over the entire plate. Ultimate failure becomes imminent when  $0^\circ$  ply damage zone reaches the edge of the plate at 88.75% of the experimental fracture strength.

Several observations can be made by comparing the elastic model and the progressive failure damage zones. First, in the progressive failure model, the stress relaxation caused by element ply removal causes the area where the stresses are relatively small to expand from the immediate vicinity of the

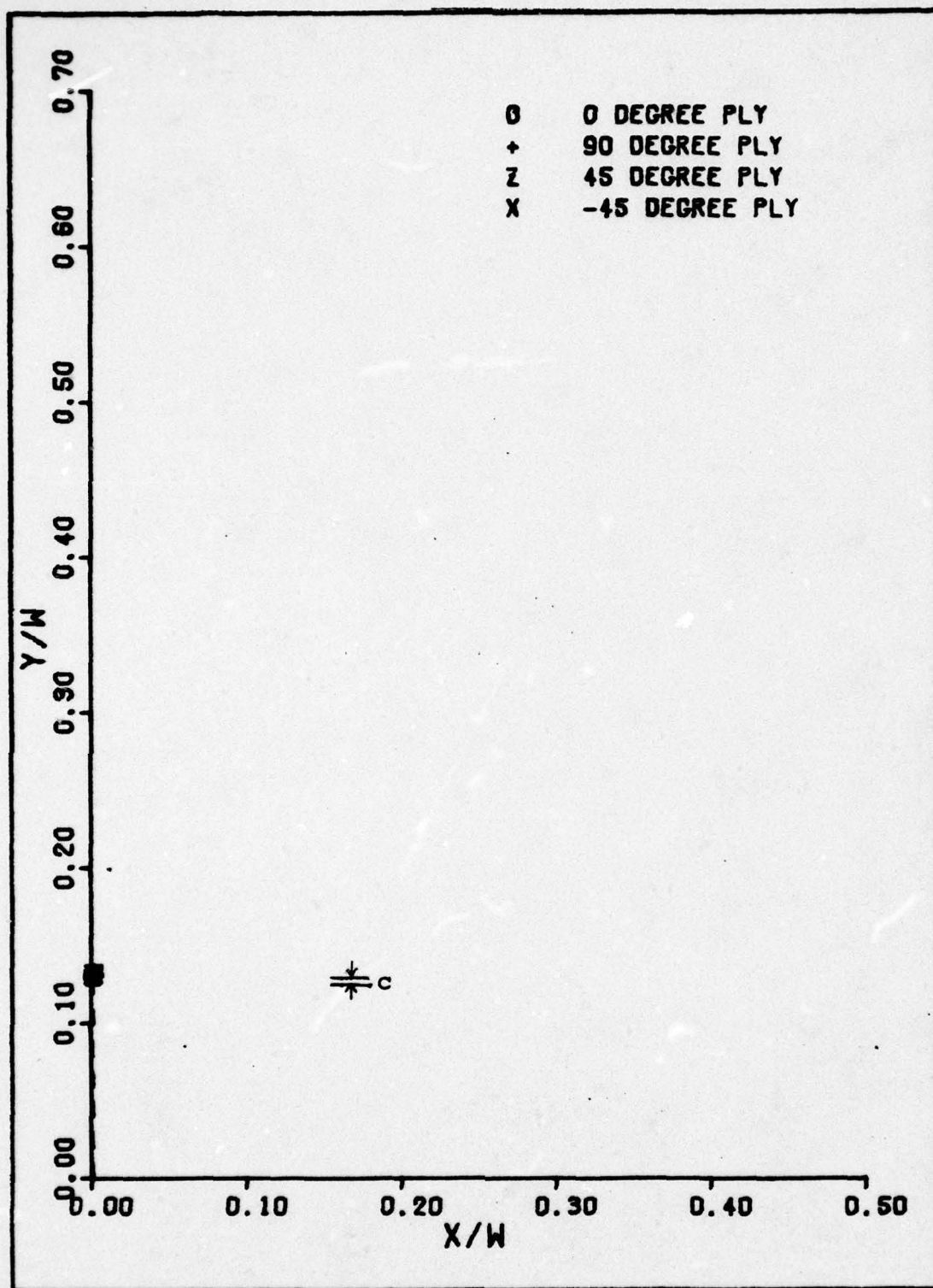


Figure 31. Damage Zone Prediction at 20% of Experimental Fracture Load, Using Progressive Failure Model.



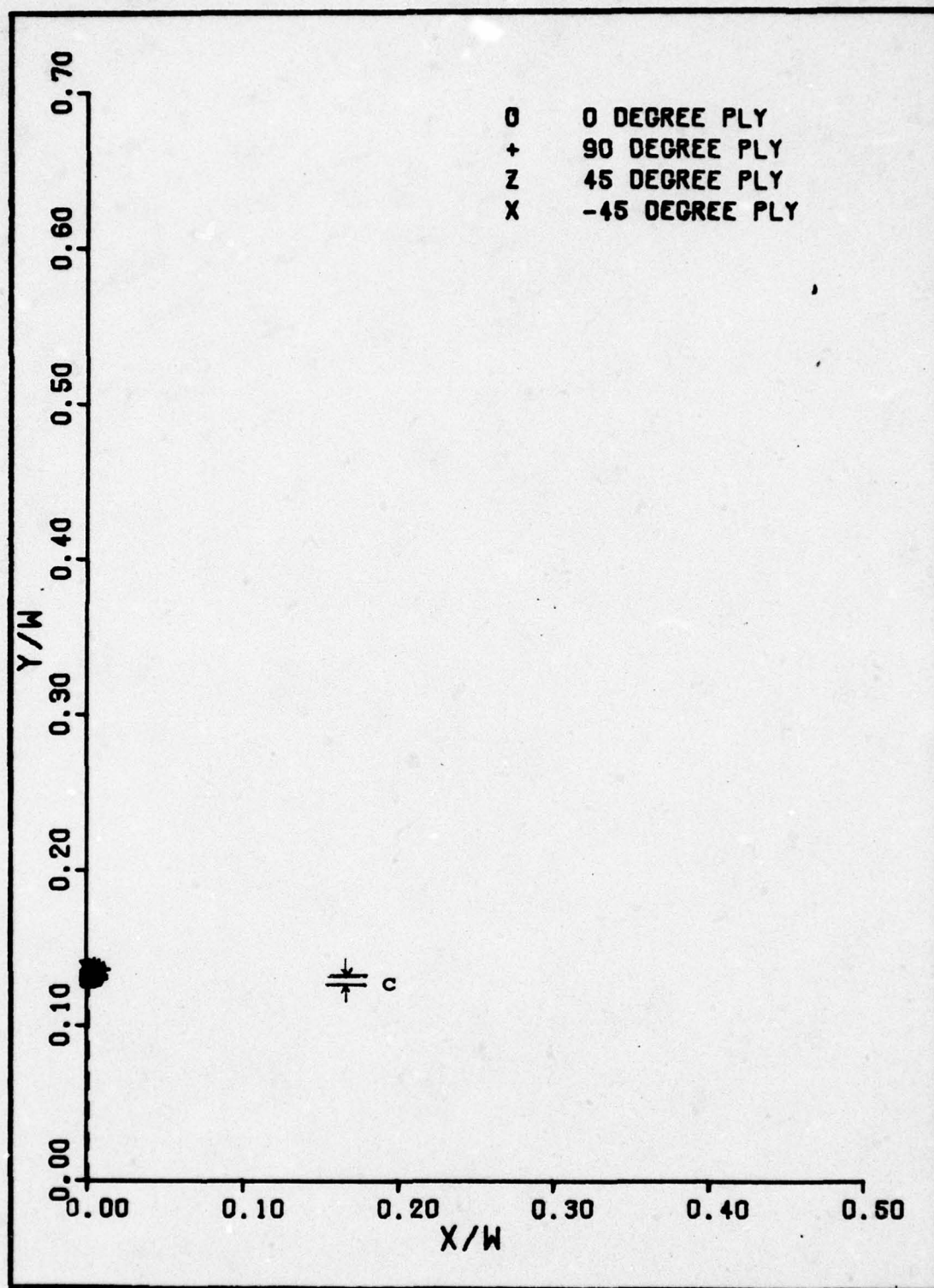


Figure 32. Damage Zone Prediction at 30% of Experimental Fracture Load, Using Progressive Failure Model.

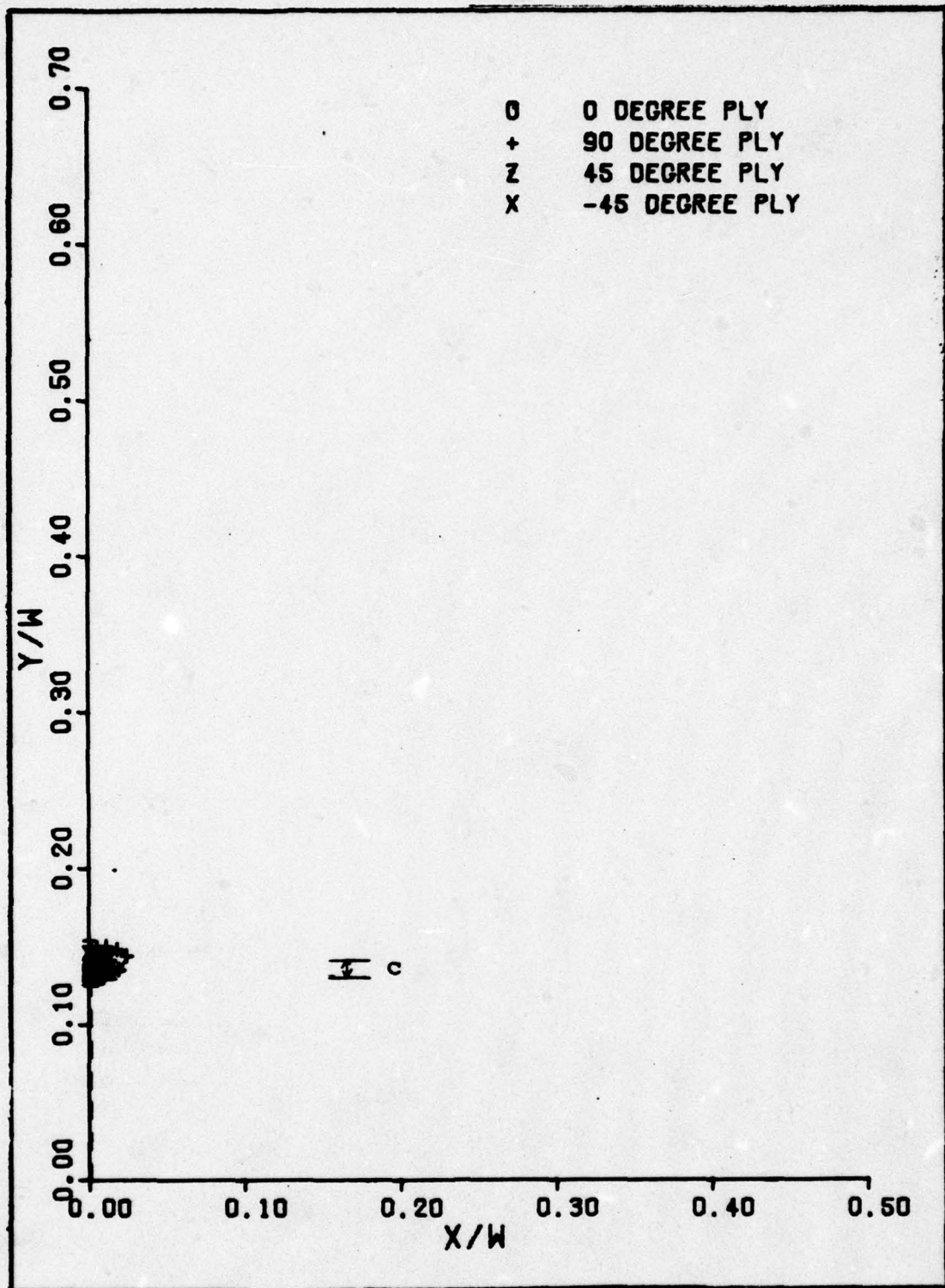


Figure 33. Damage Zone Prediction at 40% of Experimental Fracture Load, Using Progressive Failure Model.



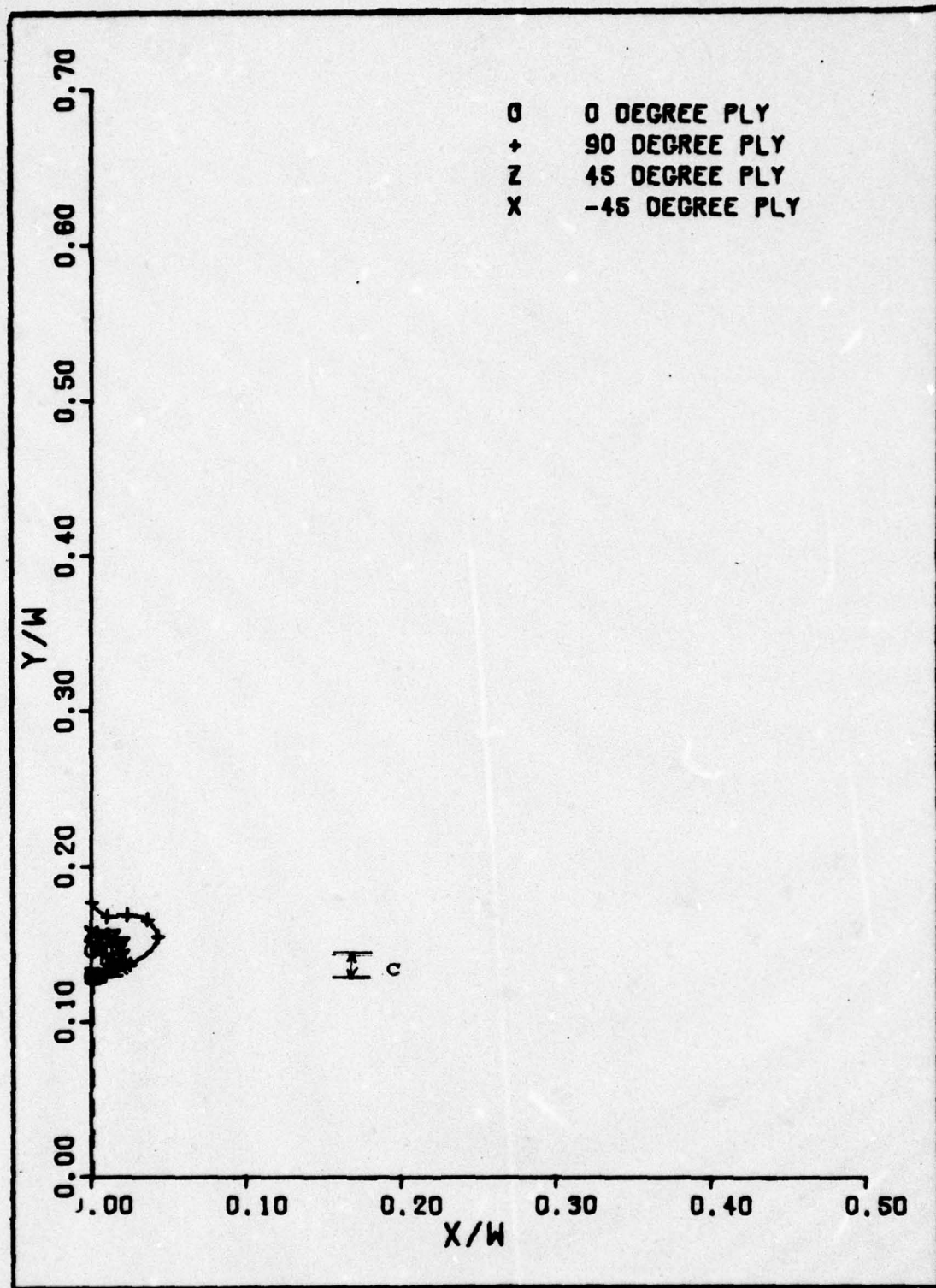


Figure 34. Damage Zone Prediction at 50% of Experimental Fracture Load, Using Progressive Failure Model.

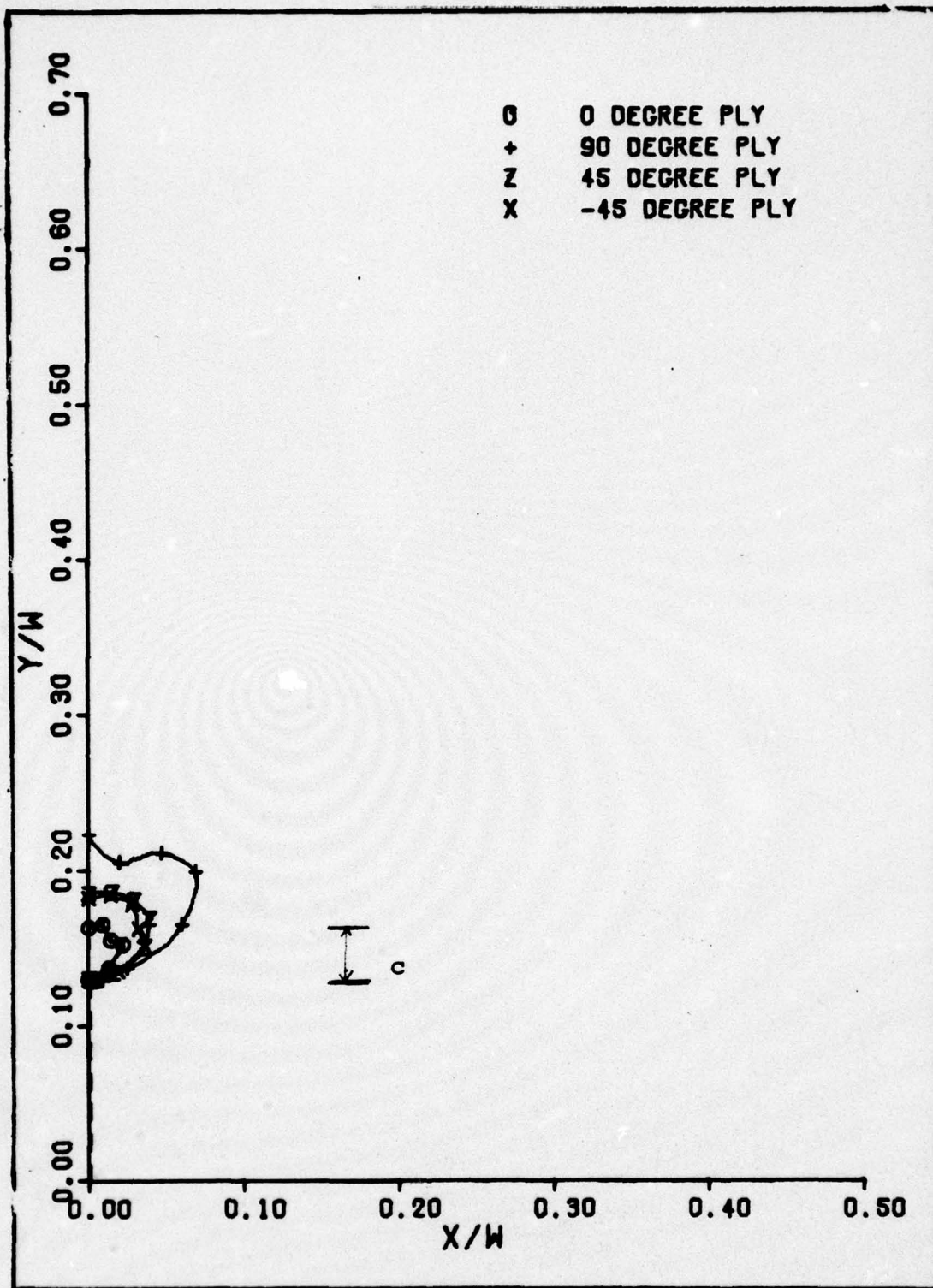


Figure 35. Damage Zone Prediction at 60% of Experimental Fracture Load, Using Progressive Failure Model.



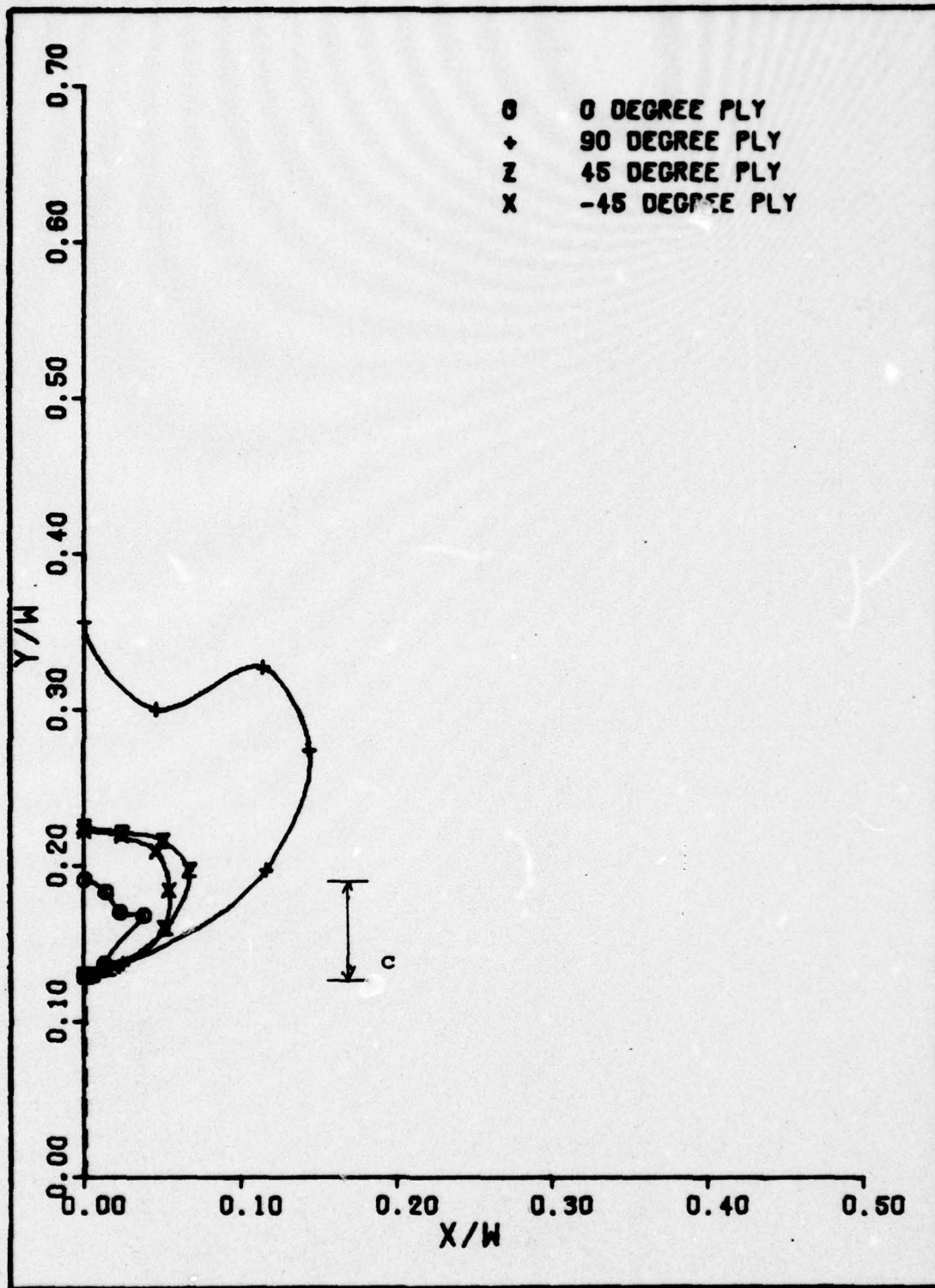


Figure 36. Damage Zone Prediction at 70% of Experimental Fracture Load, Using Progressive Failure Model.

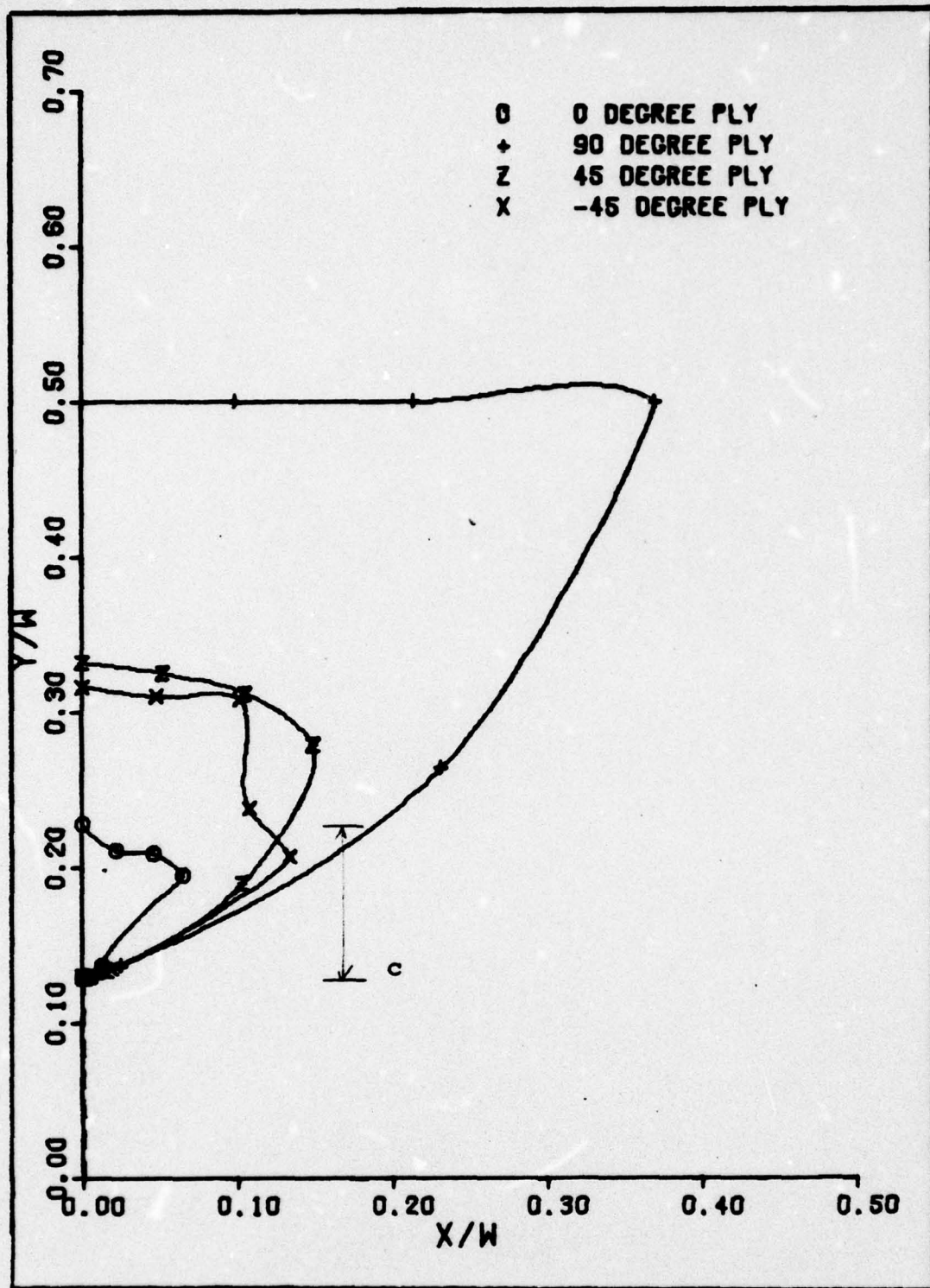


Figure 37. Damage Zone Prediction at 80% of Experimental Fracture Load, Using Progressive Failure Model.



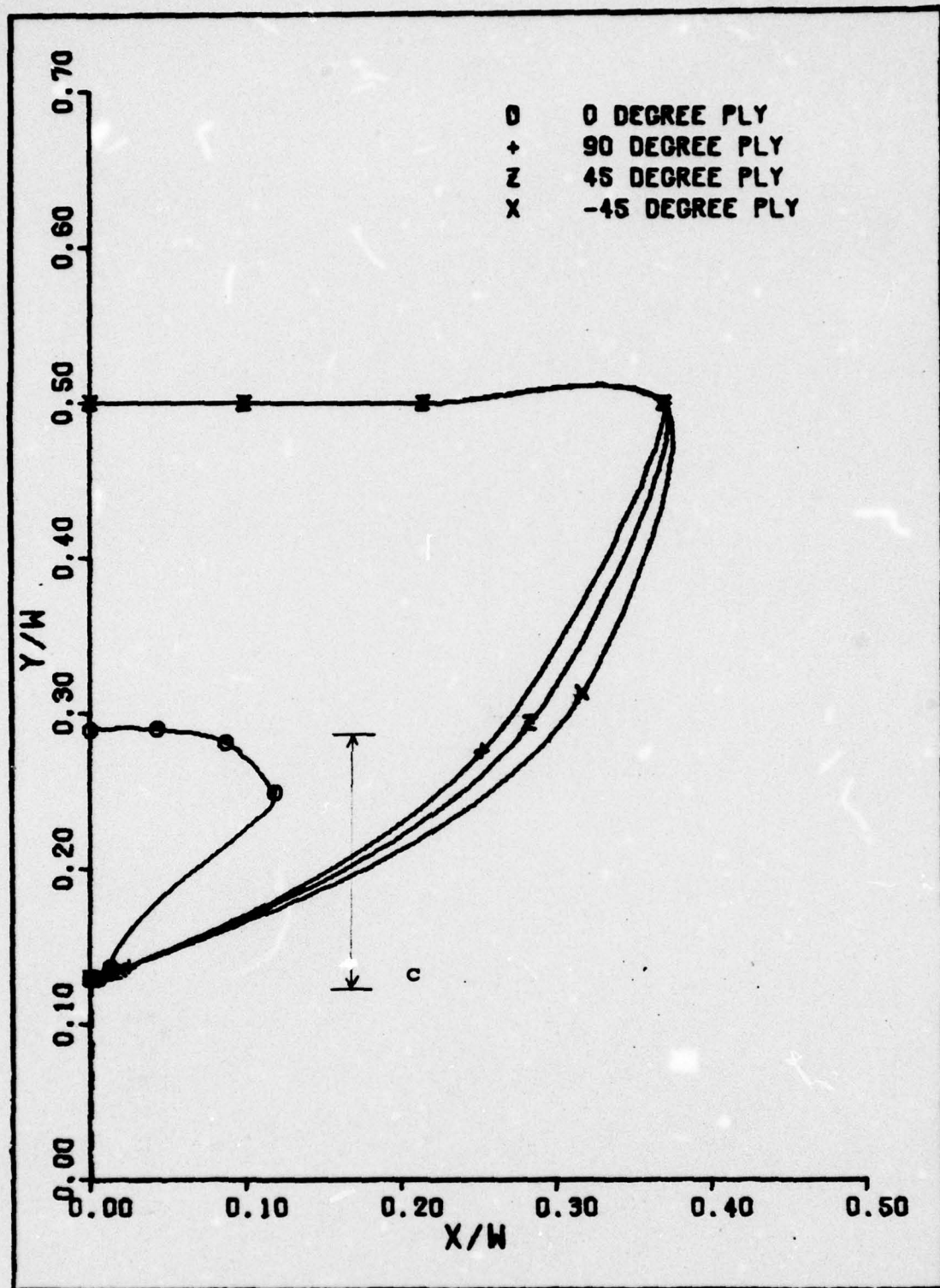


Figure 38. Damage Zone Prediction at 85% of Experimental Fracture Load, Using Progressive Failure Model.

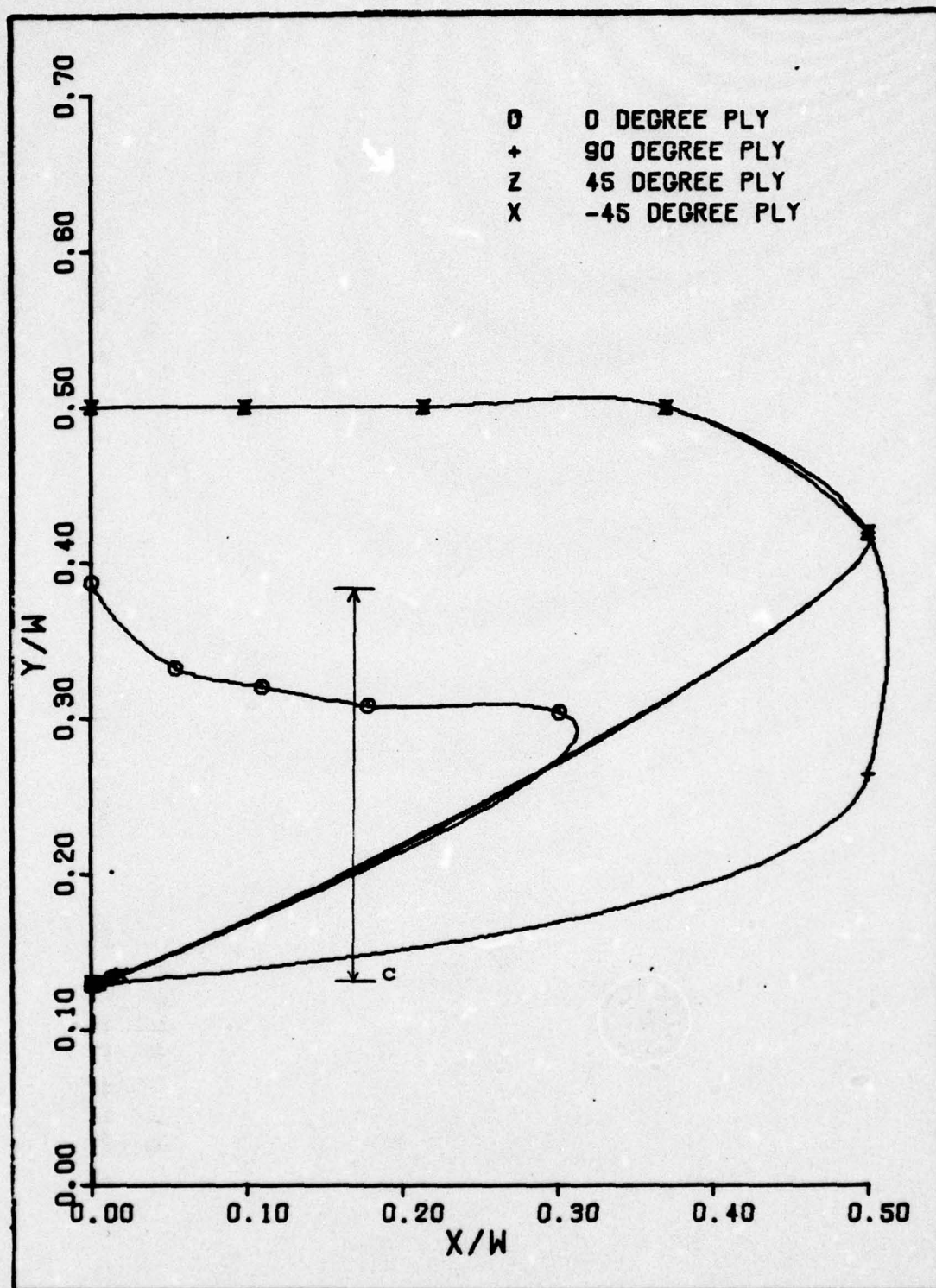


Figure 39. Damage Zone Prediction at 87.5% of Experimental Fracture Load, Using Progressive Failure Model.



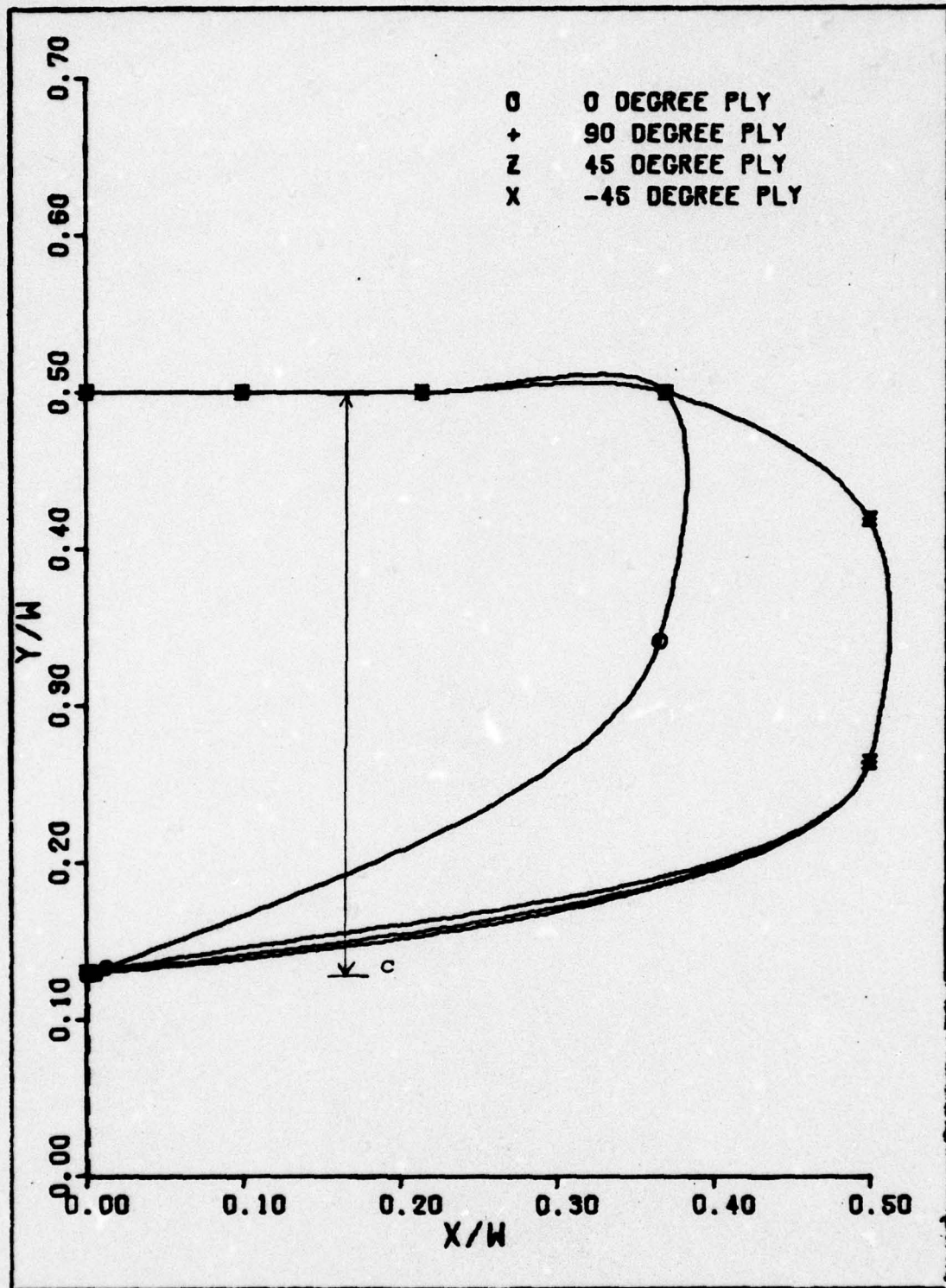


Figure 40. Damage Zone Prediction at 88.75% of Experimental Fracture, Load, Using Progressive Fracture Model.

crack flanks, which is where the relatively small stresses occur in the elastic model. Next, as is obvious by comparing respective damage zone diagrams, the damage zones predicted using the progressive failure model are larger than those predicted using the elastic model. As a consequence of this larger size, the predicted failure load is less for the progressive failure model than it is for the elastic model. Last, it must be recognized that these two models are intended to bound the actual case. The actual damage zone boundaries will exist somewhere between those predicted with the progressive failure model and those predicted with the elastic model.

#### Correlation of Subcrack Length

The first application of the finite element analysis is to check the correlation between the subcrack length in each ply and the values of  $K_I^2$  and  $\chi$ . Two values of  $K_I$  are calculated; one is for the purely elastic analysis, and the other is for the progressive failure analysis.

The first task is to determine the length of the subcracks in each ply. The subcrack measurements are obtained from the photographs shown in Figures 4 through 9. As can be seen in these photographs the exact length of the ply subcracks is not easily discernible. The subcracks perpendicular to the notch are in the  $0^\circ$  ply; the subcracks colinear with the notch are in the  $90^\circ$  ply, and the subcracks running oblique to the notch are in the  $\pm 45^\circ$  plies. Since the orientation of the plate is



unknown, it is impossible to discern between the +45° and -45° plies. The subcrack lengths shown in Table IV are the average of the measured lengths.

Table IV			
Subcrack Lengths			
Applied Stress (ksi)	0° ply (in.)	90° ply (in.)	+45° ply (in.)
14.734	.031	.047	.023
17.718	.055	.086	.039
20.609	.057	.115	.046
23.593	.060	.226	.068
26.577	.084	.436	.092
28.069	.087	.564	.095

The values of  $K_I$  are obtained from equation (4); and  $\mathcal{J}$  is calculated using equation (8). The crack half length,  $a$ , is calculated using equation (5). The computed values of  $K_I$  at the various stress levels for the elastic analysis are shown in Table V.

The values of  $K_I$  for the progressive failure analysis are shown in Table VI. This table does not go to the same stress level as the elastic analysis since the analysis developed an instability before 100% of the experimental notched strength was reached. The values of  $\mathcal{J}$  are shown in Table VII. The compliance values are obtained from Fig. 20.

The values of  $K_I^2$  determined from the elastic analysis versus the subcrack length in each ply are shown in Fig. 41. As was found in reference 4, there appears to be a linear

Table V				
K <sub>I</sub> Calculations (Elastic Model)				
Applied Stress (ksi)	Crack Length (in.)	Plate Width (in.)	K <sub>I</sub> (ksi-in. <sup>1/2</sup> )	K <sub>I</sub> <sup>2</sup> (ksi <sup>2</sup> -in.)
2.9841	.2559	1.9685	2.75	7.59
5.8750	.2559	1.9685	5.00	25.04
8.8591	.2640	1.9685	8.32	69.24
11.8433	.2687	1.9685	11.04	121.85
14.7341	.2745	1.9685	14.15	200.19
17.7183	.2814	1.9685	17.28	298.44
20.6091	.2865	1.9685	20.28	411.36
23.5933	.2928	1.9685	23.51	552.87
26.5774	.3034	1.9685	27.04	731.34
29.4683	.3116	1.9685	30.46	927.85

Table VI				
K <sub>I</sub> Calculations (Progressive Failure Model)				
Applied Stress (ksi)	Crack Length (in.)	Plate Width (in.)	K <sub>I</sub> (ksi-in. <sup>1/2</sup> )	K <sub>I</sub> <sup>2</sup> (ksi <sup>2</sup> -in.)
2.9841	.2559	1.9685	2.75	7.59
5.8750	.2559	1.9685	5.00	25.04
8.8591	.2615	1.9685	8.28	68.50
11.8433	.2701	1.9685	11.27	126.98
14.7341	.2881	1.9685	14.55	211.62
17.7183	.3213	1.9685	18.65	344.93
20.6091	.3769	1.9685	23.96	573.85
23.5933	.4487	1.9685	30.89	953.51
25.0853	.5698	1.9685	39.89	1591.36
25.8341	.4627	1.9685	59.66	3558.77
26.2044	.9842	1.9685	4115.75	16.9 x 10 <sup>6</sup>



Table VII			
Strain Energy Release Rates			
Squared Load $P^2$ (lb <sup>2</sup> )	Change in Compliance $\Delta c$ (in./lb.)	Crack Extension $\Delta a$ (in.)	Strain Energy Release Rate $\mathcal{J}$ $\left(\frac{\text{in.-lb.}}{\text{in.}}\right)$
1597696	$1.77 \times 10^{-8}$	$3.60 \times 10^{-2}$	.39
2310400	$4.87 \times 10^{-8}$	$6.64 \times 10^{-2}$	.85
3125824	$7.78 \times 10^{-8}$	$1.11 \times 10^{-1}$	1.09
4096576	$2.02 \times 10^{-7}$	$1.44 \times 10^{-1}$	2.89
4631104	$6.46 \times 10^{-7}$	$2.42 \times 10^{-1}$	6.18
4910656	$1.26 \times 10^{-6}$	$3.86 \times 10^{-1}$	8.05
5505354	$2.64 \times 10^{-6}$	$4.43 \times 10^{-1}$	15.04

relation between  $K_I^2$  and the subcrack lengths.

The values of  $K_I^2$  determined from the progressive failure analysis versus subcrack lengths are shown in Fig. 42. For the values of  $K_I^2$ , considering values of load from 14.7341 ksi to 23.593 ksi, the correlation appears to be linear. At the last load level where the damage zone extends to the edge of the plate, there is no correlation between  $K_I^2$  and the subcrack lengths.

The values of  $\mathcal{J}$  versus subcrack length are plotted in Fig. 43. As with the  $K_I^2$  versus subcrack length for the progressive failure case, the relation appears to be linear. The data point associated with the last load increment is not within the range of a linear relation since the equation used to approximate the derivative of structural compliance with respect to crack extension, equation (7), is not valid.

From the limited amount of experimental data, it is difficult to determine absolutely if a linear relation exists. For the data available though, values of  $K_I^2$  and  $\mathcal{J}$  are linearly related

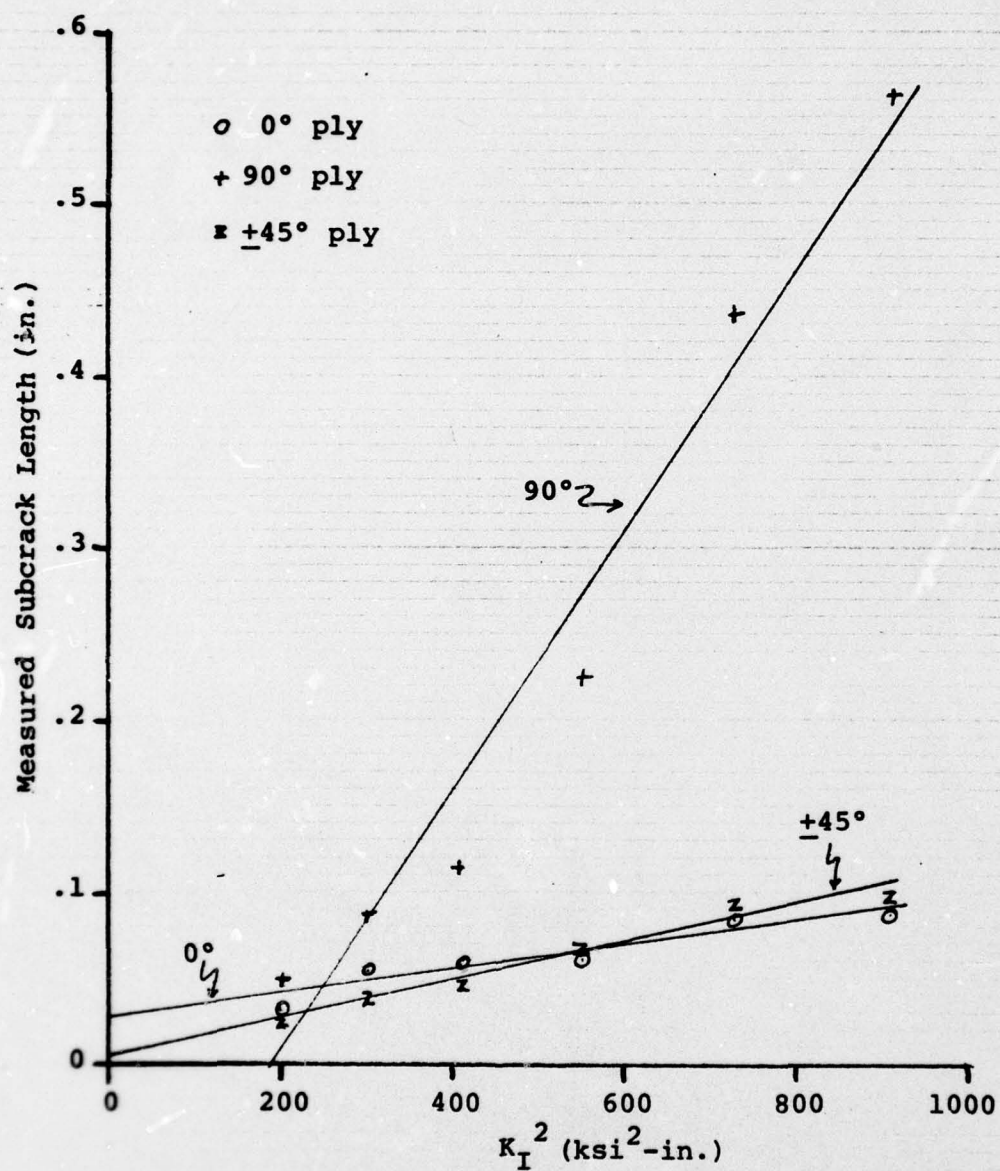


Figure 41.  $K_I^2$  Versus Subcrack Length for Elastic Model.



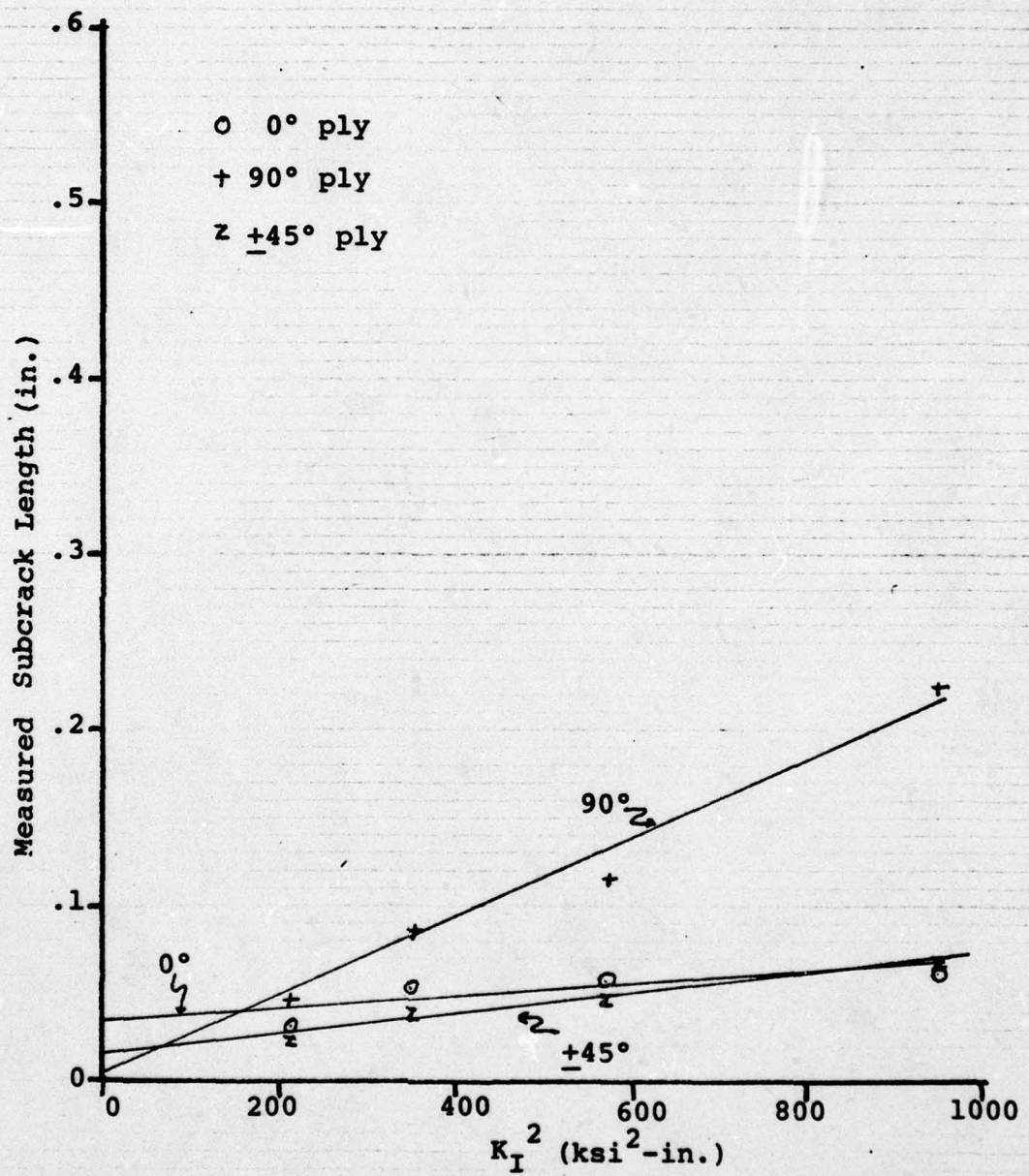


Figure 42.  $K_I^2$  Versus Subcrack Length for Progressive Failure Model.

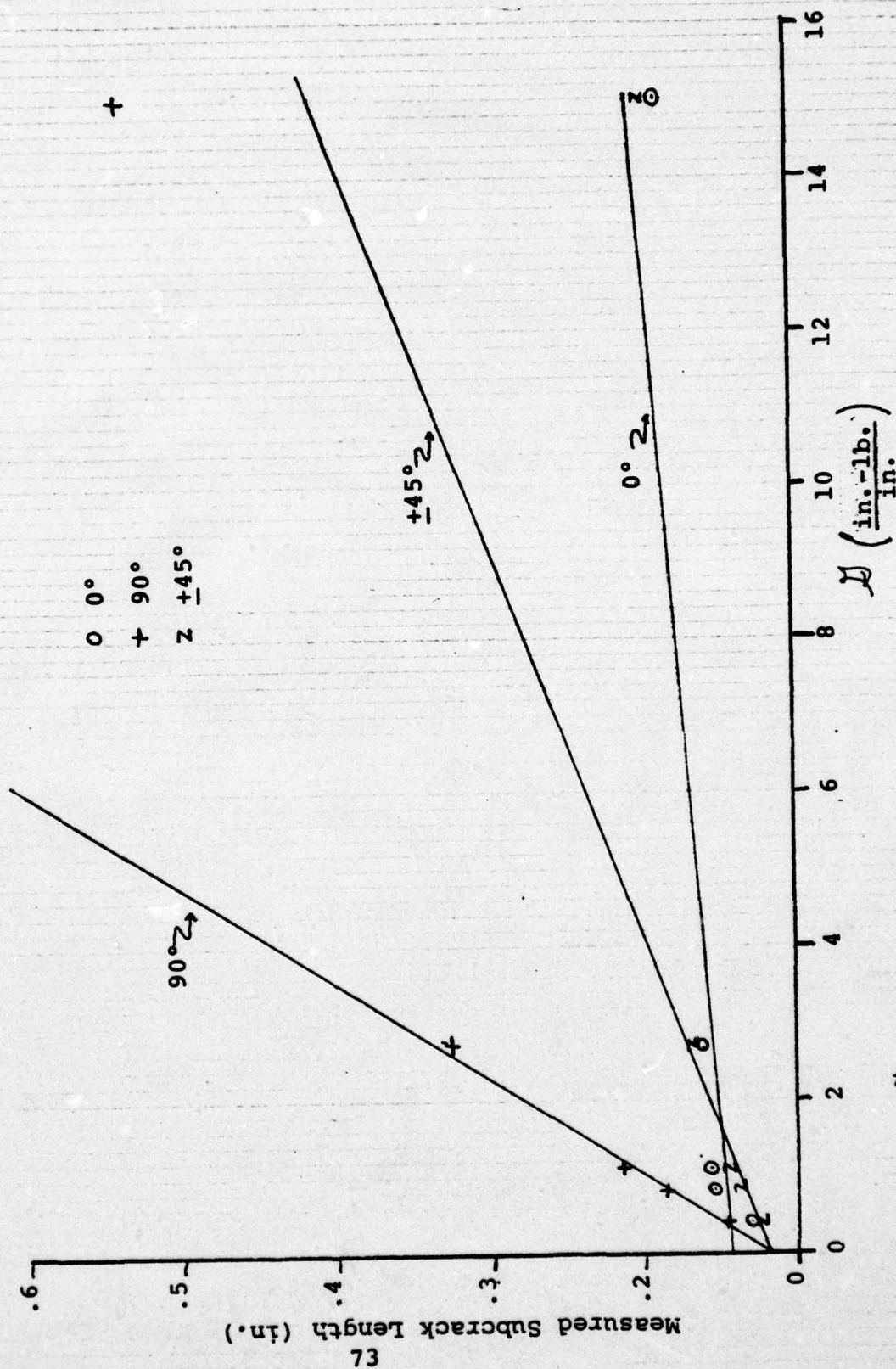


Figure 43.  $D$  Versus Subcrack Length for Progressive Failure Model.



to the ply subcrack lengths except when the load is at the point where the model exhibits large nonlinear behavior.

### Failure Prediction

As was stated in the theory chapter, calculated values of the opening mode stress intensity factor,  $K_I$ , can be used to predict failure. For this specimen the critical stress intensity factor is between 40.22 and 41.67 ksi-in.<sup>1/2</sup> Referring to Table V, it is seen that failure would occur at some value over 29.4683 ksi which is the experimental notched strength. If the value of  $K_I$  continued to increase in the same manner, the predicted fracture strength would be approximately 39 ksi or 32% over the experimental strength. Using the values of  $K_I$  in Table VI, the failure strength would be between 25.0853 and 25.8341 ksi. This is in error by 12-15%. As was expected the elastic analysis provides an upper bound on the fracture strength and the progressive failure analysis provides a lower bound.

The load-displacement diagram, Fig. 20, can be used to determine the fracture load from a stability standpoint. After the last iteration the slope changes from  $5.104 \times 10^3$  lb./in., for the load increment from 87.5% to 88.75% of the experimental fracture load, to  $2.99 \times 10^1$  lb./in. for the increment from 88.75% to 90%. Therefore, the failure strength becomes the stress at 88.75% or 26.204 ksi. This is below the actual fracture strength by 11%. For the instability analysis, there is not an upper bound since the elastic load displacement diagram

remains linear.

The last method that can be used to predict fracture strength is the applied load versus load bearing area diagram ( $P-A_{LB}$  diagram). The values of the applied load and the remaining load bearing area data are shown in Table VIII.

Table VIII		
Load and Load Bearing Area Data		
Load, P (lb.)	Elastic Remaining Load Bearing Area $A_{LB}$ (in. <sup>2</sup> )	Progressive Failure Remaining Load Bearing Area $A_{LB}$ (in. <sup>2</sup> )
256	$6.35 \times 10^{-2}$	$6.35 \times 10^{-2}$
504	$6.35 \times 10^{-2}$	$6.35 \times 10^{-2}$
760	$6.28 \times 10^{-2}$	$6.30 \times 10^{-2}$
1016	$6.24 \times 10^{-2}$	$6.22 \times 10^{-2}$
1264	$6.19 \times 10^{-2}$	$6.07 \times 10^{-2}$
1520	$6.12 \times 10^{-2}$	$5.78 \times 10^{-2}$
1768	$6.08 \times 10^{-2}$	$5.29 \times 10^{-2}$
2024	$6.03 \times 10^{-2}$	$4.67 \times 10^{-2}$
2152	*	$3.61 \times 10^{-2}$
2216	*	$1.93 \times 10^{-2}$
2248	*	0
2280	$5.93 \times 10^{-2}$	*
2528	$5.86 \times 10^{-2}$	*
* Analysis was not performed for these loads.		

The  $P$  versus  $A_{LB}$  diagram is shown in Fig. 44. The values along the horizontal axis correspond to values of  $A_{LB}$  which is the load bearing area of the plate between the notch and the edge of the plate. The load bearing area represents the portion of the plate in which all lamina have not failed. The vertical axis values are the applied loads,  $P$ . The straight line running in an oblique direction from the origin represents the boundary between loads and load bearing areas which do not



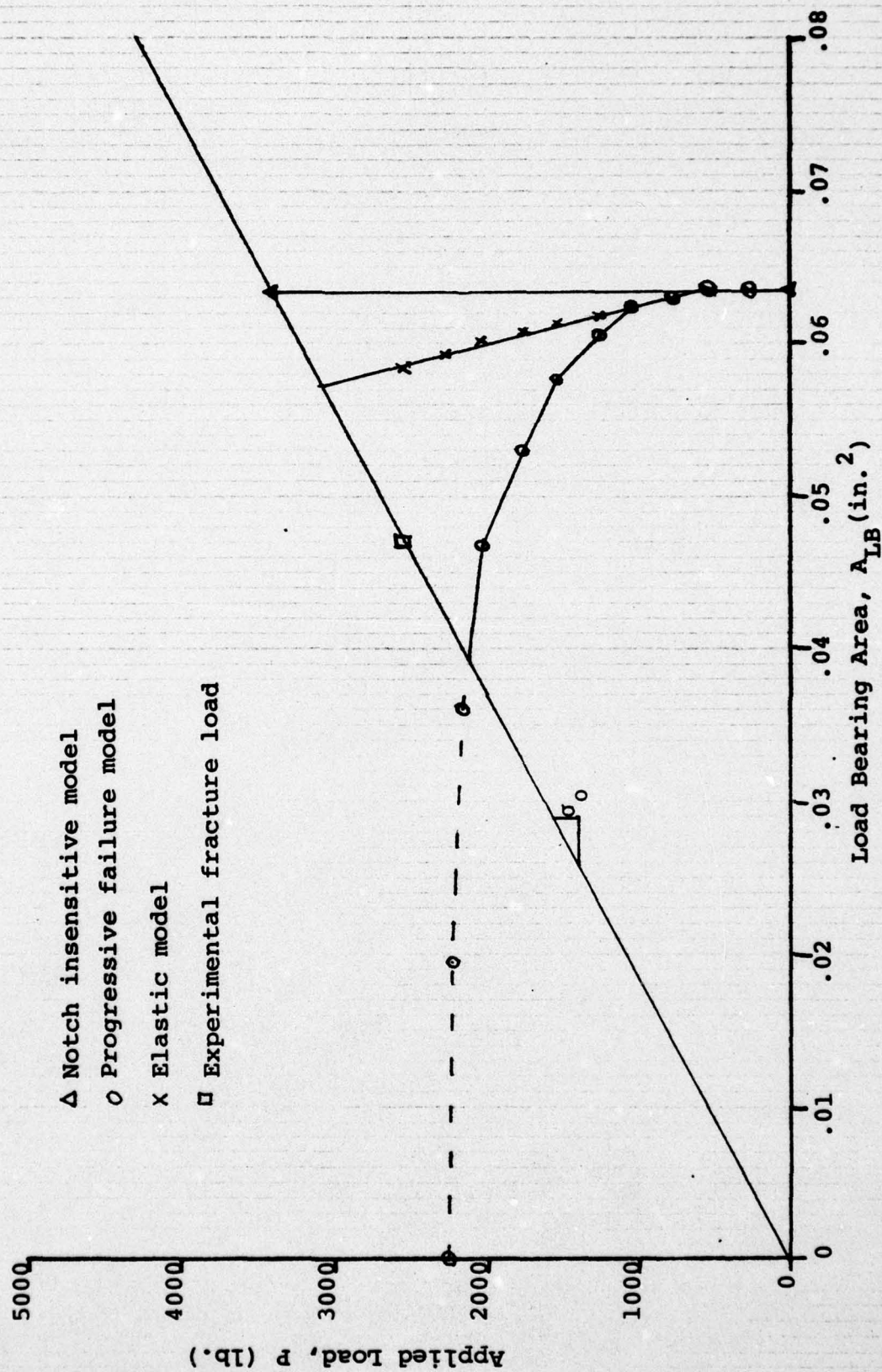


Figure 44. Analytical Load Versus Load Bearing Area Diagram for This Specimen.

result in failure and those combinations which cause failure. The slope of this line is equal to the unnotched failure stress of 54.4 ksi.

In order to explain the significance of the points on this diagram, the effect of notch sensitivity is examined. If the plate is not notch sensitive, the plate would fail when the load per area exceeded the notched tensile stress. The failure line would extend parallel to the load axis and the failure load would be 3400 lb. Since the plate is notch sensitive, the failure load is less, 2530 lb. This is a 34% error.

The growth of a damage zone at the crack tip accounts for the notch sensitivity. The elastic analysis can be used to model damage zone growth as shown in the diagram. Using only the elastic analysis, the predicted fracture load is 3100 lb. This is a 23% error. As expected, the elastic analysis provides a prediction which is above the actual fracture load.

The progressive failure analysis can also be used to predict fracture strength. The failure curve using this analysis becomes nonlinear in the upper load levels as the damage zone growth accelerates. The predicted fracture load using the progressive failure analysis is 2110 lb. This prediction is 16% below the actual fracture strength. As predicted using only theoretical considerations, the progressive failure analysis provides a lower bound on the fracture strength.



## V. Conclusions

As can be seen from the damage zone diagrams, the amount of damage in each ply is vastly different. Since it is impossible to experimentally measure this damage zone, the use of a numerical model such as the one presented in this thesis is warranted. Of course this thesis only studied one laminate with one notch orientation, but the accuracy of the model would indicate that further study should be conducted.

Using numerical models, it was possible to correlate ply subcrack length and two fracture mechanics parameter. Although it was not shown that the subcrack length was related to ultimate failure, the linear relation between  $K_I^2$ ,  $\mathcal{Y}$ , and subcrack length does indicate that some principles of fracture mechanics do apply, at least in the immediate vicinity of the crack tip.

Through numerical modelling, it was also possible to bound the fracture strength using either  $K_I$  or one of the other models. Although the instability analysis provided the closest approximation of fracture strength, it did not provide an upper bound. The  $P-A_{LB}$  approach provided bounds which were as close to the actual strength as that calculated using  $K_I$  values. Since the  $P-A_{LB}$  approach could be applied to all types of laminates and structures, it is considered better.

The numerical model presented in this paper is crude and could obviously be improved upon. The most important area

requiring improvement is that of the strength criterion. A better criterion could possibly give better estimates of which element plies have failed. The next area requiring improvement is in the treatment of element stiffness after failure. After exceeding the failure criterion, the element probably retains some load carrying capability. Since this analysis completely discounted all stiffness after element ply failure, it should provide estimates which are conservative. Yet the method always provides a lower bound solution which is important when considering problems in which experimental data is nonexistent or the experiment is in the planning stage. Improving stiffness characteristics may not provide a closer, conservative result. The last procedure which requires improvement is in the method of loading. Through the use of more sophisticated incremental loading and convergence methods, associated with nonlinear analysis, the predictions could be improved.

The applicability of the finite element method in analyzing composite fracture has been shown for this special case. Since finite element models can be applied to complicated structures, and are not as costly as experimentation, further study into the application of finite elements to this type of problem is necessary and should prove profitable.



### Bibliography

1. Steiner, J. E. "The Timing of Technology for Commercial Transport Aircraft." Astronautics and Aeronautics, 15: 42-55 (October 1977).
2. Coffin, M. D. and C.F. Tiffany. "New Air Force Requirements for Structural Safety, Durability, and Life Management." AIAA Paper 75-781, 1975.
3. Gallagher, J. P. "What the Designer Should Know About Fracture Mechanics Fundamentals." Society of Automotive Engineers Paper No. 710151, 1971.
4. Mandell, J. F., S.S. Wang, and F. J. McGarry. Fracture of Graphite Fiber Reinforced Composites. Technical Report AFML-TR-73-142. Wright-Patterson AFB, Ohio: Air Force Materials Laboratory, July 1973.
5. Conrad, Nicholas. On Microcrack Growth and Arrest in Simulated Fibrous Composites. Technical Report MM-3168-76-10. College Station, Texas: Mechanics and Materials Research Center, Texas A & M University, December, 1976.
6. Tsai, S. W. and H. T. Hahn. "Recent Developments in Fracture of Filamentary Composites," Proceedings of an International Conference on Prospects of Fracture Mechanics, (New York: Woodhoff International Publishing, 1974), 493-501.
7. Cotterell, B. and J. K. Reddel. "The Essential Work of Plane Stress Ductile Fracture." International Journal of Fracture, 13: 267-278 (June 1977).
8. Tetelman, A. S. and A. J. McEvily, Jr. Fracture of Structural Materials. New York: John Wiley and Sons, Inc., 1967.
9. Jones, R. M. Mechanics of Composite Materials. Washington, D. C.: Scripto Book, Co., 1975.
10. Morris, D.H. and H. T. Hahn. "Mixed Mode Fracture of Graphite/Epoxy Composites: Fracture Strength." Journal of Composite Materials, 11: 129-138 (April 1977).
11. Papirino, R. "Fatigue Fracture Initiation in Notched Graphite-Epoxy Specimens." Journal of Composite Materials, 11: 41-50 (January 1977).

12. Rockwell International Corporation. Advanced Composites Design Guide, Volume IV: Materials (Third Edition). Wright-Patterson Air Force Base, Ohio: Air Force Materials Laboratory, January 1973.
13. Hahn, H. T. "Fracture Behavior of Composite Laminates." Unpublished paper prepared at the Nonmetallic Materials Division, Air Force Materials Laboratory, Wright-Patterson Air Force Base, Ohio, December 1976.
14. Morris, D. H. and H. T. Hahn. "Fracture Resistance Characterization of Graphite/Epoxy Composites." ASTM STP 617, presented at the ASTM 4th National Conference on Composite Materials: Testing and Design, Valley Forge, Pennsylvania, May 1976.
15. Hahn, H. T. and J. Y. Kim. "Fatigue Behavior of Composite Laminates." Journal of Composite Materials, 10: 156-180 (April 1976).
16. Wu, E. M. and R. C. Reuter, Jr. "Crack Extension in Fiberglass Reinforced Plastics." T & AM Report No. 725. Urbana, Illinois, February, 1965.
17. Wu, E. M. "Fracture Mechanics of Anisotropic Plates." Composite Materials Workshop, edited by S. W. Tsai, J. C. Halpin, and N.J. Pagano. Stamford, Connecticut: Technomic Publishing Co., Inc., 1968.
18. Chang, F. H., D. E. Gordon, B. T. Rodini, and R. H. McDaniel. "Real Time Characterization of Damage Growth in Graphite/Epoxy Laminates." Journal of Composite Materials, 10: 182-192 (July 1976).
19. Whitey, J. M. and R. Y. Kim. "Effect of Stacking Sequence on the Notched Strength of Laminated Composites." Presented at the ASTM 4th National Conference on Composite Materials: Testing and Design, Valley Forge, Pennsylvania, May 1976.
20. Hill, R. The Mathematical Theory of Plasticity. London: Oxford University Press, 1950.
21. Mendelson, A. Plasticity: Theory and Application. New York: The MacMillan Company, 1968.
22. Tsai, S. W. Strength Characteristics of Composite Materials. NASA Contractor Report CR-224. Washington, D.C.: National Aeronautics and Space Administration, April, 1965.
23. Rockwell International Corporation. Advanced Composite Design Guide, Volume II: Analysis (Third Edition). Wright-Patterson Air Force Base, Ohio: Air Force Materials Laboratory, January 1973.



24. Nuismer, R. J. and G. E. Brown. "Progressive Failure of Notched Composite Laminates Using Finite Elements." UTEC ME 76-194, presented at the 13th Annual Meeting of the Society of Engineering Science, Inc., Hampton, Virginia, November, 1976.
25. Rockwell International Corporation. Advanced Composite Design Guide, Volume I: Design (Third Edition). Wright-Patterson Air Force Base, Ohio: Air Force Materials Laboratory, January 1973.
26. Liebowitz, H. Fracture: An Advanced Treatise. Volume I: Microscopic and Macroscopic Fundamentals. New York: Academic Press, Inc., 1968.
27. Phillips, D. C. "The Fracture Mechanics of Carbon Fibre Laminates." Journal of Composite Materials, 8: 130-141 (April, 1974).
28. Damage Tolerance Design Guidelines. (Draft). Prepared by Battelle Columbus Laboratories under Air Force Flight Dynamics Laboratory Contract F33 615-75-C-3101, January, 1976.
29. Nuismer, R. J. and J. M. Whitey. "Uniaxial Failure of Composite Laminates Containing Stress Concentrations." Fracture Mechanics of Composites. American Society for Testing and Materials Special Technical Publication 593 (1975).
30. Chan, S. K., J. S. Tuba, and W. K. Witson. "On the Finite Element Method in Linear Fracture Mechanics." Engineering Fracture Mechanics, 2: 1-7 (January 1970).
31. Venkayya, V. B. Finite element program OPTSTATCOMP written by Dr. Venkayya at the Air Force Flight Dynamics Laboratory, Wright-Patterson Air Force Base, Ohio.
32. The NASTRAN Theoretical Manual. NASA SP-221. Washington, D.C.: National Aeronautical and Space Administration, September 1970.

### Vita

William Paxton Witt, III, was born 29 June, 1948 in Carrollton, Illinois. He graduated from East Peoria High School in East Peoria, Illinois, in 1966. After receiving a Bachelor of Science in Engineering Sciences from the United States Air Force Academy in 1970, he served as aircraft maintenance officer at various Air Force bases. In June, 1976, he entered the Air Force Institute of Technology in the Graduate Astronautical Engineering program.

Permenent Address: 1225 Westheimer, #45  
Austin, Texas 78752



REPORT DOCUMENTATION PAGE		READ INSTRUCTIONS BEFORE COMPLETING FORM
1. REPORT NUMBER AFIT/GA/AA/77D-9	2. GOVT ACCESSION NO.	3. RECIPIENT'S CATALOG NUMBER
4. TITLE (and Subtitle) A Numerical Analysis of Fracture in a Laminated Fibrous Composite Plate		5. TYPE OF REPORT & PERIOD COVERED MS Thesis Jun 76 - Dec 77
7. AUTHOR(s) William P. Witt, III Captain USAF		8. CONTRACT OR GRANT NUMBER(s)
9. PERFORMING ORGANIZATION NAME AND ADDRESS Air Force Institute of Technology AFIT/EN Wright-Patterson AFB, Ohio 45433		10. PROGRAM ELEMENT, PROJECT, TASK AREA & WORK UNIT NUMBERS
11. CONTROLLING OFFICE NAME AND ADDRESS		12. REPORT DATE 9 December 77
		13. NUMBER OF PAGES 91
14. MONITORING AGENCY NAME & ADDRESS (if different from Controlling Office)		15. SECURITY CLASS. (of this report) Unclassified
		15a. DECLASSIFICATION/DOWNGRADING SCHEDULE
16. DISTRIBUTION STATEMENT (of this Report) Approved for public release, distribution unlimited		
17. DISTRIBUTION STATEMENT (of the abstract entered in Block 20, if different from Report)		
18. SUPPLEMENTARY NOTES Approved for public release; IAW AFR 190-17 Jerral F. Guess, Captain, USAF Director of Information		
19. KEY WORDS (Continue on reverse side if necessary and identify by block number) Composites Finite Elements Fracture Mechanics + or - sub 5		
20. ABSTRACT (Continue on reverse side if necessary and identify by block number) A crack in a laminated, composite plate was modelled using numerical methods. The experimental results used to validate this analysis were for a (0, +45, 90) graphite/epoxy plate with a center notch oriented normal to the loading direction. Two, Two-dimensional finite element models were used to determine the size of the crack tip damage zones. One involved a purely elastic analysis, and in the other, the element ply stiffness was completely discounted if the stresses exceeded the Tsai-Hill failure criterion. Damage		

AD-A048 907

AIR FORCE INST OF TECH WRIGHT-PATTERSON AFB OHIO SCH--ETC F/G 11/4  
A NUMERICAL ANALYSIS OF FRACTURE IN A LAMINATED FIBROUS COMPOSI--ETC(U)  
DEC 77 W P WITT  
AFIT/GA/AA/77D-9

UNCLASSIFIED

NL

2 OF 2  
AD  
A048 907



END  
DATE  
FILMED

2-78  
DDC



G

K sub I

zone diagrams showing the growth and shape of the ply damage zones at increasing load levels were developed for both models. The size of the subcracks in each ply were linearly related to the opening mode stress intensity factor,  $K_I$ , and to the strain energy release rate,  $G$ . A critical stress intensity factor approach, an instability approach, and a new fracture load prediction method based on load versus load bearing area diagrams were used to predict the fracture load. Since this new method provided close upper and lower bounds on the fracture load and is applicable to complicated structures, it was considered the best of the three methods.

UNCLASSIFIED